UNIVERSITY OF CALIFORNIA
SANTA CRUZ

Chromosome Dynamics in Meiosis and Mitosis

A dissertation submitted in partial satisfaction
of the requirements for the degree of

DOCTOR OF PHILOSOPHY

in

MOLECULAR, CELL, AND DEVELOPMENTAL BIOLOGY

by

Christian Nelson

June 2016

The Dissertation of Christian Nelson

Is approved:

_____
Professor Needhi Bhalla, Chair

_____
Professor Susan Strome

_____
Professor Seth Rubin

_____
Professor Doug Kellogg

_____
Tyrus Miller
Vice Provost and Dean of Graduate Studies

Table of Contents

List of Tables & Figures

Abstract

Chromosome Dynamics in Meiosis and Mitosis

Christian Nelson

Accurate chromosome segregation in meiosis and mitosis is essential for avoiding aneuploidy, a hallmark of cancer cells. In meiosis, proper chromosome segregation relies upon the events of meiotic prophase: pairing, synapsis, and recombination between homologous chromosomes. After meiotic recombination, chromosome architecture must be remodeled to form bivalents, the structures that promote proper homolog portioning at meiosis I. How recombination is coupled to chromosome remodeling remains unclear. Here, we show that the conserved ZHP-3 protein, required for crossover formation, has ubiquitin ligase activity *in vitro*, indicating it may serve to coordinate meiotic recombination with changes in chromosome architecture. Furthermore, we identify ZHP-3 as a substrate of both the MPK-1 (MAP) and CHK-1 kinases *in vitro*. MAP kinase integrates developmental processes with meiotic chromosome dynamics—it may phosphorylate ZHP-3 to coordinate and regulate these events. Finally, in mitosis, the spindle checkpoint regulates the fidelity of mitotic segregation by delaying the onset of anaphase until all chromosomes are properly attached to the mitotic spindle. Here, we identify PCH-2^{Trip13} as a novel component of the spindle checkpoint in *C. elegans*. We show that through the CMT-1^{p31comet} protein, PCH-2^{Trip13} regulates the amount of Mad2 that localizes to mitotic chromosomes, suggesting that PCH-2^{Trip13} may regulate the strength or robustness of the spindle checkpoint response. Furthermore, we show that the requirement for PCH-2^{Trip13} in MAD-2 recruitment to kinetochores is conserved in human epithelial RPE1 cells. Together, these data help to elucidate the mechanisms by which multiple cell types ensure proper chromosome segregation in both meiosis and mitosis, helping to preventing aneuploidy and, thus, human disease.

Acknowledgements

First, I would like to thank Dr. Needhi Bhalla for being an incredibly thoughtful, engaged, and supportive advisor. I'm grateful that she was so open to exploring new research avenues in the lab, allowing me to pursue projects outside of the lab's normal expertise. Needhi is incredibly passionate about basic research—I hope to take some of that passion with me in my next scientific endeavor.

I'd like to thank all of the members, past and present, of the Bhalla lab who have made the lab a great place to work and provided helpful insights into my research. I'd like to thank Tom Hwang and Pin-Hsi Chen who made some of the *C. elegans* strains and performed the yeast-two hybrid assays for Chapter 3. Finally, I'd like to thank my thesis committee members: Susan Strome, Seth Rubin, and Doug Kellogg, for their time and valuable feedback on my research. I'm grateful to both the NIH and QB3 for providing me funding for the first 3 years of my graduate work.

Last, but not least, I'm appreciative of my wife, Ally, for being so incredibly supportive during my time at UC Santa Cruz. Graduate school is much easier when you have someone to escape the lab with and explore.

Chapter 1: Introduction

Regulation of Meiotic Chromosome Structure

Meiosis is a specialized form of cell division required by sexually reproducing organisms. The process underlies adaptation, generating novel allele combinations, thereby contributing to diversification of the genome. The process involves a single round of replication followed by two successive rounds of chromosome segregation (Figure 1-1). In meiosis I, homologous chromosomes are segregated, while in meiosis II, sister chromatids are partitioned. Meiosis ends with production of haploid gametes, such as sperm, eggs, and pollen—thus, allowing for the restoration of diploidy upon fertilization. Defects at any stage of meiosis can lead to the production of aneuploidy gametes, causing zygotic inviability (miscarriage) or developmental disorders like Down syndrome and Kleinfelter's syndrome (HASSOLD AND HUNT 2001).

The events of meiotic prophase are critical for ensuring proper meiotic chromosome segregation (BHALLA AND DERNBURG 2008). The germline of the nematode C. *elegans* provides an excellent platform for studying these highly conserved events as they are segregated spatially within the gonad (Figure 1-2). Meiotic prophase begins with a homology search, where homologous chromosomes must find and pair with their unique partner. In *C. elegans,* this occurs in the transition zone (TZ; Figure 1-2), and is mediated by chromosome movements via attachments to cytoplasmic microtubules through conserved SUN/KASH domain proteins which span the nuclear envelope (PENKNER *et al.* 2007). Stable pairing between homologs is thought to initiate synapsis, the loading of the proteinaceous structure termed the synaptonemal complex (SC) between homologs (SATO *et al.* 2009). The SC then facilitates recombination between homologous chromosomes, resulting in the formation of chiasmata (PAGE AND HAWLEY 2003).

The SC assembles in a multi-step process: first, axial elements (e.g. HTP-1) are loaded onto sister chromatids, organizing chromatin into loops attached at their base

(KLECKNER 2006). Synapsis is completed through the loading of central region components (e.g. SYP-1) between homologous chromosomes, forming a zipper like structure (Figure 1-3). Crossover recombination then occurs within the context of the SC. Meiotic recombination is initiated through the introduction of programmed double-strand breaks throughout the genome via the conserved Spo11 enzyme (NEALE AND KEENEY 2006). Strand invasion and exchange are mediated by Dmc1/Rad51 (SHERIDAN *et al.* 2008) and the homolog, instead of the sister chromatid, is the preferred repair template in meiosis (SYMINGTON AND GAUTIER 2011), promoting the crossover outcome. In *C. elegans*, synaptonemal complex assembly is required for meiotic recombination (MACQUEEN *et al.* 2002).

Once recombination is completed and a crossover is formed, the synaptonemal complex must be disassembled and chromosomes must be restructured in order to promote the attachment of homologs to opposite spindle poles (NABESHIMA *et al.* 2005). This process, termed desynapsis, is directed by the sites of recombination, as SC disassembly occurs stochastically and aberrantly in the absence of crossovers (NABESHIMA *et al.* 2005). Furthermore, desynapsis is highly regulated and occurs asymmetrically: central element components like SYP-1 are first lost along the long arms of the bivalent, whereas some axial components, like HTP-1, are removed first from the short arms of the bivalent and retained on the long arms of the bivalent (Figure 1-3) (MARTINEZ-PEREZ *et al.* 2008). Thus, coordinating crossover formation with these highly regulated changes in chromosome structure is critical for ensuring the fidelity of meiotic chromosome segregation. In Chapter 2, I analyze how changes in chromosome structure are regulated and coordinated with the formation of crossovers during meiosis.

Coordinating Meiotic Prophase Events with Germline Development

The events of meiotic prophase must be highly coordinated to ensure the production of functional gametes (BHALLA AND DERNBURG 2008) . Furthermore, chromosome dynamics within individual nuclei must be coordinated with development of the germline so that events

like cellularization only occur in meiocytes that have completed specific meioitic events. This coordination almost certainly involves multiple signaling cascades and likely requires the transduction of extracellular cues to signals within individual meiocytes.

MAP kinases, highly conserved serine/threonine kinases, are responsible for controlling many complex events in *C. elegans* biology including, but not limited to: embryogenesis, oocyte growth, germ cell apoptosis, germ cell organization, and germ cell progression through meiosis (CHEN *et al.* 2001). *C. elegans* contains two MAP kinases, MPK-1 and MPK-2, regulated by the conserved extracellular RAS pathway, allowing extracellular signals to control intracellular events (MOGHAL AND STERNBERG 2003). MAP kinase (MAPK) is the most downstream kinase in the pathway and is activated through its phosphorylation. Activated MAPK then controls diverse cellular events through phosphorylation of its own unique set of substrates. MAPK is activated multiple times during meiotic prophase in *C. elegans*: in mid-pachytene, when crossover formation is completed and desynapsis occurs, and, again, in diakinesis (ARUR *et al.* 2009).

CHK-1, another highly conserved serine/threonine kinase, is involved in coordinating the DNA damage response with cell cycle arrest (SANCHEZ *et al.* 1997). It is activated via the ATM kinase in the presence of double-strand breaks (FLAGGS *et al.* 1997), which are programmed and plentiful in meiotic prophase. CHK-1 localizes to meiotic chromosomes and, like MAPK, is activated through phosphorylation. CHK-1 is required for meiotic progression in mice (WANG *et al.* 2014a). Chapter 3 explores the roles of both the MAP and CHK-1 kinases in the progression and coordination of meiotic events in *C. elegans*.

Regulation of Spindle Checkpoint Robustness in Mitosis

Cell division in eukaryotes requires mitosis, the cellular process that generates genetically identical daughter cells through chromosome partitioning. It is a single stage of the cell cycle (M phase), preceded by chromosome replication (S phase), and followed by cytokinesis, or division of the cytoplasm. Replicated chromosomes, called sister chromatids, are segregated into daughter cells during mitosis through their attachment to the mitotic

spindle. Defects in mitotic chromosome segregation can lead to the production of cells with an incorrect number of chromosomes, termed aneuploidy, which is a hallmark of cancer cells (HOLLAND AND CLEVELAND 2009).

The mitotic spindle is a bi-polar structure composed primarily of microtubules, whose dynamic instability is harnessed to transport chromosomes (KIRSCHNER AND MITCHISON 1986). Sister chromatids attach to the mitotic spindle through macromolecular protein structures called kinetochores (CHEESEMAN AND DESAI 2008a). Kinetochores assemble at centromeres, epigenetically defined regions of chromatin, specified by a unique histone variant, called CENP-A (CLEVELAND *et al.* 2003). Kinetochores not only connect mitotic chromatin with the spindle, but serve as molecular machines that drive chromosome segregation. In *C. elegans*, chromosomes are holocentric, meaning that kinetochores assemble along their entire lengths (DERNBURG 2001).

To ensure the fidelity of chromosome segregation in mitosis, the cell utilizes a molecular safety device, called the spindle checkpoint. The spindle checkpoint monitors chromosome attachment to the mitotic spindle and delays the onset of anaphase onset until all chromosomes are properly attached to the spindle, allowing time for error correction (LONDON AND BIGGINS 2014). Sister chromatids must bi-orient, or attach to microtubules emanating from opposite spindles, such that daughter cells receive equivalent sets of chromosomes. Kinetochores, the macromolecular protein complexes that direct chromosome segregation, also serve as the regulatory platforms for the spindle checkpoint (FOLEY AND KAPOOR 2013a).

Recently, it has become clear that the spindle checkpoint response, or the extent to which the molecular device delays anaphase, can vary in strength depending on the extent of attachment errors (COLLIN *et al.* 2013). Additionally, during *C. elegans* embryogenesis, the strength of the checkpoint response is dependent upon cell size (GALLI AND MORGAN 2016). In Chapters 4 and 5, the molecular signals underlying variations in checkpoint strength are explored in both *C. elegans* and cultured mammalian cells.

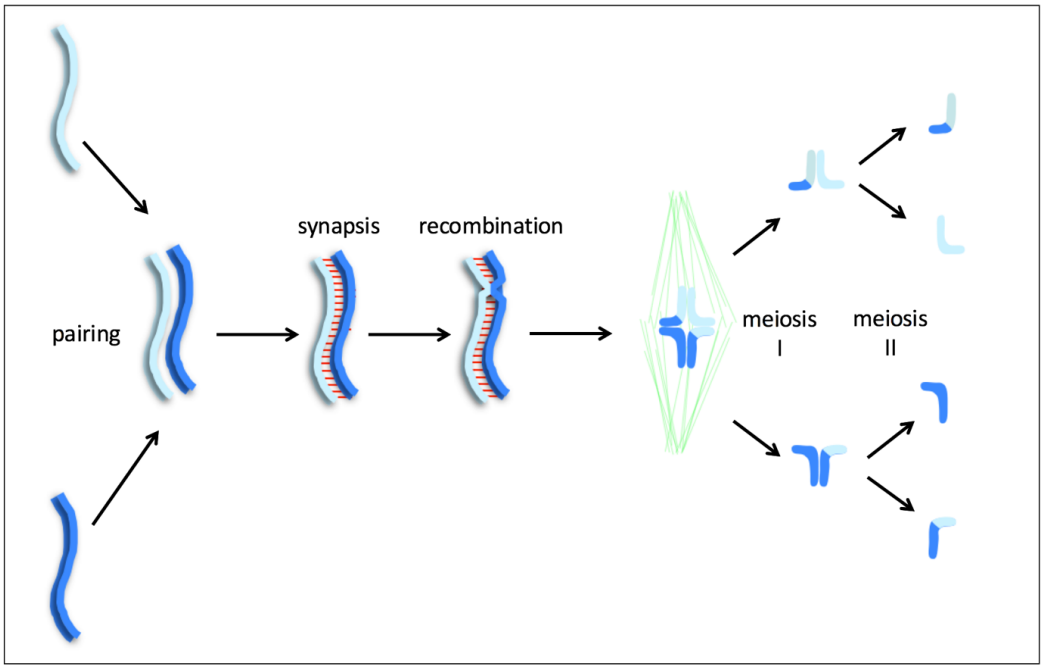

Figure 1- 1: The Events of Meiosis in *C. elegans.*

Meiosis involves one round of chromosome replication followed by two successive rounds of chromosome segregation: meiosis I, where homologs segregate, and meiosis II, where sister chromatids are partitioned. Proper homolog segregation at meiosis I requires a physical linkage between homologous chromosomes, called a chiasma. The formation of chiasmata depends on the events of meiotic prophase: pairing, synapsis, and crossover recombination. These processes are mediated by the synaptonemal complex, a proteinaceous structure that assembles between homologous chromosomes (shown in red).

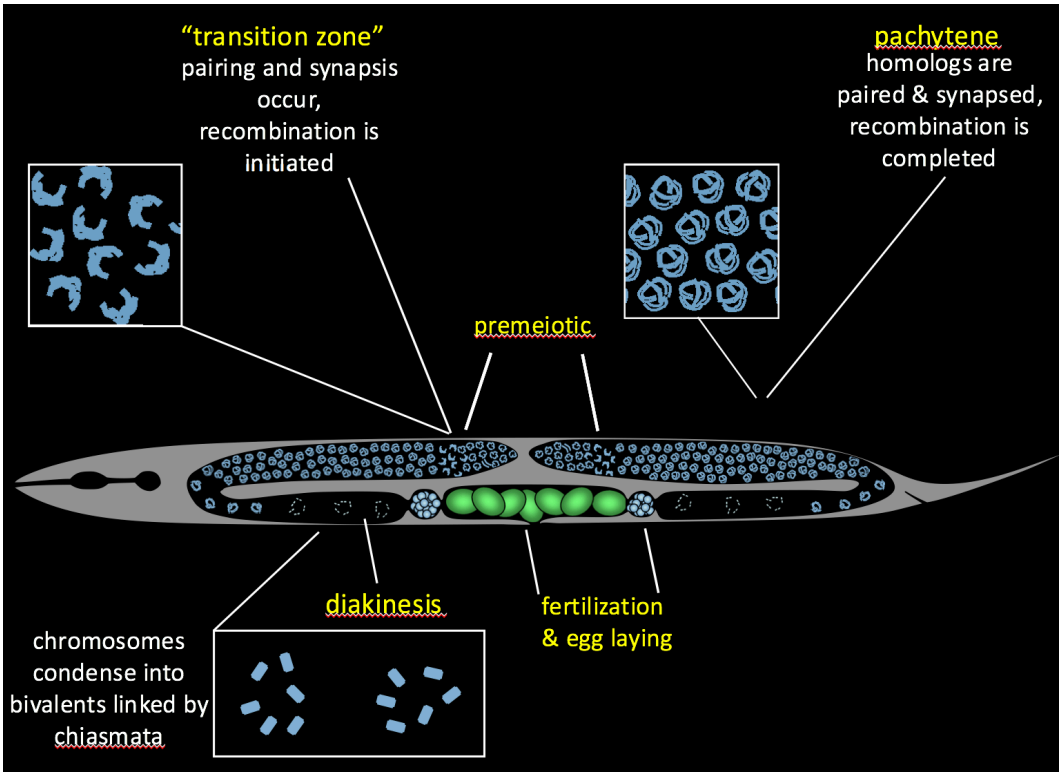

Figure 1- 2: The *C. elegans* germline and the events of meiotic prophase.

The spatial and temporal organization of meiotic nuclei in the *C. elegans* germline allows us to visualize these events of meiotic prophase cytologically as well as perturb them genetically. In the distal tip of the germline, nuclei divide mitotically. Nuclei then enter meiosis at the transition zone, characterized by polarized nuclear morphology. Meiocytes then enter pachytene, where pairing, synapsis, and recombination are completed. Finally, in diakinesis, chromosomes condense into bivalents: 6 bivalents are present representing the 6 homolog pairs. Oocytes then travel through the spermatheca to get fertilized, producing embryos that are laid through the vulva.

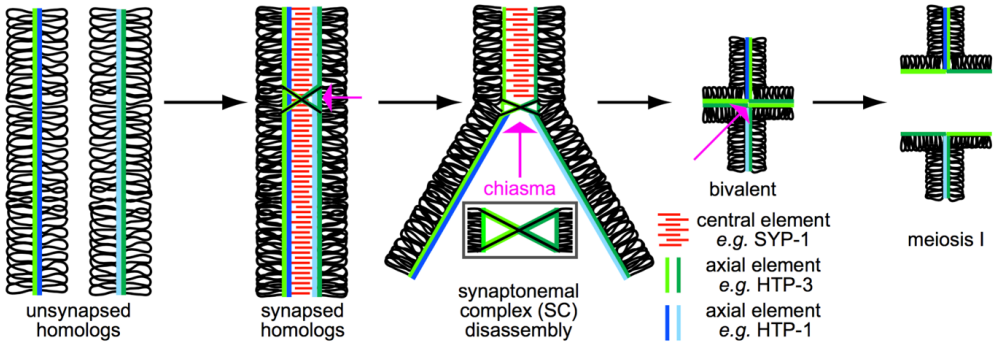

Figure 1- 3 : Synaptonemal complex assembly and disassembly.

During syanptonemal complex (SC) assembly, axial elements first load (HTP-3/HTP-1, green and blue) between sister chromatids, organizing chromatin into loops (unsynapsed homologs). Central elements (SYP-1, red) then “zip” together homologs (synapsed homologs). Within the context of the SC, meiotic recombination occurs, forming chiasmata. The long and short arms of the bivalent are defined by the location of the crossover: the shorter arm (top) has a crossover closer to the telomere. After crossover formation, the SC disassembles asymmetrically, with the central element SYP-1 first being removed from the long arm of the bivalent, then the short. In contrast, HTP-1 is retained on the long arm of the bivalent, and lost from the short arm, denoting the location where chromosomes will separate at meiosis I. Note the changes in chromosome architecture required to form the cruciform bivalent structure.

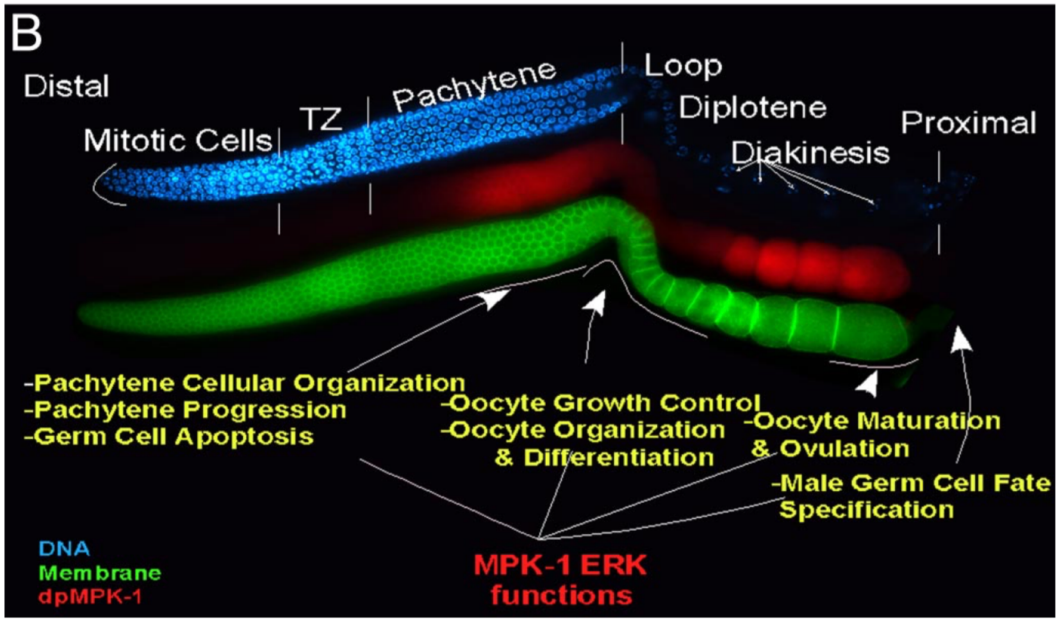

Figure 1- 4: MAP kinase is active in late pachytene and diakinesis*.

*This figure is taken from: Arur, S. *et al.* Multiple ERK substrates execute single biological processes in Caenorhabditis elegans germ-line development. *Proceedings of the National Academy of Sciences* **106,** 4776–4781 (2009). Activated MAP kinase, dpMPK-1, is present in multiple regions of the *C. elegans* germline. MPK-1 is required for the completion of numerous events within the germline.

Chapter 2: Regulation of Meiotic Chromosome Structure by the RING domain protein ZHP-3

Introduction

Meiotic chromosome segregation relies upon crossover recombination between homologous chromosomes, which generates the physical linkages, called chiasmata, that facilitate homolog segregation. Meiotic recombination is coupled to large-scale changes in chromosome structure in order to construct bivalents, which help direct chromosome segregation at meiosis I (Figure 1-3) (ZICKLER AND KLECKNER 1999). The *C. elegans* ZHP-3 protein provides a unique opportunity to study how the formation of meiotic crossovers is coordinated with changes in chromosome architecture. Originally identified as Zip3 in budding yeast, the protein provided one of the first links between the synaptonemal complex (SC) and meiotic recombination (AGARWAL AND ROEDER 2000). The *C. elegans* ortholog, ZHP-3, identified in 2004, also localizes to the SC and is required for meiotic recombination in nematodes (JANTSCH *et al.* 2004) More recently, it was demonstrated that RNF212, the murine ortholog, is required for meiotic crossover formation as well (REYNOLDS *et al.* 2013). Furthermore, sequence variations in the human orthologs of ZHP-3, RNF212a and RNF212b, were shown to be associated with genome-wide changes in recombination rates (KONG *et al.* 2008), suggesting functional conservation in humans. Thus, elucidating ZHP-3 function should provide a conserved mechanism for regulation of both crossover formation and chromosome architecture in meiotic prophase.

In addition to its requirement for meiotic crossovers, *C. elegans* ZHP-3 is involved in SC morphogenesis. A separation of function allele, *zhp-3::GFP*, promotes nearly wildtype levels of recombination, yet aneuploidy amongst its progeny remains high (BHALLA *et al.* 2008). This indicates additional roles for ZHP-3 after meiotic recombination. Analysis of chiasmata in *zhp-3::GFP* germlines indicates improper SC disassembly in this mutant, with the axis component HTP-1 retained on the short axes of the bivalent, where it would normally be removed (Figure 2-1). Together, these data indicate that ZHP-3 coordinates the formation of meiotic crossovers with disassembly of the SC in order to facilitate changes in chromosome structure associated with bivalent formation.

Finally, ZHP-3 and its orthologs contain RING domains (PERRY *et al.* 2005), indicating that they may function in ubiquitin or SUMO (small ubiquitin-related modifier) signaling as E3 ligases. Ubiquitin and SUMO are post-translational modifications that serve to regulate a protein's stability, function, and/or localization (GILL 2004). E3 ligases function in concert with E1 activating enzymes and E2 conjugating enzymes to attach these small polypeptides (DESHAIES AND JOAZEIRO 2009). Poly-ubiquitination is generally associated with targeting of a specific protein for degradation via the proteasome. Thus, elucidating ZHP-3 ligase function and identifying relevant meiotic substrates will help to uncover how meiotic crossover formation is coordinated with changes in chromosome structure.

Results

Immunoprecipitated mCherry::ZHP-3 forms ubiquitin conjugates *in vitro*

ZHP-3 contains a RING domain, indicating it may have ubiquitin or SUMO ligase activity (Figure 2-2). SUMO is critical for SC formation in budding yeast (VOELKEL-MEIMAN *et al.* 2013) and it has previously been argued that Zip3, the budding yeast ZHP-3 ortholog, is Zip3 is a SUMO ligase (CHENG *et al.* 2006). However, in *C. elegans*, deletion of the SUMO protein causes only minor meiotic defects and crossover formation remains unimpeded (BHALLA *et al.* 2008) . Finally, ZHP-3 shows a genetic interaction with mutations in *ubc-2*, an E2 ubiquitin conjugating enzyme, but not with mutations in *ubc-9*, the E2 SUMO conjugating enzyme (data not shown). Together, these data argue that ZHP-3 is more likely to function in the ubiquitin pathway. Therefore, we explored the possibility that ZHP-3 functions as a ubiquitin ligase.

To test this possibility, we first generated an n-terminally mCherry tagged ZHP-3 for immunoprecipitation (IP) in *C. elegans* using microparticle bombardment (PRAITIS *et al.* 2001). This construct rescues the *zhp-3* null allele, *jf61*, and localizes properly to the synaptonemal complex (data not shown), indicating it is functional. Immunoprecipitation of mCherry-ZHP-3 with an RFP antibody pulled down the full length fusion protein (Figure 2-

3A). Next, we tested whether ZHP-3 could assemble poly-ubiquitin conjugates *in vitro*. mCherry-ZHP-3 formed the characteristic "smear" of ubiquitin and poly-ubiquitin species in the presence of E2 conjugating enzyme (human Ubch5c), E1 activating enzyme (human Ube1), ATP, and ubiquitin (HA-ubiquitin) (Figure 2-3B). We chose Ubch5c as our E2 enzyme for *in vitro* assays as it has been shown to provide robust ubiquitylation activity with a number of E3 ligases. The ubiquitylation activity we observed also required mCherry::ZHP-3, as no activity was observed in a control reaction where an anti-RFP IP was performed in the absence of tagged protein (Figure 2-3B). Together, these data indicate that mCherry::ZHP-3 can function as an E3 ubiquitin ligase *in vitro*.

To establish a ubiquitylation assay for the identification of ZHP-3 substrates, we required a modified form of ZHP-3 lacking E3 ligase activity to serve as a negative control. To this end, we made two point mutations in the RING domain (C39A/C42A) which we refer to as RFM (RING finger mutant) and inserted *mCherry::zhp-3-rfm* into the *C. elegans* genome (Figure 2-2). Unfortunately, mCherry::ZHP-3-RFM failled to localize to the SC and didn't rescue the *zhp-3* null allele, *jf61* (data not shown). Furthermore, IP of even *wildtype C. elegans ZHP-3* isolated only very small amounts of purified protein. Therefore, we decided to express ZHP-3 recombinantly to increase protein yield and allow for quick mutagenesis.

Recombinant 3XFLAG::ZHP-3 ubiquitin ligase activity depends on its n-terminus

Previous analysis in the lab found full-length ZHP-3 to express poorly and remain insoluble in *E. coli*. Therefore, I turned to *S. cerevisae* for recombinant expression. N-terminally 3XFLAG tagged ZHP-3 under GAL promoter control expressed well in budding yeast (3 hour galactose induction) and was readily immunoprecipitated using a FLAG antibody (Figure 2-4A). As a control for ubiquitylation assays, a deletion of the entire ZHP-3 N-terminus, which contains the RING domain (Figure 2-2), was also purified (Figure 2-4A). 3XFLAG-ZHP-3 and 3XFLAG-ZHP-3-ΔN were then assayed for auto-ubiquitylation utilizing *in vitro* assays. Again, full length ZHP-3 exhibited robust ubiquitylation activity in the presence of HA-ubiquitin, ATP, and E1 and E2 enzymes (Figure 2-4B). Importantly, this activity was

lost in assays containing 3XFLAG-ZHP-3-ΔN, indicating the N-terminus of ZHP-3, which contains the RING domain, is necessary for ubiquitylation *in vitro* (Figure 2-4B). Furthermore, in this assay, the beads bound to ZHP-3 were washed in high salt (0.5M KCl) prior to elution and western blot analysis. This indicates that the poly-ubiquitin complexes seen here (Figure 2-4B) are likely auto-ubiquitylation or ubiquitylaton of a very tightly bound interacting protein. Ubiquitylated E1 and E2 enzymes are no longer visible (Figure 2-4B) compared to previous assays (Figure 2-3B) as they were washed away from beads prior to analysis.

Next, we we curious if the RING domain is required for ZHP-3's *in vitro* ubiquitylation activity, as is the case for most E3 ligases (DESHAIES AND JOAZEIRO 2009). To answer this question, we made point mutations in two highly conserved cysteine residues (Figure 2-2), C39 and C42, which should abolish RING domain function, a domain that generally mediates E2 enzyme binding (DESHAIES AND JOAZEIRO 2009). Again, this mutant, ZHP-3-C39A-C42A (ZHP-3-RFM) was expressed in budding yeast and purified using an n-terminal 3XFLAG tag (Figure 2-4C). *In vitro* ubiquitylation assays, however, showed that this mutant still retained ubiquitin ligase activity (Figure 2-4D). Together, these data show that ZHP-3 can auto-ubiquitylate *in vitro*, strongly arguing that ZHP-3 functions as an E3 ubiquitin ligase *in vivo.* Furthermore, ZHP-3 ubiquitin ligase activity depends on its n-terminus, but not a fully functional RING domain in its n-terminus.

A candidate approach to identify meiotic substrates of ZHP-3 ubiquitin ligase activity

To identify meiotic substrates of ZHP-3 ubiquitin ligase activity, a candidate approach was taken. Figure 2-5A shows meiotic substrates that were cloned for analysis of ZHP-3 ubiquitylation. We focused on meiotic proteins that are degraded or whose localization changed throughout meiotic prophase, especially in response to crossover formation. The most obvious candidate is HTP-1, an axial element of the SC, which is normally disassembled or degraded from chromosomes in late meiotic prophase, but fails to do so in a hypomorphic *zhp-3* mutant (Figure 2-1). Other components of the SC, including HTP-1-HTP-3, SYP-1-SYP-4, HIM-3, and LAB-1, many of which change their localization in response to

crossovers, also make excellent candidates. Proteins involves in the late stages of recombination, such as MSH-4, MSH-5, and COSA-1, need to be targeted to crossover sites that are marked by ZHP-3 (BHALLA *et al.* 2008), a process that could involve ubiquitin signaling. Finally, many cohesin complex components are involved in SC assembly and must be removed or remodeled prior to meiotic chromosome segregation. These proteins, such as REC-8, SMC-1, SMC-3, COH-1-COH-4, WAPL-1, and PDS-5, also represent putative candidates for ZHP-3 ubiquitylation.

To assay candidates for ZHP-3 ubiquitylation, substrate cDNAs were cloned, utilizing ORFeome DNA (LAMESCH *et al.* 2004) or PCR amplified *C. elegans* cDNA, into vectors for *in vitro* transcription/translation (IVT/T). We utilized a rabbit reticulocyte system for expression (Promega) in the presence of radiolabeled [35S]-methionine. Expression candidate substrates was verified by radiography (a portion are shown in Figure 2-5B) prior to use in ubiquitylation assays. Note that the majority of candidates produce a single, intense band at the proper molecular weight (Wormbase). Some candidates (e.g. SYP-4), produce multiple bands, likely indicative of some degradation. However, expression of the majority of clones was adequate for our assay.

Next, we incubated each IVT/T candidate substrates with either full length yeast-purified 3XFLAG-ZHP-3 (lane 3), 3XFLAG-ZHP-3-ΔN (lane 2), or no E3 ligase (lane 1) (Figure 2-5C). All reactions included E1 enzyme, E2 enzyme, ATP, and ubiquitin. Figure 2-5C shows an example experiment from candidate substrate ubiquitylation analysis. MSH-5 and HTP-1 are the most promising candidates for ZHP-3 ubiquitylation (Figure 2-5C). They show upper forms (indicating polyubiquitylation) in the presence of full length ZHP-3 and all necessary ubiquitin reagents. Putative substrates, such as these, will need further *in vitro* and *in vivo* verification before they can be classified as *bona fide* ZHP-3 substrates.

Discussion

Here, we have definitively shown that ZHP-3 possesses auto-ubiiquitylation activity *in vitro,* indicating that the *C. elegans* gene is likely an E3 ubiquitin ligase. Previous

bioinformatic anlaysis of Zip3 and its orthologs indicated that their RING domains were more likely to function in the ubiquitin pathway rather than the SUMO (PERRY *et al.* 2005). However, budding yeast Zip3 was shown to have sumoylation activity (CHENG *et al.* 2006) and more recent analysis of human RNF212 suggested that it, too, is a SUMO ligase (QIAO *et al.* 2014). Still, the elucidation of true ZHP-3/Zip3/RNF212 function remains elusive as no *bona fide in vivo* substrates have been identified for the ligase in any organism.

One possibility is that *C. elegans* ZHP-3 has maintained or evolved a unique function in nematodees. *C. elegans* has holocentric chromosomes, posing unique challenges during meiotic chromosome segregation. ZHP-3 may have evolved ubiquitin ligase function to deal with nematode specific changes in meiotic chromosome structure. Another meiotic E3 ubiquitin ligase, called Hei10, is present in the *Arabidposis* as well as human genomes, where it functions in meiotic crossover formation (QIAO *et al.* 2014) (CHELYSHEVA *et al.* 2012). *C. elegans* is thought to lack Hei10, but ZHP-3 may be a Hei10 ortholog rather than a Zip3 ortholog. Given the role of Hei10 in CO formation and the presence of a RING domain functioning in ubiquitin ligation, it would be easy to argue that ZHP-3 is functionally conserved from Hei10. Finally, it remains formally possible that ZHP-3 is, indeed, a SUMO ligase. The experiments presented here were performed *in vitro* and under promiscuous conditions, in the presence of a non-native E2 ligase. Many future experiments are needed to establish the molecular functions of ZHP-3 and its orthologs *in vivo.*

To clarify ZHP-3 ligase function in *C. elegans*, we performed a large scale IP of GFP-3XFLAG::ZHP-3 followed by mass spectrometry to identify interacting proteins (data not shown). Identification of the native E2 conjugating enzyme, which should interact with ZHP-3, would provide great insight into ZHP-3 function. This E2 conjugating enzyme could then be utilized in *in vitro* assays to facilitate ZHP-3 substrate identification. It may be that ZHP-3 necessitates a specific E2 for ubiquitin conjugation to substrates. Furthermore, this analysis may identify post-translational modifications (i.e. ubiquitylation) as well as possible ZHP-3 substrates. Unfortunately, while the IP worked, I was unable to elute sufficient GFP-

3XFLAG::ZHP-3 for suitable mass spec coverage on ZHP-3 or any interacting proteins. Continuation of this experiment in the future will greatly facilitate our understanding of ZHP-3 function.

Finally, a quirk of ZHP-3 is the lack of a requirement for its RING domain in auto-ubiquitylation (Figure 2-4D). While RING domains are generally required for the E2-3 interaction, examples in the literature indicate that other sequences can mediate this interaction, including U-BOX domains and CUE domains (XIE AND VARSHAVSKY 1999) (CHEN *et al.* 2006) . Analysis of ZHP-3 and its orthologs shows that more conserved sequence is present in the N-terminus just c-termminal to the RING domain (data not shown). I previously attempted to make deletions spanning portions of this region to determine if they would abrogate *in vitro* ubiquitylation activity, but I was unsuccessful. Future experiments will need to identify the E2 interacting domain or motifs within the ZHP-3 n-terminus.

As for identification of ZHP-3 substrates, both MSH-5 and HTP-1 remain the most promising. HTP-1 is removed asymmetrically from bivalents prior to meiosis I. Hypomorphs of *zhp-3* fail in this asymmetric disassembly, providing *in vivo* evidence that ZHP-3 may mediate this process (Figure 2-2). MSH-5 likely functions to facilitate the stability of double holliday junctions, promoting interhomolog crossovers. Intriguingly, it forms many foci at DSB sites throughout the genome, but then becomes restricted to just 6 foci which form interhomolog crossovers—indicating ubiquitylation could regulate the removal of non-CO MSH-5 foci or could designate specific MSH-5 foci at future CO sites. Both HTP-1 and MSH-5 show weak conjugate formation in the presence of full length ZHP-3 (Figure 2-5C). These experiments should be repeated with HA-ubiquitin to analyze whether or not these upper forms of HTP-1 and MSH-5 are, indeed, ubiquitin conjugates. IP of these proteins from nematodes may also identify ubiquitin conjugates, which should be lost in the asbsence of ZHP-3 or with a ZHP-3 mutant that fails to bind the E2 conjugating enzyme. Together, these experiments will establish HTP-1/MSH-5 as *bona fide* ZHP-3 substrates.

Materials & Methods

C. elegans Strains and Husbandry

The wildtype *C. elegans* strain background was Bristol N2 (BRENNER 1974) . All strains were maintained at 20°C. The mCherry:::ZHP-3 strain used for immunoprecipitation (Figure 2-3) was generated via microparticle bombardment (PRAITIS *et al.* 2001). After mCherry::ZHP-3 expression was verified by live microscopy, the strain was backcrossed 6X to N2 and then to the *zhp-3* null allele, *jf61*.

Immunofluorescence

All microscopy was performed on a DeltaVision Personal DV deconvolution microscope (Applied Precision) equipped with a 100X N.A. 1.40 oil-immersion objective (Olympus) coupled with a CoolSNAP charge-coupled camera (Roper Scientific). Immunofluorescence of gonads was performed as described previously (BHALLA AND DERNBURG 2005) .The following primary antibodies were used for *C. elegans* immunofluorescence (dilutions in parentheses): guinea pig anti-HTP-3 (1:500); rabbit anti-HTP-1/2 (1:200); rabbit anti-SYP-1 (1:500); and mouse anti-GFP (1:100). Secondary antibodies were Cy3/Cy5 anti-guinea pig and and anti rabbit (Jackson Immunochemicals) and Alexa-Fluor 488 anti-mouse (Invitrogen). Three-dimensional image stacks were collected at 0.2-μm Z-spacing and processed by constrained, iterative deconvolution. Image scaling and analysis were performed using functions in the softWoRx software package. Projections were calculated by a maximum intensity algorithm. Composite images were assembled and some false coloring was performed with Adobe Photoshop.

Immunoprecipitations & Western Blots

Immunoprecipitations in yeast were performed essentially as described as previously (AKIYOSHI *et al.* 2009b) using FLAG M2 antibody (Sigma) conjugated to Protein G Dynabeads (Invitrogen). Salt was increased to 0.5M KCl during IP and washes to eliminate any interacting proteins. 3XFLAG- tagged ZHP-3 proteins were then eluted from beads using

3XFLAG peptide (Sigma), quantified, and stored at -80C prior to use in ubiquitylation assays. Some ubiquitylation assays were performed with 3XFLAG-ZHP-3 still attached to beads.

Immunopreciptations in *C. elegans* were performed similarly, except that an anti-RFP antibody was used (a kind gift from A. Desai) bound to Protein a Dynabeads (Invitrogen). 150mM KCl was used for ZHP-3 IP. Furthermore, Roche Protease Inhibitor Tablets (EDTA-Free) were utilized in all buffers to avoid protein degradation from nematode gut proteases.

For western blots, samples were run on 12% SDS-PAGE gels, transferred to nitrocellulose using a Trans-Blot SD Semi-Dry system (Bio-Rad), blocked in a PBST + 5% (w/v) non-fat milk solution, and then probed with either mouse anti-HA 12CA5 (1:5000; Sigma) or mouse anti-FLAG M2 (1:2500; Sigma) overnight at 4°C. Blots were washed 3x for 10 minutes in PBST, probed for 1 hour using an HRP-conjugated secondary antibody (rabbit or mouse; GE Healthcare), washed 3x for 10 minutes in PBST, and then analyzed using a chemiluminescent substrate (Thermo Scientific).

***In vitro* Transcription/Translation & Ubiquitylation Assays**

In vitro transcription/translation of candidate ZHP-3 substrates was performed utilizing the TNT Quick Coupled rabbit reticulocyte system according to the manufacturer's instructions (Promega). Briefly, cDNAs were cloned into either pCP108 (no tag) or pCP109 (n-terminal 3XHA tag) using the Gateway Cloning System (Invitrogen). 25uL IVT/T reactions were assembled: 20uL Quick Master Mix, 1uL [^{35}S]-Methionine, 500ng plasmid DNA, nuclease free water to 25uL. Mixes were the incubated at 30C for 90 minutes. A portion of the protein was then either run out on a SDS-PAGE gel (5uL) and the remainder was utilized in ubiquitylation reactions.

Ubiqutiyation assays were essentially performed as described previously (RANJITKAR *et al.* 2010). Reactions were performed in 20uL volume: 400ng E1 activating enzyme (human E1); 400ng E2 conjugating enzyme (human UbcH5c), 2.5ug HA-ubiquitin (or untagged), 2mM Mg-ATP, 50mM Tris-Hcl pH=7.5, 2.5mM $MgCl_2$, and 0.5mM DTT. 50ng of 3XFLAG-ZHP-3 variants were used when protein was eluted from beads. To analyze auto-ubiquitination,

ZHP-3 was left attached to beads, which were washed 3X in 50mM Tris-Hcl pH=7.5, 0.5mM DTT, 2.5mM $MgCl_2$ and then then the beads were resuspended in the 20uL reaction volume. Reactions were run for 30 minutes at 30C. Reactions were quenched with 20uL 2X SB and boiling for 5 minutes. For reactions containing beads, the beads were separated (reaction was discarded, beads retained) and were washed 3X in immunoprecipitation buffer prior to elution by boiling in 20uL sample buffer. Samples were then analyzed via SDS-PAGE and either exposed to a phosphor screen (GE Health Sciences) for analysis of [^{35}S]-Methionine labeled substrates or an immunoblot was performed (HA-Ubiquitin). All ubiquitin reagents were purchased from Boston Biochemicals.

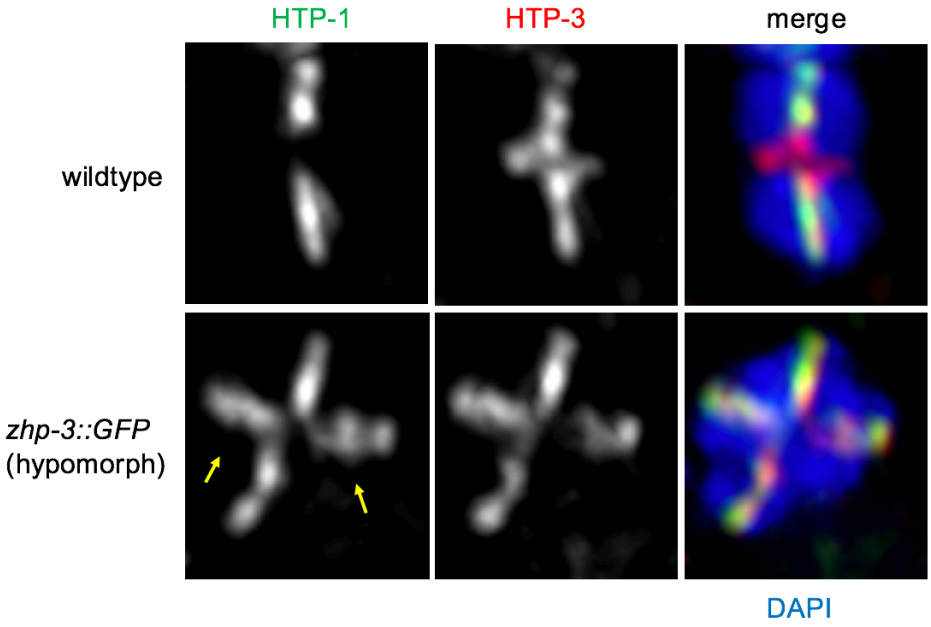

Figure 2- 1: HTP-1 disassembly is impaired in *zhp-3* mutants.

The axial element component, HTP-1, is normally lost from the short arm of bivalents and retained on the long arms or the bivalent prior to meiosis I. In the hypomorphic *zhp-3::GFP* mutant, HTP-1 is found along both arms of the bivalent (arrows denote retention of HTP-1 on short arms).

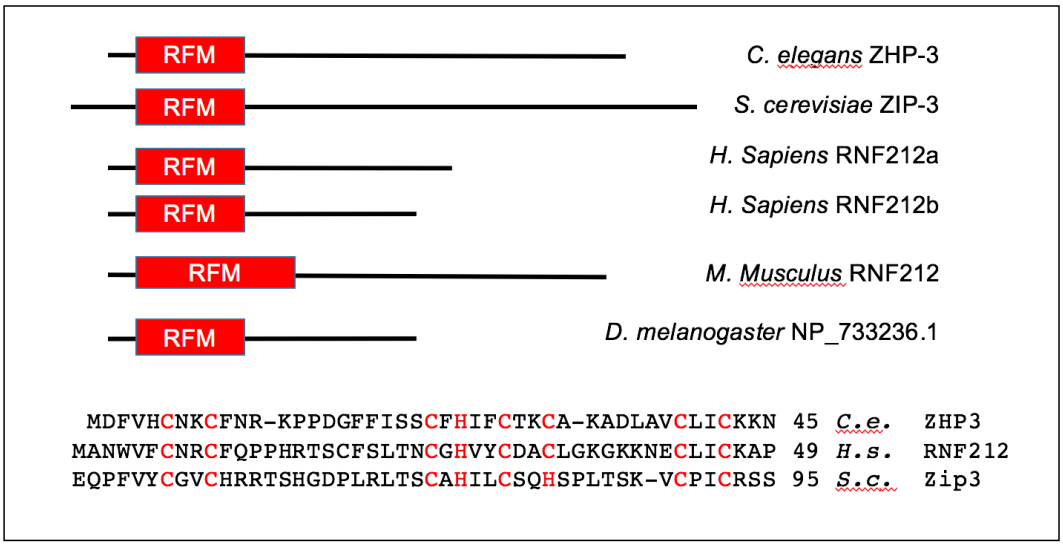

Figure 2- 2: ZHP-3 contains a RING finger motif.

ZHP-3 contains a RING domain, a hallmark of E3 ubiquitin and SUMO ligases. While ZHP-3 orthologs in other species contain considerable variability in their c-termini, the RING domain in the N-terminus remains highly conserved from budding yeast to humans. Below, the sequences of the RING domains in the worm, human, and budding yeast proteins are aligned for comparison.

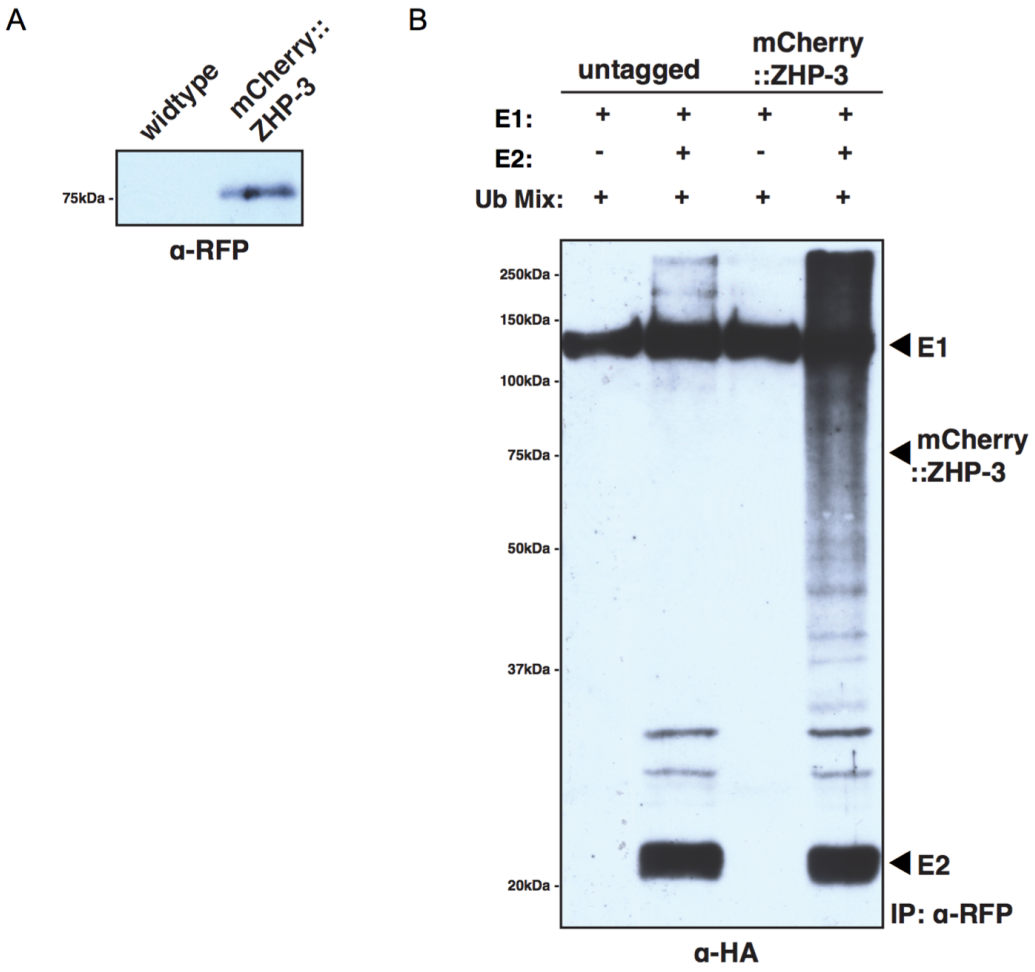

Figure 2- 3: Purified mCherry::ZHP-3 auto-ubiquiitylates *in vitro.*

(A) mCherry::ZHP-3 was immunoprecipitated from C. elegans lysates. The fusion protein, containing an n-terminal mCherry tag, runs at the predicted molecular weight of 75kDa. (B) mCherry::ZHP-3 auto-ubiquitylates *in vitro*. Immunprecipitation of mCherry::ZHP-3 or an untagged control strain were performed. IP'd protein was left on beads and utilized for *in vitro* ubiquitylation assays. Ubiquitin (HA-Ub) conjugates were seen only in the presence of mCherry-ZHP-3 and E2 conjugating enzyme. See Materials & Methods for experimental details.

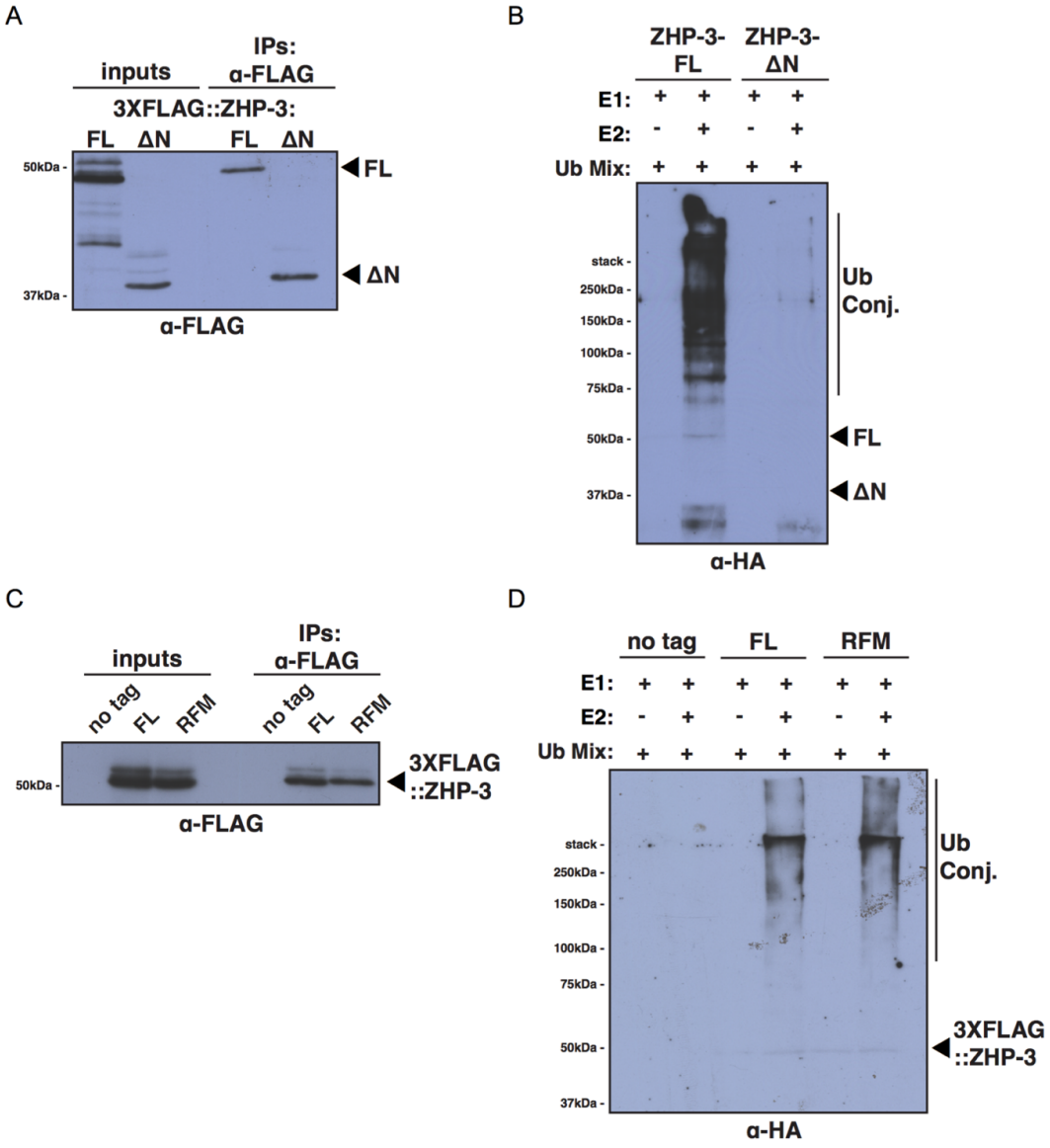

Figure 2- 4: ZHP-3 auto-ubiquitylation activity depends on the n-terminus, but not the RING domain.

(A) n-terminally 3XFLAG tagged full-length ZHP-3 or an n-terminal truncation (ΔN) were successfully expressed and immunprecipitated from budding yeast. (B) The n-terminus of ZHP-3, which contains the RING domain, is required for auto-ubiquitylation activity *in vitro.* See Materials & Methods for experimental details. (C) n-terminally 3XFLAG tagged full-length ZHP-3 and a RING finger domain mutant (RFM) were successfully expressed and immunprecipitated from budding yeast. An untagged strain was used as a control. (D) Both ZHP-3 and ZHP-3-RFM form ubiquitin conjugates in an *in vitro* reaction.

A

Role in Meiosis	Protein
Late stages of recombination	MSH-4, MSH-5, COSA-1
Component of SC that changes localization in response to crossovers	HTP-1, HTP-2, SYP-1, SYP-2, SYP-3, SYP-4, LAB-1
SC components	HIM-3, HTP-3
Cohesin complex components involved in SC formation	REC-8, SMC-1, SMC-3, COH-1, COH-2, COH-3, COH-4, WAPL-1, PDS-5

B

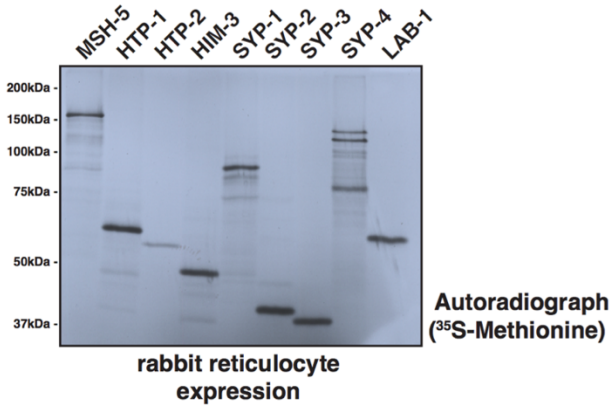

C

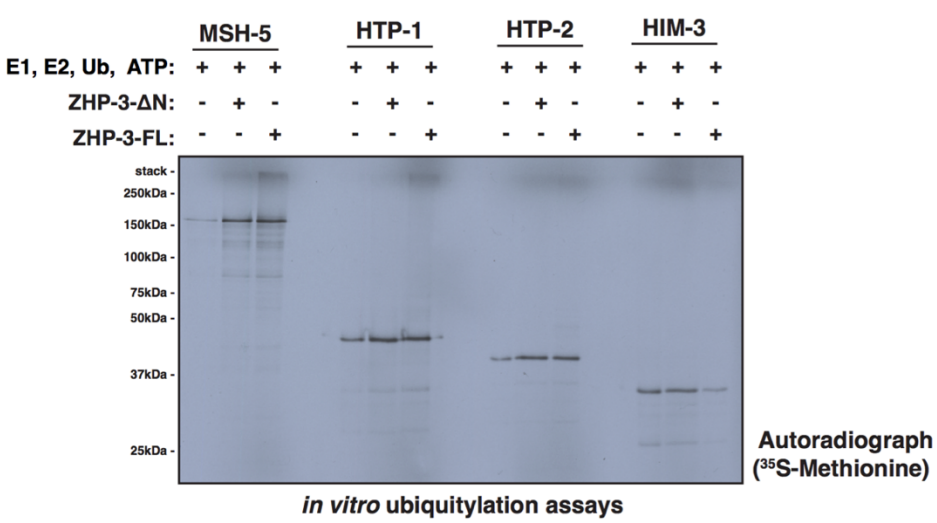

Figure 2- 5: Identification of ZHP-3 E3 ubiquitin ligase substrates *in vitro.*

(A) Candidate meiotic substrates to be tested for ZHP-3 ubiquitylation *in vitro.* (B) Expression of some candidates via rabbit reticulocyte IVT/T is verified via autoradiograph. (C) Candidates MSH-5, HTP-1, HTP-2, and HIM-3 are tested for ubiquitylation by ZHP-3. Note that for both MSH-5 and HTP-1, a "smear" of ubiquitin like conjugates appears in the 3rd lane, containing full length ZHP-3 and all necessary ubiquitin reagents, indicating they may be true ZHP-3 substrates.

Chapter 3: Coordinating Meiotic Chromosome Dynamics with Germline Development

Introduction

The MAP kinase (MAPK) signaling cascade links extracellular signals to intracellular events. *C. elegans* MAP kinase, MPK-1, is activated in late pachytene and is required for numerous events in the germline, including meiotic progression, germ cell apoptosis, oocyte growth and meiocyte cellularization (ARUR *et al.* 2009). Therefore, MAP kinase represents an ideal candidate for a master regulator that coordinates the development of the germline with the chromosomal events of meiotic prophase. Identification of meiotic substrates of MAP kinase in *C. elegans* will likely uncover how these processes are interconnected and coordinated.

ZHP-3 is required for meiotic crossover formation and the subsequent changes in chromosome structure (JANTSCH *et al.* 2004; BHALLA *et al.* 2008). ZHP-3 localizes to the SC dynamically: in early pachytene, it localizes along the length of the synaptonemal complex (SC), then is partially relocalized or removed in late pachytene, forming comet like structures, and finally becomes restricted to foci, 6 per nucleus, marking crossovers (Figure 3-1A) (BHALLA *et al.* 2008). Thus, understanding how ZHP-3 is regulated may help us to understand how meiotic events are coordinated and mechanistically linked to the germline developmental program.

CHK-1, another highly conserved serine/threonine kinase, that is activated via the ATM in the presence of double-strand breaks (DSBs) via ATM(FLAGGS *et al.* 1997), is involved in coordinating the DNA damage response with cell cycle arrest (SANCHEZ *et al.* 1997). CHK-1 is activated via phosphorylation and in *C. elegans* appears to be hyper-activated in mid-pachytene (WOGLAR *et al.* 2013b), when crossing over is nearing completion and ZHP-3 is re-localizing. ZHP-3 also contains two CHK-1 consensus motifs in its c-terminus and therefore may be regulated by CHK-1 directly (Figure 3-7A).

ZHP-3 fails to re-localize to the site of COs in *mpk-1* mutants (Figure 3-1B), indicating MAPK may regulate ZHP-3 localization and/or function. MAPK uses docking sites, or distinct

amino acid signatures, to help recognize substrates and enhance their phosphorylation (SHARROCKS *et al.* 2000). ZHP-3 contains a putative MAPK docking site as well as 5 MAPK consensus motifs for phosphorylation (Figure 3-2A). Thus, understanding how ZHP-3 is regulated by MAPK is critical for understanding how meiotic prophase events are coordinated with oocyte maturation

Results

ZHP-3 is phosphorylated by MAPK *in vitro*

MAPK is activated via phosphorylation by an upstream kinase. Di-phosphorylated MPK-1 is present in late pachytene and diakinesis (Figure 1-4), indicating that MPK-1 is active when ZHP-3 is re-localized to CO sites. Moreover, *mpk-1* mutants fail to re-localize ZHP-3 to CO sites in late pachytene (Figure 3-1B). Given this, it is possible that MAP kinase phosphorylates ZHP-3 directly to regulate its localization and/or function. We set out to test this hypothesis.

To this end, GST-ZHP-3 was expressed in *E. coli* and a purification was attempted. However, GST-ZHP-3 was insoluble (data not shown) and therefore purification was not attempted. Instead, the ZHP-3 coding sequence was split into two fragments: an n-terminal fragment containing the RING domain (Figure 3-2B) and a c-terminal fragment (Figure 3-2C). The c-terminal fragment contains the putative MAPK phosphorylation sites as well as the putative MAPK docking site (Figure 3-2C). These fragments were soluble and readily purified on a glutathione column via affinity chromatography (Figure 3-2D). To test whether ZHP-3 was a substrate for MAPK *in vitro*, recombinant murine p42 (ERK/MAPK) and *in vitro* kinase assay was performed using 1ug of either recombinant GST-ZHP-3 n-terminus or c-terminus as substrate in the presence of [γ-^{32}P]-ATP. Robust phosphorylation of the c-terminus containing the putative MAPK phosphorylation motifs, but not the n-terminus, was detected (Figure 3-2-D&E).

To test which of the consensus motifs in the c-terminus are required for ZHP-3 phosphorylation by MAPK, various combinations of serine/threonine to alanine mutants were constructed. The 3 serines in close proximity (starting with S205) seemed to be required for the majority of the phosphorylation, as mutation of all 3 simultaneously essentially eliminated phosphorylation (ZHP-3-3A; Figure 3-2D/E). Mutation of T341 and T269 had little effect on ZHP-3 phosphorylation, however, ZHP-3-5A, with all 5 sites mutated, showed less phosphorylation than ZHP-3-3A, indicating the kinase may phosphorylate them weakly (Figure 3-2D/E). Furthermore, we identified an additional putative MAPK site, S190. Given that mutation of the previous 5 sites completely ablates ZHP-3 phosphorylation, we did not analyze this mutant for phosphorylation *in vitro*. However, when analyzing ZHP-3 phospho-mutants *in vivo*, we mutated this site, creating the mutant referred to here as ZHP-3-6A.

Mutation of the ZHP-3 MAP kinase docking site in *C. elegans* reduces the fidelity of crossover formation and results in embryonic inviability

To analyze whether ZHP-3 phosphorylation by MAPK was required for ZHP-3 localization and/or function *in vivo*, we inserted *zhp-3-6A* mutant using MosSCI (FROKJAER-JENSEN *et al.* 2008). All transgenes were n-terminally tagged with a GFP-tag. Wildtype, 6A, and a MAPK docking site mutant (*zhp-3-dock)* were inserted on chromosome II and crossed to the *zhp-3* deletion, *jf61*, to test complementation. A viability assay was performed to assess embryonic lethality. Intriguingly, while the wildtype and 6A mutant completely rescued *jf61*, the docking mutant, *zhp-3-dock*, showed 80% embryonic lethality. To verify this result, we made a second insertion of *zhp-3-dock* which showed similar viability (data not shown). Notably, the mutations in ZHP-3-dock did not reduce phosphorylation by MAP kinase *in vitro*.

To better understand the viability defect found in *zhp-3-dock* mutants, we first assayed for meiotic COs. ZHP-3 forms 6 foci that mark CO sites in late pachytene. Intriguingly, while *zhp-3-dock* formed foci, there were almost always fewer than 6 foci (Figure 3-4A). Quantification indicated an average of 4 foci for both independent insertions of *zhp-3-dock*, indicating a defect in CO formation (Figure 3-4B).

To further assess the *zhp-3-dock* CO defect, we analyzed the formation of bivalents at diakinesis. In a wildtype *C. elegans* meiosis, 6 DAPI stained bodies are present at diakinesis that stain with a cruciform HTP-3 structure. Intriguingly, *zhp-3-dock* mutants showed abrogated HTP-3 staining at diakinesis (Figure 3-4C) and increased DAPI body count (Figure 3-4D). DAPI bodies were between 7 and 8 on average (Figure 3-4D). Thus, the embryonic inviability observed in *zhp-3-dock* mutants is likely due to a defect in CO formation (Figure 3-4B) that leads to the presence of univalents at diakinesis (Figure 3-4C). These univalents form aneuploid gametes that likely produce inviable progeny. Furthermore, GFP::ZHP-3-dock localizes properly to the SC in early pachytene (Figure 3-4E), indicating the protein's initial localization is unaffected and the meiotic defects in *zhp-3-dock* mutants don't appear to be due to gross protein misfolding or instability.

ZHP-3 mutants show no genetic interactions with *mpk-1(ga111)*

Given that the 6A mutant did not display embryonic lethality (Figure 3-3A), CO formation, or localization (data not shown), we worried that ZHP-3 may not be a *bona* fide in vivo target for ZHP-3. Given that ZHP-3-6A shows no defects in embryonic viability, localization, or CO formation, we wondered if the defects seen in *zhp-3-dock* were indeed due to altered MAPK regulation. To test this, we assayed for a genetic interaction between our 6A and dock alleles with a previously characterized temperature sensitive allele of MPK-1, *mpk-1(ga111)* (LACKNER AND KIM 1998).

At 22C, *mpk-1(ga111)* is largely viable (Figure 3-5). Unfortunately, *zhp-3-dock* and *zhp-3-6A* mutants showed no decrease in embryonic viability when combined with *mpk-1(ga111)* at 22C, a temperature at which MAPK function is reduced in this background. This indicates that the *zhp-3-dock* phenotype may not be due to reduced MAPK phosphorylation/function. In addition, we performed these experiments at 23C, but *mpk-1(ga111)* was almost completely inviable at this temperature (data not shown), eliminating the ability to perform this experiment.

Finally, we assayed for viability in the WT, 6A, and dock mutants at 25C. At 25C, meiosis begins to become negatively affected by temperature in *C. elegans*. Unfortunately, we saw reductions in embryonic viability with all three allleles (Figure 3-6), especially *zhp-3-dock*, which was almost completely inviable at 25C. No corresponding decrease in viability of wildtype worms was seen (Figure 3-6), indicating that the GFP-ZHP-3 transgene is likely affected at this temperature, reducing the fidelity of meiosis. Furthermore, immunoflourscence analysis of GFP-ZHP-3-6A and *zhp-3-dock* at 25C indicated reduced localization to the SC (data not shown), indicating these proteins may become less functional as temperature increases.

Taken together, these data argue that the defects in CO formation and embryonic viability in *zhp-3-dock* mutants may be merely due to reduced protein function due to mutagenic load or misfolding. Given that neither mutant showed a genetic interaction with *mpk-1(ga111)* and we couldn't detect a phenotype for the phosphomutant (6A) on its own, we cannot definitively state whether or not MPK-1 regulates ZHP-3 *in vivo*.

CHK-1 phosphorylates ZHP-3 *in vitro*

Given that MPK-1 may not regulate ZHP-3 *in vivo*, we tested whether another meiotic kinase, CHK-1, could phosphorylate ZHP-3. Again, we phosphorylated ZHP-3 *in vitro* using recombinant human CHK-1. We detected weak phosphorylation of the n-terminus and strong c-terminal phosphorylation of ZHP-3 (Figure 3-7B). To identify the sites phosphorylated by CHK-1 *in vitro*, we assayed the phosphorylated ZHP-3 via mass spectrometry (UC Berkeley). We detected phosphorylation at two CHK-1 consensus sites, S308 and S388 (Figure 3-7A).

To determine whether CHK-1 regulates ZHP-3 localization *in vivo*, we knocked down *chk-1* via RNA interference (RNAi) using the Ahringer library (KAMATH AND AHRINGER 2003) vector V13G06. RNAi of *chk-1* did not alter GFP::ZHP-3 localization, which still formed 6 foci per nucleus in late pachytene (Figure 3-7C). Furthermore, diakinesis bivalent structure, as assayed by cruciform HTP-3, was unaffected by *chk-1*^{RNAi} (Figure 3-7D). Six DAPI bodies

were also present in all *chk-1*^{RNAi} diakinesis nuclei analyzed (Figure 3-7D), indicating inter-homolog CO were properly formed on all 6 *C. elegans* chromosomes.

In mutants defective in meiotic recombination, like *spo-11* and *msh-5*, ZHP-3 fails to re-localize to CO sites in late pachytene due to a failure in crossing over (BHALLA *et al.* 2008). CHK-1 is active in mid-pachytene prior to re-localization of ZHP-3 at CO sites, but becomes inactive in late pachytene when ZHP-3 forms foci (WOGLAR *et al.* 2013b). Therefore, CHK-1 phosphorylation may inhibit ZHP-3 re-localization until COs are formed. This hypothesis predicts that in the absence of recombination (*msh-5* or *spo-11* mutants) and *chk-1*, ZHP-3 may re-localize aberrantly. However, analysis of *spo-11*;*chk-1*^{RNAi} and *msh-5*;*chk-1*^{RNAi} mutant germlines indicated that GFP::ZHP-3 remained co-localized with the SC, as is true in these mutants in the presence of *chk-1*. Thus, RNAi of *chk-1* does not alter ZHP-3 localization in the presence or absence of meiotic COs. Hence, while CHK-1 phosphorylates ZHP-3 *in vitro*, further experimentation is required to determine whether ZHP-3 is a *bona fide* CHK-1 substrate *in vivo*.

Discussion

Our results clearly indicate that MAPK phosphorylates the c-terminus of ZHP-3 *in vitro* and that this phosphorylation depends on the presence of predicted MAPK consensus sites. However, we were unable to discern a function for this phosphorylation *in vivo*, as mutation of all 6 phosphorylation sites did not reduce nematode viability, alter ZHP-3 localization, or affect meiotic CO formation. One possibility is that MAPK is a promiscuous kinase *in vitro* and that ZHP-3 is not a true substrate in nematodes. A second possibility is that MAP kinase phosphorylates multiple redundant substrates to help promote crossover completion and coordinate it with SC disassembly. For example, MSH-5, like ZHP-3, is required for CO formation, and has multiple MPK-1 consensus sites and is phosphorylated by MPK-1 *in vitro* (data not shown; personal communication with Swathi Arur). Mutation of phosphorylation sites in multiple CO-promoting proteins may be necessary to produce a

strong meiotic phenotype. Future analysis should combine GFP::ZHP-3-6A with additional *mpk-1* phoshpo-mutants.

A second possibility is that ZHP-3 merely functions as a docking partner for MPK-1 in the germline in order to help promote MPK-1 phosphorylation of other meiotic proteins. Mutation of the MPK-1 docking site in ZHP-3 resulted in embryonic inviability due to reduced meiotic crossover formation. Analysis of MPK-1 localization and/or activation in *zhp-3-dock* mutants should provide insight into whether meiotic function of MAP kinase is affected in this mutant background. Furthermore, identification of additional meiotic MAP kinase substrates will be necessary should this hypothesis prove to be correct. This hypothesis predicts that *zhp-3-dock* mutants may show reduced or abolished phosphorylation of these additional MAP kinase substrates.

Finally, our analysis identified ZHP-3 as an *in vitro* substrate of an additional meiotic kinase, CHK-1. However, RNAi of *chk-1* failed to produce any alterations in ZHP-3 localization or defects in crossover formation. However, given that *chk-1* is essential for embryonic viability in *C. elegans* (KALOGEROPOULOS *et al.* 2004), knockdown had to be performed beginning at the larval stage L1. Therefore, it remains unclear whether our knockdown of *chk-1* was complete. Further analysis should use a more potent RNAi vector, pDONRT7, containing terminators, or utilize the degron system for *chk-1* knockdown (ZHANG *et al.* 2015). Furthermore, analysis of a ZHP-3-S309/S366 phospho-mutant *in vivo* should provide evidence as to whether ZHP-3 is a true CHK-1 substrate and how CHK-1 phosphorylation regulates meiotic prophase.

Materials & Methods

***C. elegans* Strains and Husbandry**

The wildtype *C. elegans* strain background was Bristol N2 (BRENNER 1974) . All strains were maintained at 20°C, except for the temperature sensitive mpk-1(ga111) allele, which was maintained at 15°C. All GFP::ZHP-3 alleles were inserted using MosSCI single-copy insertion on the ChII site (ttTi5605) and their insertion was verified via PCR and live

microscopy. Each insertion was then backcrossed 6X to N2 and then to the *zhp-3* null allele, *jf61*, for analysis.

Immunofluorescence

All microscopy was performed on a DeltaVision Personal DV deconvolution microscope (Applied Precision) equipped with a 100X N.A. 1.40 oil-immersion objective (Olympus) coupled with a CoolSNAP charge-coupled camera (Roper Scientific). Immunofluorescence of gonads was performed as described previously (BHALLA AND DERNBURG 2005) .The following primary antibodies were used for *C. elegans* immunofluorescence (dilutions in parentheses): guinea pig anti-HTP-3 (1:500); guinea pig anti-ZHP-3 (1:250); rabbit anti-SYP-1 (1:500); and mouse anti-GFP (1:100). Secondary antibodies were Cy3/Cy5 anti-guinea pig and and anti-rabbit (Jackson Immunochemicals) and Alexa-Fluor 488 anti-mouse (Invitrogen). Three-dimensional image stacks were collected at 0.2-μm Z-spacing and processed by constrained, iterative deconvolution. Image scaling and analysis were performed using functions in the softWoRx software package. Projections were calculated by a maximum intensity algorithm. Composite images were assembled and some false coloring was performed with Adobe Photoshop.

***In vitro* kinase assays & Immunoblots**

Kinase assays were performed at 30°C in 10uL reactions with 1X kinase buffer (50mM Tris pH7.4, 1mM DTT, 25mM β-glycerophosphate, 5mM $MgCl_2$,10μM ATP) for 30 minutes. Reactions included 1μL ^{32}P- γ-ATP (Perkin Elmer), 10U of activated MAPK (NEB), and 50ng of substrate. Reactions were quenched by adding 10uL 2X sample buffer and boiling for 5 minutes. Reactions were run out in duplicate on two 12% SDS-PAGE gels, one was stained with Coomassie to verify equivalent amounts of substrate were utilized, and one was dried and then exposed to a phosphor screen (GE Life Sciences) for analysis of phosphorylation.

For immunoblots, samples were run on 12% SDS-PAGE gels, transferred to nitrocellulose using a Trans-Blot SD Semi-Dry system (Bio-Rad), blocked in a PBST + 5%

(w/v) non-fat milk solution, and then probed with rabbit anti-GST (1:10,000; gift from Doug Kellogg) overnight at 4°C. Blots were washed 3x for 10 minutes in PBST, probed for 1 hour using an HRP-conjugated secondary antibody (rabbit or mouse; GE aealthcare), washed 3x for 10 minutes in PBST, and then analyzed using a chemiluminescent substrate (Thermo Scientific).

ZHP-3 Mutagenesis & Purification

Two fragments of ZHP-3, the n-terminus (aa 1-173) and the c-terminus (aa 174-387), were first amplified from cDNA, and then inserted into pDONR221 via BP reaction and shuttled into pDEST15, which contains an n-termina GST tag, via LR reaction using the Gateway Cloning System (Invitrogen). Mutagenesis of MAPK phosphosites and docking site was completed using the QuickChange Site-Directed Mutagenesis Kit (Agilent). Putative phosphor-acceptors (serines/thereonines) were mutated to alanines and the putative MAPK docking site (IAQNNR) was mutated to ASQNGG to create the *zhp-3-dock* allele.

GST-tagged ZHP-3 fragments were expressed in BL21 codon plus cells (Agilent) overnight at 18°C (14-16 hours) to maintain solubility after induction with 0.2mM IPTG. Cells were lysed in a coffee grinder, resuspended in cold lysis buffer (1X PBS, 0.5% Tween-20, 1M NaCl, 10mM DTT) with protease inhibitor (1mM PMSF), sonicated, and then spun for 1 hour at 35k to clarify lysate. A glutathione agarose column (Sigma) was equilibrated in lysis buffer, the lysate was loaded, the column washed (1X PBS, 0.05% Tween-20, 0.5mM DTT, 0.25M KCl), washed a second time in the same buffer emitting detergent (Tween-20). Protein then was eluted from the column (50mM Tris pH8, 0.25M KCl, 5mM reduced glutathione) in 1mL fractions. The fractions containing protein (Bradford Assay, Bio-Rad) were combined and dialyzed overnight (50mM Hepes-KOH pH7.4, 0.25M KCl, 30% glycerol) and then aliquoted and stored at -80°C.

Viability Assays

Viability assays were performed (at 20C, unless otherwise noted) by picking L4 worms onto fresh NGM plates spread lightly with OP50 food. Worms were moved to a fresh

NGM+OP50 plate every 24 hours until egg laying ceased. Eggs were counted every 24 hours and progeny counted two days later. Viability was scored as (#progeny/#eggs) * 100.

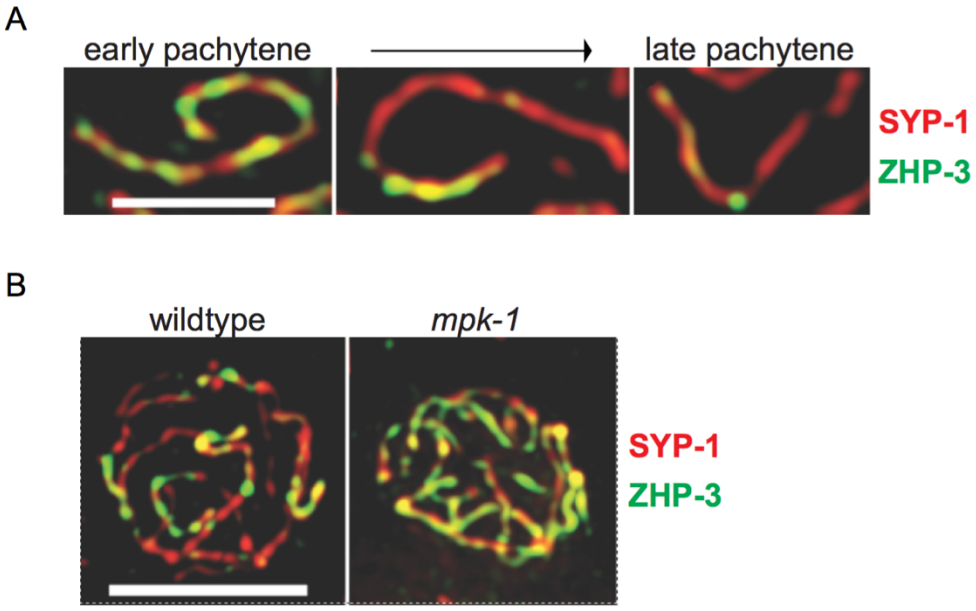

Figure 3- 1: The dynamic localization of ZHP-3 is abrogated in *mpk-1* mutants.

(A) ZHP-3 has a dynamic localization in meiotic prophase. It co-localizes with the SC component SYP-1 in early pachytene, then becomes restricted in mid-pachytene, and eventually forms foci that mark crossover sites by late pachytene. Scale bar indicates 2 micrometers. (B) Late pachytene nuclei stained for ZHP-3. In *mpk-1* mutants, ZHP-3 fails to re-localize to CO sites, instead staying fully co-localizes with the SC component SYP-1. Scale bar indicates 4 micrometers.

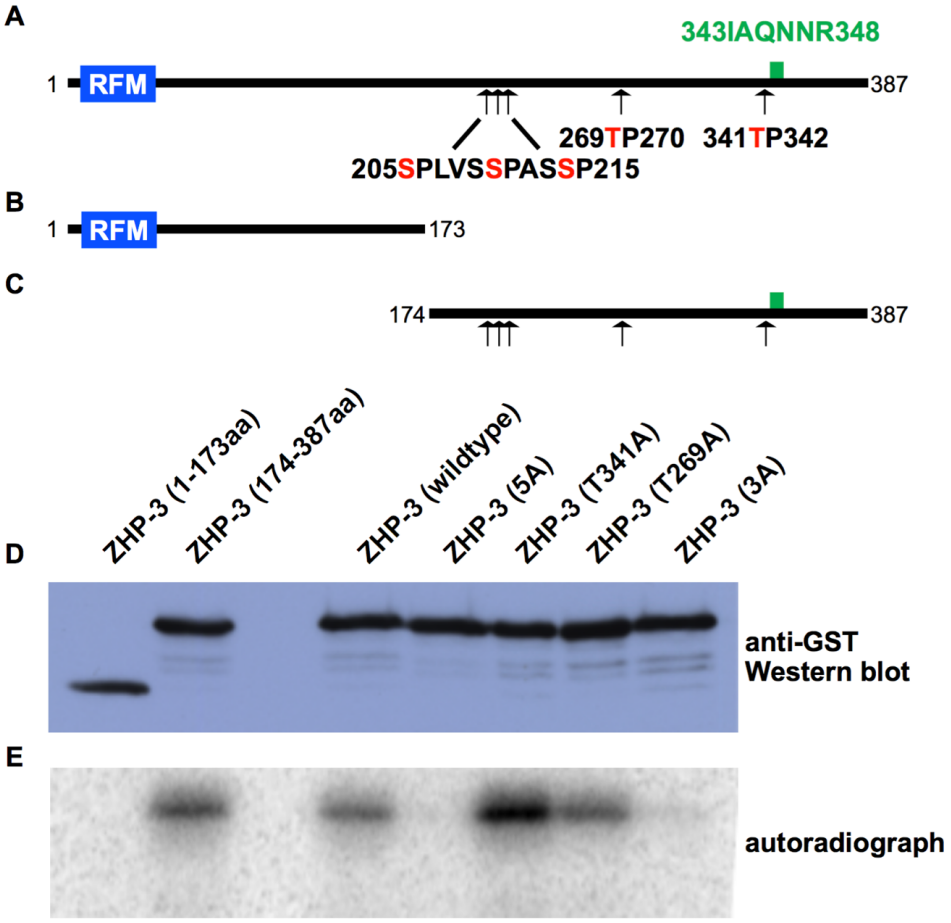

Figure 3- 2 : The C-terminus of ZHP-3 is phorpshorylated by MAPK *in vitro.*

Schematic of the ZHP-3 polypeptide, denoting the 5 putative consensus MAPK phosphorylation sites (with phosphoacceptors in red) and the putative MAPK docking site (green). (B) Schematic of N-terminal fragment of ZHP-3. (C) Schematic of C-terminal fragment of ZHP-3, containing the putative MAPK phosphorylation sites. (D) anti-GST western blot indicating relative abundance of the ZHP-3 fragments as well as phosphomutants which were utilized in a kinase assay. (E) Autoradiograph showing relative phosphorylation of each ZHP-3 mutant by recombinant MAP kinase.

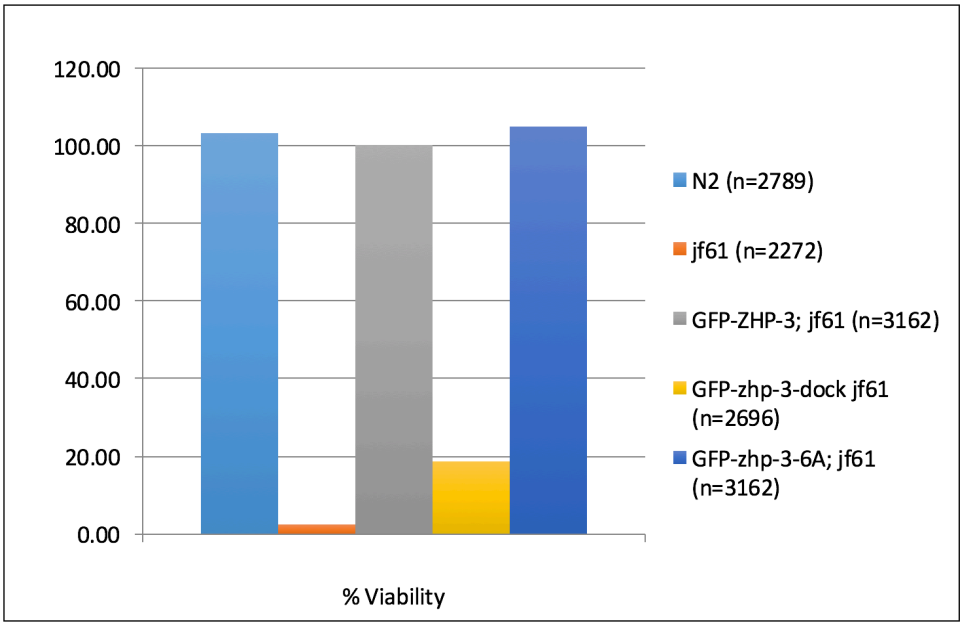

Figure 3- 3: Mutation of MAPK docking site in ZHP-3 results in embryonic lethality.

C. elegans viability is reduced to <20% in the absence of the putative ZHP-3 MAP kinase docking site. Viability was assayed in WT (N2), zhp-3 null mutants (jf61); and 3 alleles of ZHP-3 in the absence of endogenous zhp-3. GFP-ZHP-3 fully rescues the null mutation as does the GFP-ZHP-3-6A mutant, which has the putative MAPK phosphorylation sites mutated to alanine. However, the ZHP-3 mutant with mutations in the MAPK docking site cannot rescue the null allele (jf61), resulting in >80% embryonic inviability.

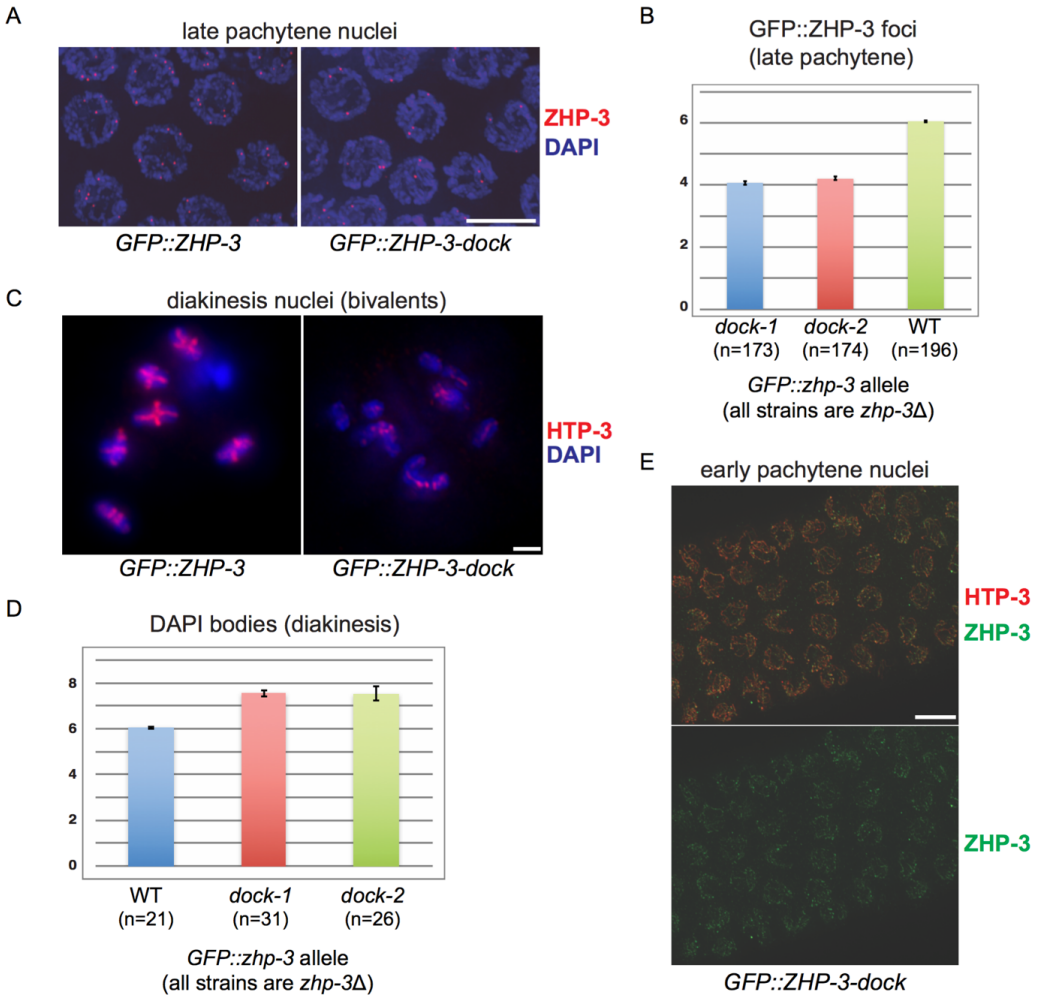

Figure 3- 4: *ZHP-dock* localizes to the SC, but is deficient in CO and bivalent formation

A. Late pachytene nuclei were stained with DAPI and a GFP antibody to recognize either GFP::ZHP-3 or GFP::zhp-3-dock. GFP::ZHP-3 forms 6 foci per nucleus, marking the CO on each of the 6 homolog pairs. The MAPK docking mutant, *GFP::zhp-3-dock* shows a reduction in foci formation. (B) Quantification from A using two unique MosSCI integrations of *GFP::zhp-3-dock*. (C) Diakinesis nuclei stained with HTP-3 & DAPI. The characteristic HTP-3 cruciform structure fails to form on all bivalents in *GFP::zhp-3-dock* mutants. (D) Quantification of the number of DAPI bodies from C. Normally 6 DAPI bodies would be present, but *GFP::zhp-3-dock* frequently shows >6, indicating at least one failed CO. (E) *GFP::zhp-3-dock co-localizes with the SC component HTP-3 in early-pachytene, indicating the protein's initial localization is similar to wildtype.*

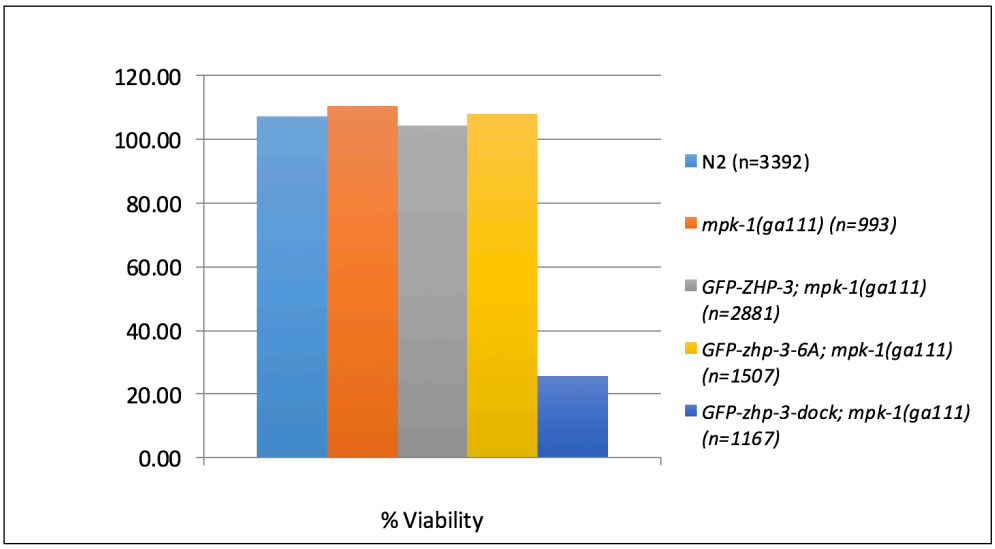

Figure 3- 5: *gfp::zhp-3* mutants show no genetic interactions with *mpk-1(ga111)* at 22C.

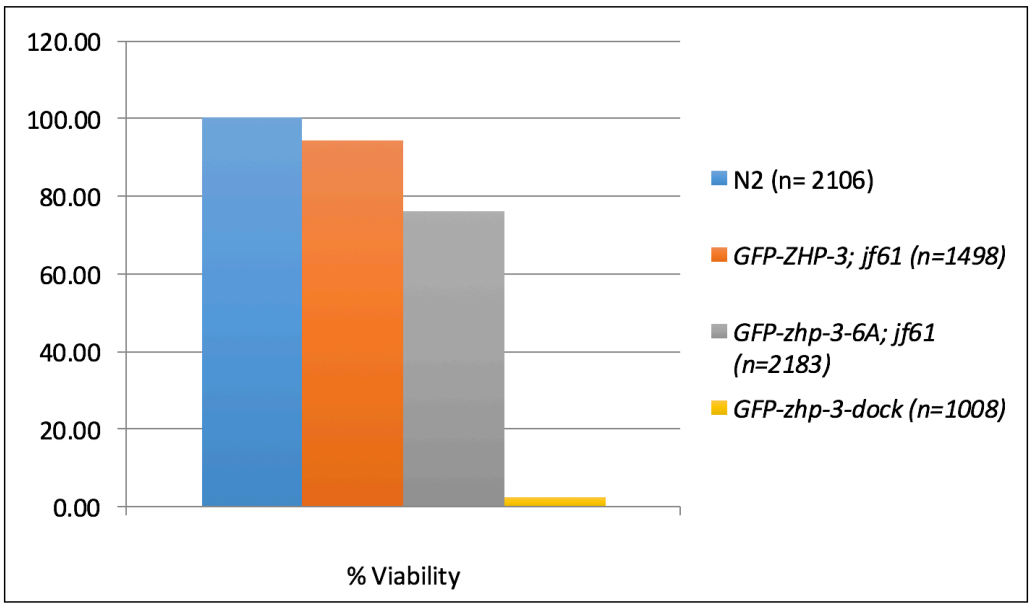

Figure 3- 6: *gfp::zhp-3* mutants are temperature sensitive (25C)

Gfp::zhp-3-dock mutants are almost completely inviable at 25C. *gfp::zhp-3-6A* mutants show a reduction in viability of nearly 25%. Wildtype *gfp::zhp-3* and N2 worms show viability near 100%.

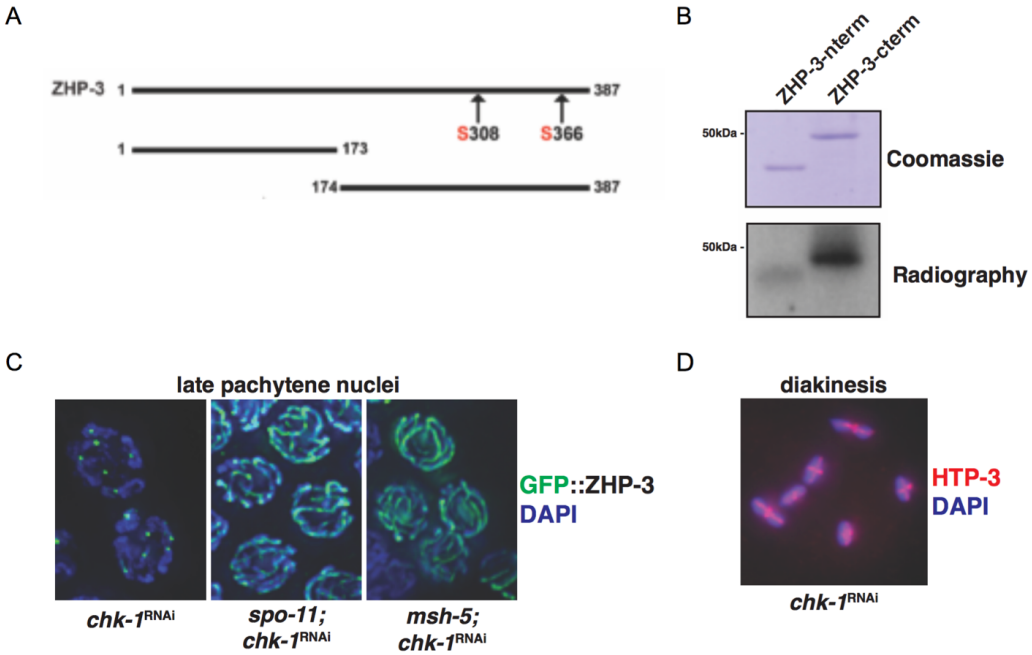

Figure 3- 7: ZHP-3 is phosphorylated by CHK-1on S308 and S366 *in vitro.*

(A) Schematic of ZHP-3 truncations. The c-terminal fragment of ZHP-3 contains two CHK-1 consensus phosphorylation sites which were phosphorylated in vitro by recombinant CHK-1, identified through mass spectrometry. (B) The c-terminus of ZHP-3 is phosphorylated by CHK-1 *in vitro*. (C) Late pachytene GFP::ZHP-3 localization after RNAi of *chk-1* in wildtype, *spo-11*, and *msh-5* mutant worms. (D) Diakinesis bivalent structures in *chk-1*RNAi germlines.

Chapter 4: The conserved ATPase TRIP13^{PCH-2} promotes Mad2 localization to unattached kinetochores in the spindle checkpoint response[1]

INTRODUCTION

Accurate chromosome segregation is essential to avoid aneuploidy, a hallmark of cancer (HOLLAND AND CLEVELAND 2012). During mitosis, replicated chromosomes must attach to microtubules emanating from opposite spindle poles (referred to as bi-orientation), so that each daughter cell receives an equivalent complement of chromosomes. To ensure the fidelity of this process, cells employ a molecular safety mechanism called the spindle checkpoint. This checkpoint monitors chromosome attachment to the mitotic spindle and delays anaphase until all chromosomes are bi-oriented, allowing time for error correction (LONDON AND BIGGINS 2014).

Mitotic chromosome segregation is choreographed by kinetochores, macromolecular protein complexes that bridge centromeric DNA with the mitotic spindle and serve as signaling platforms for the spindle checkpoint (CHEESEMAN AND DESAI 2008a; CHEESEMAN AND DESAI 2008b; FOLEY AND KAPOOR 2013a; FOLEY AND KAPOOR 2013b). When sister chromatids fail to bi-orient, spindle checkpoint components including Bub1, Bub3, Mad1, and Mad2 are hierarchically recruited to kinetochores. Kinetochores then catalyze the formation of the soluble mitotic checkpoint complex (MCC) (DE ANTONI *et al.* 2005), which in turn inhibits the anaphase promoting complex (APC/C), preventing anaphase (SUDAKIN *et al.* 2001). Mad1 plays multiple roles in checkpoint activation: it recruits Mad2 to unattached kinetochores (CHEN *et al.* 1996; BALLISTER *et al.* 2014; KUIJT *et al.* 2014) and likely promotes Mad2 activation (BALLISTER *et al.* 2014; HEINRICH *et al.* 2014; KRUSE *et al.* 2014), although this second role is less well understood. Kinetochore localization of the Mad1/Mad2 complex,

[1] The text and figures for this chapter includes contributions T. Hwang and P. Chen and are excerpted from the previously published manuscript: Nelson, C. R., Hwang, T., Chen, P.-H., & Bhalla, N. (2015). TRIP13PCH-2 promotes Mad2 localization to unattached kinetochores in the spindle checkpoint response. *The Journal of Cell Biology (211): 503-516*.

however, appears to be the determining step in checkpoint activation: artificial tethering of Mad1 to kinetochores is sufficient to both recruit Mad2 and to constitutively activate the checkpoint (MALDONADO AND KAPOOR 2011; BALLISTER *et al.* 2014; KUIJT *et al.* 2014). Furthermore, the amount of Mad2 localized to kinetochores correlates with checkpoint signal strength (COLLIN *et al.* 2013; HEINRICH *et al.* 2013). Mad2 exists in two unique conformational states: a free 'open' form (O-Mad2) and bound 'closed' form (C-Mad2) (LUO *et al.* 2002; SIRONI *et al.* 2002; LUO *et al.* 2004). Kinetochore bound C-Mad2 acts as a template to activate soluble O-Mad2, converting it to C-Mad2, a significantly more robust APC/C inhibitor (DE ANTONI *et al.* 2005). However, whether additional mechanisms regulate Mad2 dimerization at the kinetochore, and therefore the strength of the spindle checkpoint response, remains unknown.

TRIP13 is a highly conserved AAA+ ATPase that contributes to homolog pairing, synapsis, and recombination during meiosis (WU AND BURGESS 2006; JOSHI *et al.* 2009; WOJTASZ *et al.* 2009; ZANDERS AND ALANI 2009; ROIG *et al.* 2010; ZANDERS *et al.* 2011; CHEN *et al.* 2014; DESHONG *et al.* 2014; JOSHI *et al.* 2015). A large class of AAA+ ATPases is thought to remodel or disassemble protein complexes via ATP hydrolysis (DOUGAN *et al.* 2002). Specifically, TRIP13 is thought to remodel proteins containing a HORMA domain, a common structural motif found amongst checkpoint proteins, including Mad2 (ARAVIND AND KOONIN 1998; BORNER *et al.* 2008; CHEN *et al.* 2014; VADER 2015; YE *et al.* 2015). Indeed, budding yeast TRIP13 was shown to disassemble the meiotic axis component Hop1 from a DNA template *in vitro* (CHEN *et al.* 2014).

Recent studies have established an additional role for TRIP13 in regulating mitosis. These experiments have revealed that TRIP13 collaborates with the spindle checkpoint silencing protein and Mad2 inhibitor, p31(comet), to disassemble the MCC and promote anaphase (TEICHNER *et al.* 2011; TIPTON *et al.* 2012; EYTAN *et al.* 2014b; WANG *et al.* 2014b). To render MCC disassembly irreversible, TRIP13's ATPase activity converts C-Mad2 to O-Mad2. However, it can only accomplish this in the presence of p31(comet) (YE *et al.* 2015),

indicating that while C-Mad2 is the substrate for TRIP13, p31(comet) is a necessary adapter for this reaction. Interestingly, the *C. elegans* version of TRIP13, PCH-2, shows the same requirement for the presence of both proteins in stimulating its ATPase activity, suggesting a similar role in mitosis (YE *et al.* 2015).

Here, we explore the hypothesis that in addition to checkpoint silencing, TRIP13 and p31(comet) contribute to spindle checkpoint activation. Consistent with this idea, both proteins localize to kinetochores in prometaphase (HAGAN *et al.* 2011; TIPTON *et al.* 2012) and TRIP13 co-localizes with Mad2 in the presence of spindle poisons (TIPTON *et al.* 2012). Since p31(comet) can outcompete O-Mad2 for C-Mad2/Mad1 binding *in vitro* (VINK *et al.* 2006), one model proposes that p31(comet) may negatively regulate Mad2 dimerization and activation at the kinetochore and this activity must be antagonized at kinetochores during spindle checkpoint activation (MUSACCHIO AND SALMON 2007; LARA-GONZALEZ *et al.* 2012). Given that p31(comet) is bound to C-Mad2 throughout the cell cycle (DATE *et al.* 2014), another possibility is that O-Mad2 may need to be released from p31(comet) to provide a substantial pool of O-Mad2 for a robust spindle checkpoint response (YE *et al.* 2015). Given the well-characterized interaction between p31(comet) and TRIP13 during mitotic exit (TIPTON *et al.* 2012; EYTAN *et al.* 2014b; WANG *et al.* 2014b) and the biochemical ability of TRIP13 to convert C-Mad2 to O-Mad2, (YE *et al.* 2015) we reasoned that TRIP13 might contribute to these regulatory mechanisms during checkpoint activation. We set out to test this possibility in *C. elegans*.

We report the first genetic analysis of the functions of TRIP13 (PCH-2 in *C. elegans*) and p31(comet) (CMT-1 in *C. elegans*) during spindle checkpoint activation. Unlike their mammalian counterparts, loss of either TRIP13^{PCH-2} or p31(comet)$^{CMT-1}$ has no effect on mitotic timing during a normal cell cycle. However, like its human ortholog, TRIP13^{PCH-2} localizes to unattached kinetochores during spindle checkpoint activation. Furthermore, TRIP13^{PCH-2} is required for spindle checkpoint activation in two cell types in *C. elegans*: germline mitotic cells and cells undergoing embryonic divisions. We demonstrate that the

function of TRIP13^{PCH-2} in the checkpoint is to promote Mad2 (MDF-2/MAD-2 in *C. elegans*) localization to kinetochores, as Mad2 levels are markedly reduced at unattached kinetochores in *pch-2* mutant embryos. The localization of Mad1, Bub1, and Bub3 (MAD-1/MDF-1, BUB-1, and BUB-3 respectively in *C. elegans*) are unaffected by mutation of *pch-2*, indicating that the role for TRIP13^{PCH-2} in the checkpoint is limited to regulating Mad2. TRIP13^{PCH-2} modulates Mad2 via p31(comet)$^{CMT-1}$. TRIP13^{PCH-2} and p31(comet)$^{CMT-1}$ physically interact via yeast two-hybrid and both p31(comet)$^{CMT-1}$ and Mad2 are required for TRIP13^{PCH-2} localization to unattached kinetochores. Finally, our data show that TRIP13^{PCH-2} genetically antagonizes p31(comet)$^{CMT-1}$ during checkpoint activation: mutation of *cmt-1* partially suppresses the defects in both checkpoint signaling and Mad2 recruitment observed in *pch-2* mutants. Taken together, these data suggest a model in which TRIP13^{PCH-2} regulates spindle checkpoint activation by disassembling a p31(comet)$^{CMT-1}$/Mad2 complex, promoting Mad2 localization to kinetochores and activation of the checkpoint.

RESULTS

PCH-2 is required for spindle checkpoint activation

First, we tested whether PCH-2 regulates the duration of mitosis in the mitotic region of the *C. elegans* germline, as has been shown in mammalian cells (WANG *et al.* 2014b). We measured the mitotic index in this region by assaying the number of nuclei positive for phosphorylation of histone H3 serine 10 (phospho-H3S10; Figure 4-1A) in wildtype, *pch-2* mutants and *mad-1* mutants. A null allele of *pch-2*, *pch-2(tm1458)* (BHALLA AND DERNBURG 2005), and a hypomorphic allele of *mad-1*, *mdf-1(av19)* (STEIN *et al.* 2007), were used for all analyses. The *mad-1(av19)* allele contains a point mutation in the MAD-2 binding motif that specifically affects MAD-1's checkpoint function (STEIN *et al.* 2007; MOYLE *et al.* 2014). To ensure that our analysis was limited to mitotic cells, we also stained germlines with an antibody against phosphorylated SUN-1, which delineates meiotic entry (phospho-SUN-1-S8; Figure 4-1A) (PENKNER *et al.* 2009; BURGER *et al.* 2013). We did not detect an increase in the

mitotic index of *pch-2* mutant germlines as compared to wildtype or *mad-1* mutants (Figure 4-1B), suggesting that germline mitotic timing is not significantly altered by deletion of *pch-2*.

Next, we evaluated whether PCH-2 was required for the spindle checkpoint in the mitotic region of the germline. The checkpoint can be activated in this region using the temperature sensitive allele *zyg-1(b1),* referred to here as *zyg-1*^{ts}. ZYG-1 is an essential regulator of centrosome duplication in *C. elegans* and inactivation of *zyg-1*^{ts} at the non-permissive temperature creates monopolar spindles (O'CONNELL *et al.* 2001). This defect in spindle formation delays, but doesn't permanently arrest, mitosis in germline nuclei and is dependent on the spindle checkpoint (STEVENS *et al.* 2013). As a result, the mitotic index of *zyg-1*^{ts} worms shifted to the non-permissive temperature for 24 hours was significantly increased compared to wildtype worms (Figure 4-1A&B). As expected, this increase was dependent on MAD-1 (Figure 4-1B; Figure 4-2A). Mutation of *pch-2* also decreased the mitotic index to wildtype levels in *zyg-1*^{ts} germlines, mirroring the *mad-1* mutant phenotype (Figure 4-1B; Figure 4-2A). Thus, PCH-2 is required for the mitotic delay induced by the spindle checkpoint in the *C. elegans* germline.

Given that PCH-2 function is well characterized in the germline (DESHONG *et al.* 2014), we were curious if its checkpoint function is conserved in other cellular contexts. To investigate this possibility, we utilized the two-cell embryo, as the spindle checkpoint has been well characterized during *C. elegans* embryogenesis (ENCALADA *et al.* 2005; ESSEX *et al.* 2009; MOYLE *et al.* 2014). The egg shell renders the embryo largely impenetrable to drug treatment (CARVALHO *et al.* 2011) and spindle checkpoint activation does not appear to occur during normal embryonic divisions (ESSEX *et al.* 2009). Thus, we again relied upon genetic perturbations to activate the spindle checkpoint. We generated a feeding RNA interference (RNAi) vector that inactivated the *zyg-1* gene. We fed worms bacteria expressing this vector for 24 hours and verified that monopolar spindles were present in the two-cell embryo (Figure 4-2B), consistent with previous analysis (ESSEX *et al.* 2009).

To analyze mitotic timing during embryogenesis, we took advantage of an assay developed by Essex and colleagues (ESSEX *et al.* 2009): DNA was visualized with an mCherry tagged version of histone H2B (mCh::H2B) and the plasma membrane with a GFP tagged plasma membrane marker (GFP::PH). We measured mitotic timing from nuclear envelope breakdown (NEBD), defined as a diffusion of mCh::H2B from the nucleoplasm, to the onset of cortical contractility (OCC), defined by a change in conformation of the plasma membrane from circular to rectangular (Figure 4-1C). In embryos with monopolar spindles induced by *zyg-1* RNAi, OCC is defined as the formation of a persistent membrane bleb (or blebs) between the anterior (AB) and posterior (P_1) cells (arrows, Figure 4-1C). OCC is concomitant with mitotic exit and is used as a marker for live microscopy (CANMAN *et al.* 2000). All further mitotic timing and localization analyses were performed in the AB cell, which enters mitosis prior to the P_1 cell (BAO *et al.* 2008).

We first tested whether PCH-2 regulates mitotic timing in the two-cell embryo. We found that an unperturbed wildtype mitosis lasted an average of 183 seconds (Figure 4-1D; Supplemental Movie 1). Average mitotic timing in *mad-1* mutants (176 seconds) and *pch-2* mutants (177 seconds; Supplemental Movie 2) was no different than wildtype (Figure 4-1D), consistent with our analysis of mitotic index in germline mitotic nuclei (Figure 4-1B). Activation of the spindle checkpoint via *zyg-1* RNAi *(zyg-1^{RNAi})* caused a statistically significant delay in average mitotic timing in otherwise wildtype embryos (300 seconds; p-value <0.0001; Supplemental Movie 3) (Figure 4-1D). However, when *zyg-1* was knocked down by RNAi in either *mad-1* or *pch-2* mutant embryos, we did not observe a delay in mitotic timing (mean of 188 seconds and 186 seconds, respectively; p-values <0.0001; Supplemental Movie 4) (Figure 4-1D). Taken together, these data indicate that PCH-2 does not regulate mitotic timing in the mitotic germline or in the developing embryo. Instead, PCH-2 is required for spindle checkpoint activation in two mitotic cell types: the developing embryo and the mitotic germline.

PCH-2 is required for robust MAD-2 accumulation at unattached kinetochores

We further investigated the loss of checkpoint function in *pch-2* mutants. Given the evidence that PCH-2 regulates HORMA-domain containing proteins (BORNER *et al.* 2008; CHEN *et al.* 2014; DESHONG *et al.* 2014; YE *et al.* 2015), we analyzed the localization of the HORMA-domain protein MAD-2. *C. elegans* chromosomes are holocentric and localize kinetochore proteins and checkpoint components along their entire lengths (OEGEMA *et al.* 2001; ESSEX *et al.* 2009). MAD-2 only localizes to kinetochores during checkpoint activation and specifically localizes to the unattached side of the pseudo-metaphase plate (ESSEX *et al.* 2009) (Figure 4-3A). As expected, GFP::MAD-2 showed robust localization to unattached kinetochores when the checkpoint was activated in embryos via *zyg-1* RNAi (Figure 4-3A). In *pch-2* mutants, we observed either little (*pch-2*) or no (*pch-2*†) GFP::MAD-2 localized to unattached kinetochores (Figure 2A). We quantified this defect and found that kinetochore localized GFP::MAD-2 signal was reduced by an average of 82% in *pch-2* mutants (Figure 4-3B). By contrast, GFP::MAD-2 kinetochore signal was reduced by an average of 97% in *mad-1* mutant embryos (Figure 4-3A&B), indicating that the genetic lesion in *mad-1(av19)* is sufficient to abolish MAD-2 kinetochore recruitment. Therefore, PCH-2 is required for full recruitment of MAD-2 at unattached kinetochores. However, MAD-2 signal was not completely ablated as in *mad-1* mutants.

We considered the possibility that PCH-2 may support stability of the MAD-2 protein. To test this, we analyzed MAD-2 protein levels by immunoblotting serial dilutions of whole worm lysates. We reproducibly saw no defect in the level of MAD-2 protein in *pch-2* mutants as compared to wildtype (Figure 4-3C). We quantified MAD-2 protein levels in *pch-2* mutants using multiple immunoblots and found MAD-2 protein levels to be essentially identical to wildtype (102% of wildtype; Figure 4-3D), indicating that the loss of MAD-2 kinetochore localization in *pch-2* mutants is not simply a secondary consequence of decreased protein level.

Loss of MAD-2 at kinetochores in *pch-2* mutants could be due to direct regulation of MAD-2 by PCH-2, or an indirect consequence due to failed kinetochore assembly or the failure to recruit other checkpoint components. We explored these latter hypotheses. KNL-1 is a member of the outer kinetochore KMN network which is responsible for kinetochore-microtubule binding as well as the loading of checkpoint components (DESAI *et al.* 2003; CHEESEMAN *et al.* 2006; LONDON *et al.* 2012; SHEPPERD *et al.* 2012; YAMAGISHI *et al.* 2012). We analyzed the localization of KNL-1::GFP in *pch-2* mutants and found that KNL-1 loaded properly onto mitotic chromosomes, indicating that *pch-2* mutants do not have significant defects in kinetochore assembly (Figure 4-4A). Furthermore, *pch-2* mutants are fully viable (DESHONG *et al.* 2014), indicating that gross chromosome segregation defects are unlikely. MAD-1 is the receptor for MAD-2 at kinetochores (CHEN *et al.* 1996; CHEN *et al.* 1998). We analyzed GFP::MAD-1 localization to unattached kinetochores in *pch-2* mutants treated with *zyg-1* RNAi (Figure 2E). Quantification of GFP::MAD-1 signal at unattached kinetochores showed that *pch-2* mutants localize comparable amounts of GFP::MAD-1 as compared to wildtype (110% of wildtype; Figure 4-3F). This indicates that the loss of MAD-2 at kinetochores in *pch-2* mutants is not due to a failure to localize its receptor. Similarly, localization of the checkpoint components BUB-1::GFP and GFP::BUB-3 were unaffected by deletion of *pch-2* (Figure 4-4B). Together, these data demonstrate that PCH-2 is required for robust accumulation of MAD-2 at kinetochores during the spindle checkpoint response and strongly suggest that PCH-2 directly regulates either MAD-2 or a MAD-2 containing protein complex during checkpoint activation.

PCH-2 localizes to unattached kinetochores in the spindle checkpoint response

We previously showed that PCH-2 localizes to chromosomes during meiotic prophase (DESHONG *et al.* 2014). However, its expression and localization during mitosis have not been explored in *C. elegans*. To analyze PCH-2 localization in live embryos, we inserted a C-terminal *gfp-3xflag* tag at the endogenous *pch-2* locus using CRISPR/Cas9 genome editing (DICKINSON *et al.* 2013; PAIX *et al.* 2014). We verified insertion of the tag via immunoblot

(Figure 4-5A) and then tested whether embryos expressing PCH-2::GFP-3XFLAG were competent for spindle checkpoint activation using DCON as a marker of mitotic exit (Figure 4-6A). Mitotic timing in control embryos averaged 281 seconds and *zyg-1 RNAi* produced a significant delay (average 440 seconds; p-value < 0.0001). *zyg-1 RNAi* also significantly delayed mitosis in embryos expressing PCH-2::GFP-3XFLAG from an average of 265 seconds to 420 seconds (p-value <0.0001). Thus, embryos expressing PCH-2::GFP-3XFLAG are competent for spindle checkpoint activation.

Next, we monitored PCH-2::GFP-3XFLAG localization using live microscopy. In embryos exposed to *zyg-1* RNAi, PCH-2::GFP-3XFLAG was excluded from nuclei prior to NEBD (P1 cell; arrow; Figure 4-5B), and then became enriched in the "cloud" surrounding mitotic chromatin after NEBD (AB cell; arrowhead; Figure 4-5B). This localization is identical to that of MAD-2, which is excluded from the nucleoplasm until NEBD and then becomes enriched around chromatin (ESSEX *et al.* 2009). We detected a similar localization pattern in wildtype embryos (data not shown). When chromosomes formed a pseudo-metaphase plate in *zyg-1*^{RNAi} embryos, PCH-2::GFP-3XFLAG localized to unattached kinetochores (right panels; Figure 4-5B), mirroring the localization of MAD-2 (Figure 4-3A) and MAD-1 (Figure 4-3E). Moreover this recruitment to unattached kinetochores exhibited similar timing as MAD-1 and MAD-2, occurring an average of 60 seconds after NEBD (data not shown). This is unique from other checkpoint components, such as BUB-1 and BUB-3, which become highly enriched on kinetochores immediately upon NEBD in *C. elegans* (ESSEX *et al.* 2009). Thus, PCH-2 localizes to unattached kinetochores during checkpoint activation, similar to its mammalian counterpart TRIP13, and with kinetics similar to that of MAD-1 and MAD-2.

CMT-1 and MAD-2 are required for PCH-2 localization to unattached kinetochores

Given the failure of *pch-2* mutants to localize MAD-2 during checkpoint activation, we were curious if PCH-2 might directly interact with MAD-2. To test this, we performed a directed yeast-two hybrid screen, using PCH-2 as bait, and a library of known kinetochore and checkpoint components as the prey (MOYLE *et al.* 2014) . We failed to detect an

interaction between PCH-2 and MAD-2 or any other of the other proteins in the library (data not shown).

Recently, the mammalian ortholog of PCH-2, TRIP13, was shown to interact with the MAD-2 inhibitor p31(comet) *in vitro* (TIPTON *et al.* 2012). CMT-1 is the *C. elegans* ortholog of p31(comet) (VLEUGEL *et al.* 2012). While CMT-1 function during *C. elegans* mitosis has not been well characterized, *cmt-1* mutants are viable and fertile (data not shown), suggesting no major defects during embryogenesis or germline development. CMT-1, like MAD-2, contains a HORMA domain (YANG *et al.* 2007), suggesting PCH-2 may regulate it directly. Using the yeast two-hybrid assay, we detected a robust interaction between PCH-2 and CMT-1 (Figure 4-7A).

Given this interaction, we reasoned that CMT-1 might be responsible for the kinetochore localization of PCH-2 during checkpoint activation. We analyzed the localization of PCH-2::GFP-3XFLAG in wildtype and *cmt-1* mutant embryos treated with *zyg-1* RNAi. In contrast to wildtype embryos which effectively localized PCH-2::GFP-3XFLAG, the enrichment of PCH-2 at unattached kinetochores was lost in *cmt-1* mutant embryos (Figure 4-7B). We quantified the PCH-2::GFP-3XFLAG kinetochore signal and found that it was reduced to 14% of wildtype in *cmt-1* mutants (Figure 4-7C), indicating that CMT-1 is required for the localization of PCH-2 to unattached kinetochores. Given that TRIP13^{PCH-2}, p31(comet)$^{CMT-1}$, and MAD-2 were shown to form a complex *in vitro* (YE *et al.* 2015), we reasoned that PCH-2 localization to unattached kinetochores might also depend on MAD-2. To test this, we again utilized the *mad-1(av19)* allele, which fails to localize MAD-2 to kinetochores (Figure 4-3A). Similar to *cmt-1* mutants, PCH-2::GFP-3XFLAG did not become enriched at unattached kinetochores in *mad-1(av19)* mutants (Figure 4-7B) and quantification indicated that PCH-2 kinetochore signal was reduced to 10% of wildtype (Figure 4-7C). Thus, both CMT-1 and MAD-2 are required for PCH-2 localization at unattached kinetochores, consistent with their ability to form a complex *in vitro* (YE *et al.* 2015).

Mutation of cmt-1 supresses the pch-2 checkpoint defect

Since the localization of PCH-2 to unattached kinetochores requires CMT-1, we assessed how mutation of *cmt-1* affected the spindle checkpoint. We used a null allele of *cmt-1*, *cmt-1(ok2879),* for all analyses. We again assessed mitotic timing during embryogenesis. Unlike in mammalian cells, where p31(comet) is required for efficient mitotic exit (XIA *et al.* 2004), *cmt-1* single mutants exhibited wildtype rates of mitotic timing (Figure 4-9A; Supplemental Movie 5), similar to our analysis of *pch-2* mutants. This result indicates that neither PCH-2 nor CMT-1 regulate mitotic timing in a normal cell cycle in *C. elegans*.

Next, we analyzed mitotic timing in *cmt-1* mutants in the context of spindle checkpoint activation. The majority of *cmt-1* mutant embryos were competent for checkpoint activation: the average length of mitosis in *cmt-1*;*zyg-1*^{RNAi} embryos was significantly longer than wildtype embryos (Figure 4-9A; 277 seconds; p-value < 0.0001; Supplemental Movie 6), similar to *zyg-1*^{RNAi} embryos (300 seconds). However, overall, the distribution of mitotic timing in *cmt-1*;*zyg-1*^{RNAi} embryos was broader and shifted lower compared to RNAi of *zyg-1* alone. Furthermore, a small population (7/28; 25%) of *cmt-1;zyg-1*^{RNAi} mutant embryos showed wildtype mitotic timing ($\leq$222 seconds, below the gray dashed line; Supplemental Movie 7), which we never observed in *zyg-1*^{RNAi} embryos (0/19; 0%). Therefore, mutation of *cmt-1* appears to reduce spindle checkpoint robustness. Moreover, since *cmt-1* mutants fail to localize PCH-2 to unattached kinetochores (Figure 4-9B), these data also demonstrate that kinetochore localization of PCH-2 is not strictly required for checkpoint activation when CMT-1 is absent.

Since the checkpoint was largely functional in *cmt-1* mutants despite the absence of PCH-2::GFP-3XFLAG at unattached kinetochores (Figure 4-9B), we wondered whether checkpoint activation in *cmt-1* mutants required PCH-2 at all. We monitored mitotic timing in *cmt-1;pch-2* double mutants in the absence and presence of *zyg-1* RNAi. Untreated double mutants exhibited wildtype mitotic timing (average 188 seconds; Supplemental Movie 8). Strikingly, most *cmt-1;pch-2;zyg-1*^{RNAi} mutant embryos were functional for checkpoint

activation, exhibiting average mitotic timing similar to *zyg-1*^{RNAi} embryos (Figure 4-9A; 283 seconds; Supplemental Movie 9). Again, however, like *cmt-1*;*zyg-1*^{RNAi} embryos, the distribution of mitotic timing was broader and shifted lower compared to *zyg-1*^{RNAi} embryos. Likewise, a small fraction (4/24; 16.7%) of *cmt-1;pch-2;zyg-1*^{RNAi} embryos went through mitosis in 222 seconds or less, indicating a subtle checkpoint defect (Supplemental Movie 10). Importantly, however, average mitotic timing in *cmt-1;pch-2;zyg-1*^{RNAi} mutants was significantly longer than *pch*-2;*zyg-1*^{RNAi} mutants (p-value< 0.0001). Altogether, our results show that CMT-1 and PCH-2 interact both physically and genetically. More specifically, mutation of *cmt-1* partially restores checkpoint function in *pch-2* mutants, indicating that CMT-1 function is antagonized by PCH-2 function during spindle checkpoint activation.

We were curious why checkpoint function was slightly reduced in both *cmt-1* and *cmt-1;pch-2* mutants (Figure 4-9A). We reasoned that MAD-2 protein levels might be affected by mutation of *cmt-1*. We qualitatively and quantitatively assessed MAD-2 protein levels in these genetic backgrounds (Figure 4-9B&C; Figure 4-10A). *cmt-1* mutants and *cmt-1*;*pch-2* double mutants showed reductions in MAD-2 protein levels of approximately 61% and 42%, respectively (Figure 4-9C). This suggests that CMT-1 may play a secondary role in stabilizing the MAD-2 protein, perhaps through a direct interaction. This reduction in MAD-2 protein level may also explain the defect in checkpoint robustness observed in the *cmt-1* genetic background.

Given the reduction in MAD-2 protein levels we detected in *cmt-1;pch-2* double mutants, we wondered if the mitotic delay induced by *zyg-1* RNAi that we observed in this background was indeed due to spindle checkpoint activation (Figure 4-9A). To test this, we created c*mt-1;pch-2*;*mad-2* triple mutants for mitotic timing analyses. However, these triple mutants produced no viable embryos for analysis (data not shown). To circumvent this genetic interaction, we performed sequential feeding RNAi of *mad-2* and *zyg-1*. We verified this scheme was sufficient for checkpoint activation and that RNAi of *mad-2* was sufficient to disable the checkpoint. RNAi of both *mad-2* and *zyg-1* in wildtype embryos decreased mitotic

timing to an average of 175 seconds, substantially lower than the average mitotic timing of embryos in which only *zyg-1* was inactivated (Figure S4B; p-value < 0.0001). Similarly, RNAi of both *zyg-1* and *mad-2* in *cmt-1;pch-2* mutants significantly reduced mitotic timing to an average of 189 seconds, compared to the average of 262 seconds observed in *zyg-1*^{RNAi} embryos (Figure 4-10B; p-value = 0.008). These data show that the mitotic delay observed in *cmt-1;pch-2;zyg-1*^{RNAi} embryos is dependent on MAD-2, and, by extension, the spindle checkpoint. Despite expressing approximately 42% of the amount of MAD-2 protein of wildtype embryos, *cmt-1;pch-2* double mutants effectively activate the spindle checkpoint in a majority of embryos.

Since mutation of *cmt-1* in *pch-2* mutant embryos rescued checkpoint function despite the reduced levels of MAD-2, we evaluated whether MAD-2 localization to unattached kinetochores was restored in these mutants as well. GFP::MAD-2 localized to unattached kinetochores in *cmt-1;zyg-1*^{RNAi} mutants, though less robustly than in *zyg-1*^{RNAi} embryos (Figure 4-9D). When we quantified the amount of kinetochore bound GFP::MAD-2, *cmt-1;zyg-1*^{RNAi} mutants exhibited 53% of the level of GFP::MAD-2 at kinetochores observed in *zyg-1*^{RNAi} embryos (Figure 4-9E). Consistent with our mitotic timing analysis, mutation of *cmt-1* partially rescued GFP::MAD-2 localization in *pch-2* mutants (Figure 4-9D). Kinetochore bound GFP::MAD-2 levels in *cmt-1;pch-2;zyg-1*^{RNAi} mutant embryos were 58% of the level of GFP::MAD-2 at kinetochores observed in *zyg-1*^{RNAi} embryos (Figure 4-9E). Similar to *pch-2* mutants, we detected no defects in the localization of GFP::MAD-1 in *cmt-1* or *cmt-1;pch-2* double mutants (Fig 4-10A). Furthermore, kinetochore assembly, as visualized by KNL-1::GFP loading was unaffected by mutation of *cmt-1* (Figure 4-4C). Finally, BUB-1::GFP and GFP::BUB-3 localized to kinetochores normally in *cmt-1* mutants (Figure 4-4B). Thus, while MAD-2 protein levels are most profoundly affected in *cmt-1;pch-2* double mutants (Figure 4-9C; Figure 4-8A), they are generally competent for checkpoint activation (Figure 4-9A) and localize functional amounts of GFP::MAD-2 to kinetochores (Figure 4-9D&E). Together, these data strongly argue that the primary role for PCH-2 during checkpoint activation is to

antagonize CMT-1 in order to promote the robust accumulation of MAD-2 at unattached kinetochores.

Our analyses of MAD-2 localization used a GFP::MAD-2 construct driven from a non-native promoter in a strain that also includes endogenous MAD-2. MAD-2 protein levels are higher in this genetic background and this increase in MAD-2 levels bypasses the requirement for other checkpoint components, such as MAD-3 (SAN-1 in *C. elegans*) and BUB-3 (ESSEX *et al.* 2009). We were curious if over-expression of MAD-2 would also bypass the requirement for PCH-2 in checkpoint activation. To test this, we analyzed mitotic timing in GFP::MAD-2 embryos using chromosome decondensation (DCON) as a marker of mitotic exit as the presence of GFP::MAD-2 in this strain prevented us from using GFP::PH. RNAi of *zyg-1* induced a statistically significant mitotic delay in GFP::MAD-2 embryos (mean 460 seconds; *zyg-1*^{RNAi}) versus control RNAi (mean 274 seconds; p-value <0.0001; Figure 4-10A). Mutation of *pch-2* in GFP::MAD-2 embryos with *zyg-1* RNAi reduced mitotic timing to an average of 300 seconds, which was significantly different than GFP::MAD-2;*zyg-1*^{RNAi} embryos (Figure 4-10A; p-value <0.0001). Furthermore, much like endogenous MAD-2, we couldn't detect any difference in the level of the GFP::MAD-2 protein in *pch-2* mutants (Figure 4-10B). These results indicate that overexpression of MAD-2 in *pch-2* mutants is not sufficient to overcome the *pch-2* checkpoint defect, lending additional support to our hypothesis that PCH-2 plays a more direct role in localizing MAD-2 to kinetochores.

Finally, given that MAD-2 levels are dramatically reduced in *cmt-1* and *cmt-1;pch-2* mutants (Figures 4-9B&C; Figure 4-8A) and the checkpoint appears less robust in these backgrounds (Figure 4-9A), we wondered if MAD-2 overexpression could restore checkpoint robustness in these strains. Even though endogenous MAD-2 levels were reduced in *cmt-1* and *cmt-1;pch-2* mutants, GFP::MAD-2 was expressed at similar levels to wildtype (Figure 4-10B). However, after *zyg-1* RNAi, mitotic timing in both *cmt-1* and *cmt-1; pch-2*, while significantly different than pch-2 mutants (p-value<0.001), was still reduced compared to *zyg-1*^{RNAi} alone (Figure 4-10A). Furthermore, the distribution of mitotic timing still appeared slightly

broader. Taken together, these data indicate that overexpression of MAD-2 in the *cmt-1* background may not be sufficient to rescue checkpoint robustness.

Discussion

The spindle checkpoint, once thought to display switch-like "on" or "off" behavior, is now thought to generate a more dynamic response, which can vary in strength (LONDON AND BIGGINS 2014). In particular, the strength of the checkpoint response correlates with the amount of kinetochore-bound Mad2 (COLLIN *et al.* 2013). Here, we have shown that TRIP13^{PCH-2} regulates Mad2 recruitment to unattached kinetochores, independent of Mad1, by antagonizing p31(comet)$^{CMT-1}$ during the spindle checkpoint response in *C. elegans.* Thus, TRIP13^{PCH-2} represents an ideal candidate as a checkpoint robustness factor through it's regulation of the p31(comet)$^{CMT-1}$/Mad2 complex. Our analysis may appear contradictory to the characterization of these factors as collaborators during checkpoint silencing and mitotic exit. However, these two roles can be reconciled when considering TRIP13^{PCH-2}'s *in vitro* biochemical activity: disassembly of the p31(comet)/Mad2 complex (YE *et al.* 2015). During checkpoint silencing and mitotic exit, this activity contributes to irreversibly inactivating the MCC (EYTAN *et al.* 2014b). During checkpoint activation, our data suggest that this same biochemical activity is utilized in a unique context, promoting Mad2 localization to unattached kinetochores and anaphase delay.

Our data suggest the existence of a regulatory mechanism that follows the initial recruitment of Mad1/ Mad2 at unattached kinetochores during checkpoint activation in *C. elegans*. *pch-2* mutants show reduced kinetochore recruitment of Mad2. However, *pch-2* mutants recruit Mad2 at levels higher than in *mad-1* mutants, which effectively have no kinetochore bound Mad2 (Figure 2B). According to the template model (DE ANTONI *et al.* 2005), kinetochore associated C-Mad2 is bound to Mad1 and exhibits slower turnover (SHAH *et al.* 2004), providing the template for dimerization and activation of free O-Mad2. This pool of activated C-Mad2 exhibits rapid turnover to generate a potent cytosolic wait anaphase signal (HOWELL *et al.* 2004; SHAH *et al.* 2004). Mad2 activation via its dimerization appears to

be a conserved mechanism of checkpoint activation (NEZI AND MUSACCHIO 2009). Our quantitative Mad2 analysis suggests that the basal Mad1/ Mad2 complex may still be recruited in *pch-2* mutants, but that subsequent Mad2 dimerization and turnover may be disrupted. Therefore, we suggest that TRIP13^{PCH-2} is not simply regulating gross Mad2 kinetochore recruitment, but instead the ability of cytosolic O-Mad2 to dimerize with C-Mad2 and convert to C-Mad2, in order to produce the soluble "wait anaphase" signal.

We offer two models to explain how TRIP13^{PCH-2} may regulate a p31(comet)$^{CMT-1}$/Mad2 complex to promote spindle checkpoint signaling at unattached kinetochores. Our first model is based on the proposed idea that p31(comet)$^{CMT-1}$ "caps" the stable Mad1/C-Mad2 complex at unattached kinetochores to limit checkpoint signaling in prometaphase (MUSACCHIO AND SALMON 2007; LARA-GONZALEZ *et al.* 2012). In this model, TRIP13^{PCH-2} would be responsible for removing the inhibitory p31(comet)$^{CMT-1}$ "cap" to allow Mad2 dimerization, additional C-Mad2 production, and checkpoint activation (Figure 4-11A; Model 1). This model is consistent with our data showing that TRIP13^{PCH-2} localization to kinetochores during checkpoint activation depends on p31(comet)$^{CMT-1}$. However, this model does not adequately explain the minor checkpoint defect observed in *cmt-1* mutants, as removal of the C-Mad2 "cap" would not be predicted to reduce Mad2 stability or checkpoint robustness.

Our second model is informed by the recent papers that describe the biochemical roles of p31(comet)$^{CMT-1}$ and TRIP13^{PCH-2} in mitotic exit in mammalian cells (EYTAN *et al.* 2014b; YE *et al.* 2015). Combined, these papers present data that p31(comet)$^{CMT-1}$ and TRIP13^{PCH-2} collaborate in a two-step reaction to disassemble C-Mad2 from the MCC via ATP hydrolysis, generating free O-Mad2. In particular, Ye and colleagues argue that p31(comet)$^{CMT-1}$ acts as an adapter, enabling TRIP13^{PCH-2} to catalyze the conformational switch of C-Mad2 to O-Mad2 (YE *et al.* 2015) . Since p31(comet)$^{CMT-1}$ and Mad2 interact throughout the cell cycle in mammalian cells (DATE *et al.* 2014), it's possible that this dimer must be disassembled to generate sufficient O-Mad2 to allow for robust checkpoint activation. Thus, our second model proposes that TRIP13^{PCH-2} specifically disassembles a p31(comet)$^{CMT-1}$/Mad2 complex to

provide free O-Mad2 for the template reaction, thereby amplifying the checkpoint signal (Figure 4-11A; Model 2). This model is consistent with the complete lack of checkpoint activity in *pch-2* mutants, as CMT-1 may sequester MAD-2 in this mutant background. Furthermore, this model could explain the reduction in Mad2 protein levels in *cmt-1* mutants (Figure 4-9B; Figure 4-8A), particularly if the formation of a p31(comet)$^{CMT-1}$/Mad2 complex contributes to Mad2 stability. This model is also consistent with data showing that p31(comet)$^{CMT-1}$ rapidly cycles on and off of unattached kinetochores in mammalian cells (HAGAN *et al.* 2011), similar to the highly mobile population of Mad2. However, this disassembly reaction may not necessarily need to occur at unattached kinetochores, as *cmt-1* mutants abolish PCH-2 localization (Figure 4-8C) while maintaining an active spindle checkpoint (Figure 4-9A). In addition, it should be noted that these two models are not mutually exclusive, raising the possibility that TRIP13^{PCH-2} undertakes both of these tasks to promote checkpoint activation in *C. elegans*.

The mitotic delay induced by the spindle checkpoint in the *C. elegans* embryo is relatively short compared to its mammalian counterpart. This may be a consequence of prioritizing the coordination of mitotic divisions over responding to cell cycle defects during embryonic development, or due to the large cytoplasmic to nuclear ratio that has been shown to affect checkpoint signaling in other systems, or both (MINSHULL *et al.* 1994; BAO *et al.* 2008). These factors may also explain why TRIP13^{PCH-2} and p31(comet)$^{CMT-1}$ appear to be dispensable for regulating normal mitotic timing in *C. elegans.* It is formally possible, however, that TRIP13^{PCH-2} is required for checkpoint silencing in *C elegans* as in mammalian cells (EYTAN *et al.* 2014b). Our ability to detect this function may simply be masked by the lack of a functional checkpoint in the absence of TRIP13^{PCH-2}. Still, our experiments demonstrate that mitotic divisions in *C. elegans*, both in the context of germline mitosis and embryonic development, are ideal to interrogate the functions of TRIP13^{PCH-2} and p31(comet)$^{CMT-1}$ in promoting spindle checkpoint activation. An obvious next question raised by our studies is whether TRIP13 is also required for Mad2 recruitment in mammalian cells. The co-localization of TRIP13 and

Mad2 at kinetochores in the presence of spindle poisons suggests this function is likely to be conserved (TIPTON *et al.* 2012).

Despite the lack of a complete mitotic arrest when the checkpoint is activated in *C. elegans* embryos, Mad2 protein levels still appear to have repercussions on the robustness of the delay induced by *zyg-1* RNAi. Overexpression of Mad2 bypasses the requirement for Bub3 and Mad1 in the checkpoint (ESSEX *et al.* 2009) and a reduction in Mad2 protein levels, as observed in *cmt-1* and *cmt-1;pch-2* double mutants (Figures 4--9B&C; Figure 4-8A), correlates with the inability of a fraction of embryos to activate the checkpoint (Figure 4-9A). However, checkpoint robustness in *cmt-1* and *cmt-1;pch-2* double mutants appears compromised even when MAD-2 is overexpressed (Figure 4-10A), suggesting that either overexpression of GFP::MAD-2 cannot restore functional MAD-2 protein levels or there is an additional layer of complexity in checkpoint regulation, perhaps through modulation of the C-MAD-2/O-MAD-2 equilibrium (YE *et al.* 2015).

The precise role of TRIP13^{PCH-2} in meiosis has been enigmatic and a definitive meiotic substrate for this AAA+-ATPase has been difficult to identify. Biochemical analysis of TRIP13^{PCH-2} in mitotic exit (EYTAN *et al.* 2014b; YE *et al.* 2015) combined with our investigation of TRIP13^{PCH-2} function in checkpoint activation clearly indicates a role for this protein in regulating proteins with HORMA domains. It seems likely that TRIP13^{PCH-2}'s effects on pairing, synapsis and recombination also rely on its ability to regulate meiotic HORMA domain containing proteins, which localize to meiotic chromosomes and are required for pairing, synapsis and recombination (ZETKA *et al.* 1999; COUTEAU *et al.* 2004; NABESHIMA *et al.* 2004; COUTEAU AND ZETKA 2005; MARTINEZ-PEREZ AND VILLENEUVE 2005; GOODYER *et al.* 2008). Indeed, recent experiments in *C. elegans* have revealed a similar requirement for these proteins in regulating the progression of meiotic events (KIM *et al.* 2014; SILVA *et al.* 2014). Whether these HORMA domain proteins undergo conformational changes similar to Mad2, whether TRIP13^{PCH-2} regulates these changes, either directly or through an adapter

protein, and how the events of meiotic prophase are impacted by these changes are open and intriguing questions.

Our data contributes to several recent studies that demonstrate a close relationship between TRIP13^{PCH-2} and p31(comet)$^{CMT-1}$, either during the activation or the silencing of the spindle checkpoint (TIPTON *et al.* 2012; EYTAN *et al.* 2014b; WANG *et al.* 2014b; YE *et al.* 2015). This relationship could potentially explain why some organisms don't rely on TRIP13^{PCH-2} and/or p31(comet)$^{CMT-1}$ for spindle checkpoint function. For example, although TRIP13^{Pch2} is present in budding yeast, its expression is limited to meiosis (SAN-SEGUNDO AND ROEDER 1999). Fission yeast does not have a TRIP13 ortholog (WU AND BURGESS 2006). Both of these model systems also lack p31(comet) (VLEUGEL *et al.* 2012). This suggests that mitotic expression of TRIP13^{PCH-2} may be limited to organisms expressing p31(comet)$^{CMT-1}$. Given that TRIP13^{PCH-2} also functions in meiotic prophase (WU AND BURGESS 2006; JOSHI *et al.* 2009; WOJTASZ *et al.* 2009; ZANDERS AND ALANI 2009; ROIG *et al.* 2010; ZANDERS *et al.* 2011; CHEN *et al.* 2014; DESHONG *et al.* 2014; JOSHI *et al.* 2015), it's possible that p31(comet)$^{CMT-1}$ acts as an adaptor protein for TRIP13^{PCH-2} during chromosome segregation in order to specifically allow for regulation of Mad2 and its spindle checkpoint function. Future experiments aim to test this hypothesis, to understand whether the ATPase function of TRIP13^{PCH-2} contributes to checkpoint activation, and to distinguish between our two models for the role of TRIP13^{PCH-2} in checkpoint activation.

Materials & Methods

C. elegans Strains and Husbandry

The wildtype *C. elegans* strain background was Bristol N2 (BRENNER 1974) . All strains were maintained at 20°C except for those containing the *zyg-1(b1)* allele (O'CONNELL *et al.* 2001), which were maintained at 15°C. See Supplemental Table 1 for a list of all *C. elegans* strains used in this study. The strain BHL664, expressing a c-terminal GFP-3XFLAG fusion with PCH-2, was generated by cloning the 3kb genomic region surrounding the *pch-2* stop codon with *gfp-3xflag* in frame into pUC19 using Gibson cloning (GIBSON *et al.* 2009). This

plasmid was used as a repair template with the CRISPR/Cas9 system (DICKINSON *et al.* 2013; PAIX *et al.* 2014) with the guide RNA AATTGCATGAATCTCTTTCTCGAGG to tag the endogenous protein. The insertion was verified by PCR and live microscopy, and then backcrossed six times to N2 prior to analysis.

Microscopy & Mitotic Timing Experiments

All immunofluorescence and live microscopy was performed on a DeltaVision Personal DV deconvolution microscope (Applied Precision) equipped with a 100X N.A. 1.40 oil-immersion objective (Olympus) coupled with a CoolSNAP charge-coupled camera (Roper Scientific). Environmental temperature averaged 21°C during image collection for all experiments. For mitotic timing experiments, Z-sections were acquired with 8x 2µm steps using a 100X objective (Olympus) at 20s intervals. Exposure time was 100ms for mCherry::H2B and 50ms for GFP::PH. Mitotic duration was calculated for the AB cell in the presence of monopolar spindles as the interval between NEBD to the onset of cortical contractility (OCC) or the interval between NEBD and chromosome decondensation (DCON). NEBD was defined by the equilibration of mCh::H2B from the nucleus into the cytosol. OCC was defined as the change in conformation of the plasma membrane from circular to rectangular, or with *zyg-1* RNAi as the first frame when a persistent membrane bleb formed from the cortex of the embryo. DCON was defined as the loss of punctate mCh::H2B signal within the decondensing chromatin. To minimize bleaching and maximize signal intensity of GFP-tagged SAC and kinetochore components (PCH-2, MAD-2, MAD-1, BUB-1, BUB-3, and KNL-1), imaging was started just after NEBD as visualized by mCh::H2B. Here, 8x 1µm steps were captured with 250ms GFP and 100ms mCherry exposures at 20s intervals. All images of MAD-1, MAD-2, BUB-1, BUB-3, and PCH-2 are shown at pseudo-metaphase.

Immunofluorescence of gonads was performed as described previously (BHALLA AND DERNBURG 2005) . For experiments with *zyg-1(b1)*, L4s were picked and incubated at 25°C for 24-26 hours prior to dissection. For live microscopy of two cell embryos, eggs were dissected 18-26 hours post-L4 into 1X Egg Buffer (25mM Hepes pH7.4, 118uM NaCl, 48mM

KCl, 2mM EDTA, 0.5mM EGTA) and mounted on 2% agarose pads for immediate analysis. The following primary antibodies were used for *C. elegans* immunofluorescence (dilutions in parentheses): guinea pig anti-SUN-1 phospho-serine 8 (1:700) (WOGLAR *et al.* 2013a) and mouse anti-Histone H3 phospho-serine 10 (1:500) [Sigma]. Secondary antibodies were Cy3 anti-guinea pig (Jackson Immunochemicals) and Alexa-Fluor 488 anti-mouse (Invitrogen). Three-dimensional image stacks were collected at 0.2-μm Z-spacing and processed by constrained, iterative deconvolution. Image scaling and analysis were performed using functions in the softWoRx software package. Projections were calculated by a maximum intensity algorithm. Composite images were assembled and some false coloring was performed with Adobe Photoshop.

Quantification of GFP::MAD-1, GFP::MAD-2, and PCH-2::GFP-3XFLAG

Analysis was performed in Fiji. Quantification of unattached kinetochore signal was performed essentially as described for GFP::MAD-1 quantification in Moyle, et al 2014 (MOYLE *et al.* 2014) . Maximum intensity projections of both mCh::H2B and GFP fusion proteins were made after the pseudo-metaphase plate was generated. The image was rotated so the metaphase plate was vertical, channels were split, and the maximum GFP pixel was identified using the process function within a box on the unattached side of the metaphase plate. In the same x-plane, the maximum mCh::H2B pixel was found. The width was changed to 12 pixels and the maxmimum GFP signal intensity was recorded in this 12 pixel window centered at the mCherry maxima. The background GFP signal was calculated by taking the average GFP intensity of a 4 pixel box in the same x-plane, 8 pixels away from the maximum mCherry on the opposite side of the pseudo-metaphase plate to the maximum GFP (i.e. the attached side). This background GFP was then subtracted from the maximum to measure the kinetochore bound GFP fusion intensity. This process was repeated at least 7x for each genetic background and the signal was averaged. The average signal in a

wildtype genetic background was set as 100% and relative signals were calculated for other genetic backgrounds as compared to wildtype.

Feeding RNA interference

RNAi was performed by growing relevant worm strains on HT115 bacteria transformed with vectors allowing for IPTG inducible expression of the desired dsRNA. Bacterial strains containing RNAi vectors were cultured overnight at 37°C, centrifuged, and the pellet was re-suspended in 1/10 of the original volume. 50uL of concentrated culture was spotted onto an NGM plate with 1mM IPTG and 50ug/uL of kanamycin or carbenicillin and the RNAi spot was allowed to grow overnight at 37C.

To knockdown *zyg-1* by feeding RNAi, we used Gateway cloning (Invitrogen) to insert the first 1.5kb of *zyg-1* genomic DNA into pDONRT7 (COUTEAU AND ZETKA 2011) using zyg-1_FWD (ggggacaagtttgtacaaaaaagcaggctctATGAGCGGTGGGAAGAGTGG) and zyg-1_REV (ggggaccactttgtacaagaaagctgggtcGAAGTATAAACAAAAGGATTGTTCGTC). L4 hermaphrodite worms were picked into M9, transferred to RNAi plates, allowed to incubate for 2-3 hours and then transferred to fresh RNAi plates. Live microscopy was performed on embryos 22-26 hours after worms were picked to *the zyg*-1 RNAi plate. HT115 bacteria transformed with pHSG298 (Clontech) was used as a control for *zyg-1*^{RNAi}.

To knockdown *mad-2*, feeding RNAi clones from the Ahringer library (FRASER *et al.* 2000) were used: *mad-2*^{RNAi} (sjj_Y69A2A_2326.a) and control^{RNAi} (L4440).

For double RNAi of *mad-2* and *zyg-1*, L4s were picked to *mad-2*^{RNAi} or control (L4440) plates and allowed to grow for at 20°C. After 4 days, F1 progeny were picked as L4s onto *zyg-1*^{RNAI} or control (pHSG298) plates, incubated for 22-26 hours at 20°C and then dissected for analysis.

Worm Lysis & Immunoblotting

To make worm lysates, worms of each genotype were grown on 10 NGM plates spread with OP50 bacteria at 20°C. Worms were washed from plates (M9+ 0.1% TX-100) and resuspended in 500uL Buffer H (50mM HEPES pH8.0, 2mM $MgCl_2$, 0.1mM EDTA pH8.0,

0.5mM EGTA-KOH pH8.0, 15% Glycerol, 0.1% NP-40, 500mM KCl) (AKIYOSHI *et al.* 2009a) supplemented with protease inhibitors (complete mini tablets w/o EGTA (Roche), 0.1 mM AEBSF, 5 mM benzamidine, 10ug/mL aprotinin). Worms were bead beat (BioSpec) 3x30" with 30" rest at 4C and then sonicated 2x30" (Braun). Lysates were spun for 10' at 14k and protein concentration was measured in the supernatant with a Bradford Assay (Bio-Rad). 250uL of 4X Sample Buffer was added. Equivalent amounts of protein were run for each sample for analysis by immunoblot.

For immunoblotting, samples were run on 12% SDS-PAGE gels, transferred to nitrocellulose using a Trans-Blot SD Semi-Dry system (Bio-Rad), blocked in a PBST + 5% (w/v) non-fat milk solution, and then probed with either mouse anti-GFP (1:1000; Roche), mouse anti-FLAG M2 (1:2500; Sigma), rabbit anti-MAD-2 (1:10000, gift from A. Desai), or mouse anti-alpha-tubulin (1:3500; DM1A; Sigma) overnight at 4°C. Blots were washed 3x for 10 minutes in PBST, probed for 1 hour using an HRP-conjugated secondary antibody (rabbit or mouse; GE Healthcare), washed 3x for 10 minutes in PBST, and then analyzed using a chemiluminescent substrate (Thermo Scientific).

For quantification of MAD-2 protein levels, the analyze gel function was used in ImageJ. For each genotype, 2 western blots from 3 independent lysate preparations (6 total immunoblots) were analyzed and the signal between them was averaged. MAD-2 protein level in a wildtype genetic background was normalized to 100%.

Yeast Two-Hybrid Assays

Yeast two-hybrid assays were performed according to the manufacturer's protocols (Matchmaker Gold System, Clontech). Control refers to growth on SC –leu/-trp, whereas selection refers to growth on SC –leu/-trp/-his/-ade (high stringency). cDNA for *pch-2* was cloned into pGBKT7 (bait vector) and cDNA for *cmt-1* were cloned into both pGBKT7 and PGADT7 (prey vector). All other kinetochore and SAC genes in Y2H vectors were a kind gift from A. Desai.

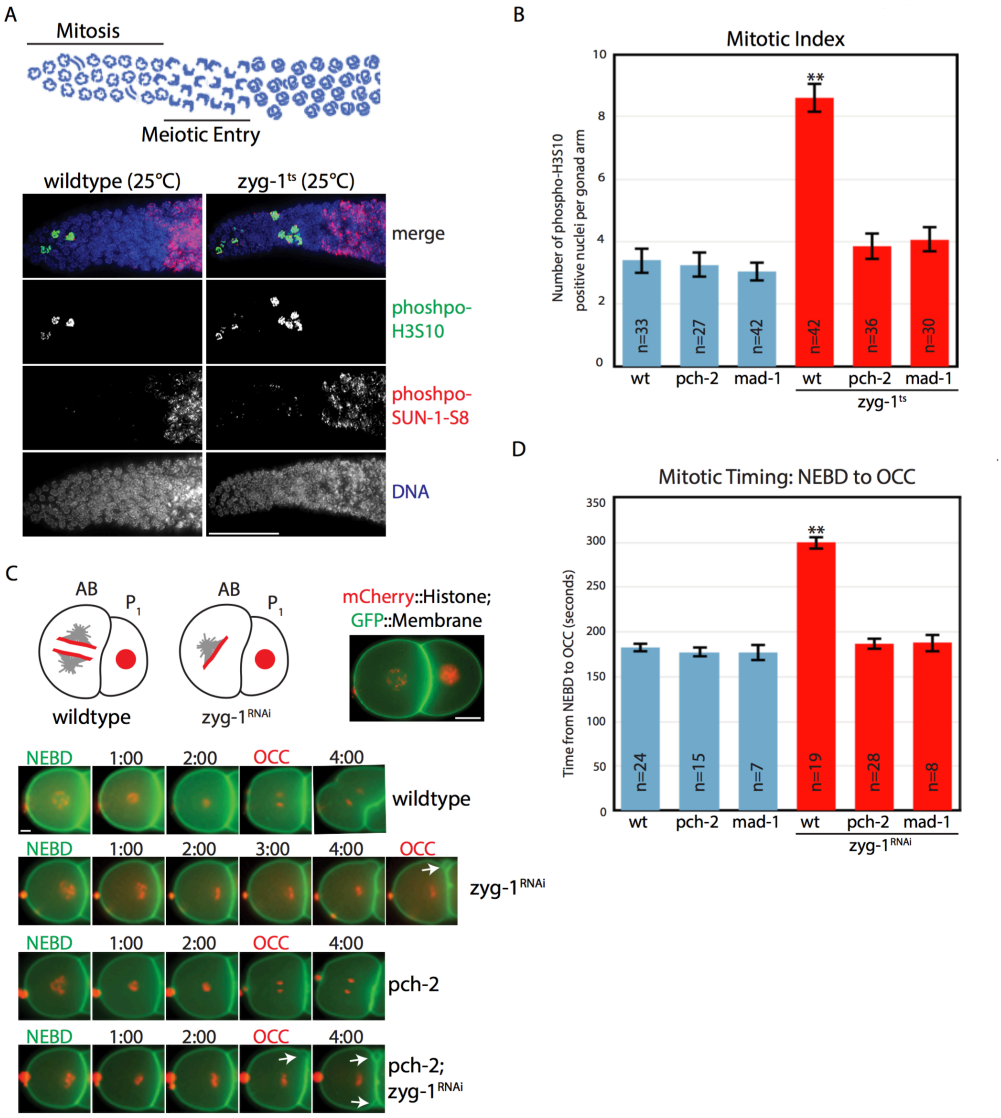

Figure 4- 1: PCH-2 is required for the spindle checkpoint response in C. elegans

(A, top) Schematic of the distal section of the *C. elegans* germline. Actively dividing mitotic nuclei are recognized by an anti-phospho-HistoneH3-S10 antibody and are found in distal tip of the germline. Upon meiotic entry, chromosomes become polarized and SUN-1 present in the nuclear envelope is recognized by an anti-phospho-SUN-1-S8 antibody. (A, bottom) Activation of the spindle checkpoint by shifting *zyg-1*^{ts} worms to the non-permissive temperature increases the mitotic index (number of phosph-H3S10-positive nuclei). Representative images of control and *zyg-1*^{ts} germlines stained with antibodies recognizing phospho-H3S10 and phospho-SUN-1-S8 as well as with DAPI. Scale bar represents 20µm (B) Mutation of *pch-2* does not affect the mitotic index of germline mitotic nuclei unless *zyg-1* is inactivated (*zyg-1*^{ts}). (C, top) Schematic of the two-cell *C. elegans* embryo. Note that RNAi of *zyg-1* creates monopolar spindles which delay mitosis through activation of the spindle checkpoint. mCherry::Histone H2B and GFP::Membrane were used to define nuclear envelope breakdown (NEBD) and the onset of cortical contractility (OCC), respectively. All

further analyses were performed in the AB cell. Scale bar represents 10µm. (C, bottom) Selected frames from wildtype, *pch-2*, *zyg-1*^{RNAi} and *pch-2;zyg-1*^{RNAi} movies are shown, denoting NEBD and OCC. OCC in *zyg-1*^{RNAi} embryos is defined by the presence of a persistent membrane bleb between AB and P_1 (arrows). Scale bar represents 5 µm. (D) Mutation of *pch-2* has no affect on mitotic timing during an unperturbed mitosis but reduces mitotic timing to wildtype timing when *zyg-1* is knocked down by RNAi (*zyg-1*^{RNAi}). Error bars in all graphs represent SEM. A ** indicates a genotype that is significantly different than all other genotypes shown (p-value < 0.0001). Significance was assessed using a paired *t*-test.

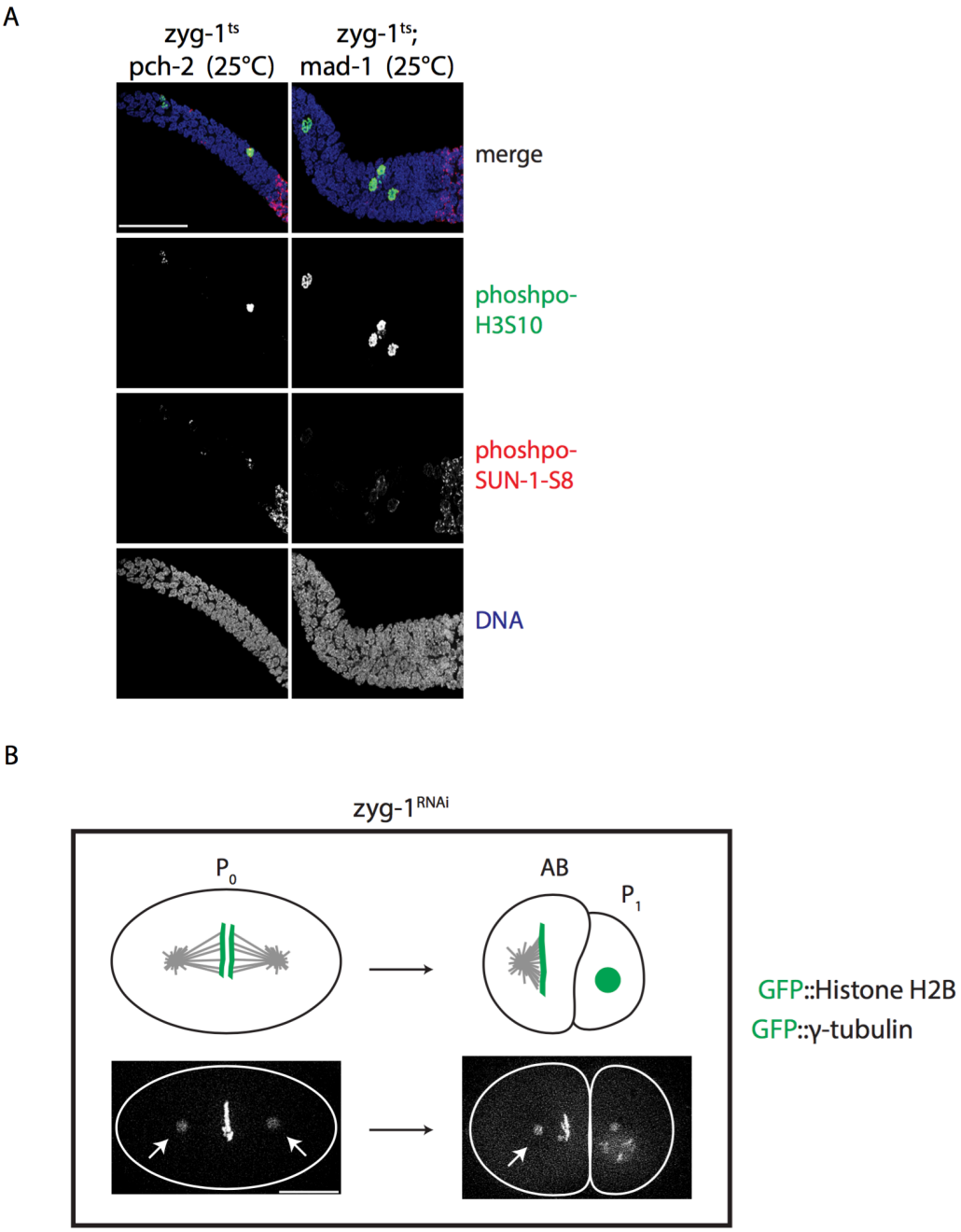

Figure 4- 2: Mutation of pch-2 or mad-1 reduces the mitotic index of zyg-1^{ts} germlines.

(A) Representative images of *zyg-1^{ts}pch-2* and *zyg-1^{ts};mad-1* mutant germlines stained with DAPI and antibodies recognizing phospho-H3S10 and phospho-SUN-1-S8. Scale bar represents 20μm. (B, top) Schematic of the first embryonic divisions in *C. elegans* after 24 hours of feeding with bacteria expressing *zyg-1* dsRNA. The first division (P_0) proceeds normally with a bipolar spindle, but subsequent divisions take place with monopolar spindles. (B, bottom) Selected frames from the first 2 divisions (P_0 and AB) of embryos at metaphase

expressing both GFP::Histone H2B and GFP::γ-tubulin. Arrows denote spindle poles. The white lines surrounding cells were drawn in Adobe Illustrator. Scale bar represents 10μm.

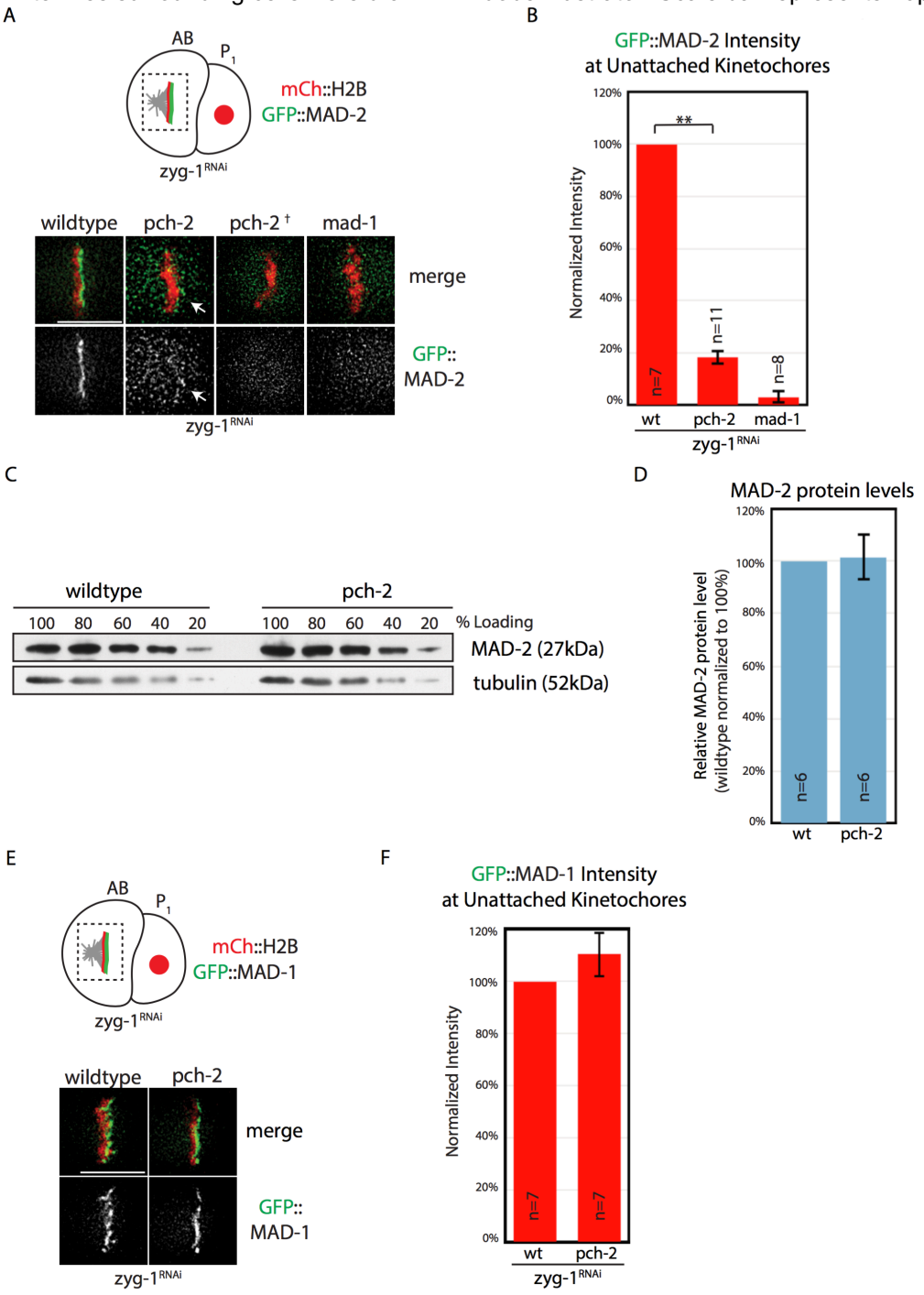

Figure 4- 3: PCH-2 is required for robust GFP::MAD-2 localization to unattached kinetochores

(A, top) Schematic showing the localization of GFP::MAD-2 to unattached kinetochores after checkpoint activation. Unattached kinetochores are present on the side of the pseudo-metaphase plate lacking a centrosome. Dashed box indicates area shown in images (A, bottom) GFP::MAD-2 signal after *zyg-1* RNAi seen in control worms is either nearly absent (*pch-2*) or completely absent (*pch-2*†) in *pch-2* mutants. Arrows indicate residual GFP::MAD-2 localization. (B) Quantification of kinetochore bound GFP::MAD-2 shows that signal was reduced by an average of 82% in *pch-2* mutants and an average of 97% in *mad-1* mutants. Quantification was performed on at least 7 embryos for each genotype. (C) MAD-2 protein levels are unaffected in *pch-2* mutants. Whole worm lysates were first normalized for protein concentration and then serial dilutions were analyzed via immunoblot with an anti-MAD-2 antibody and an anti-alpha-tubulin antibody serving as a loading control. (D) Quantification of MAD-2 protein level in *pch-2* mutants across multiple immunoblots indicates that MAD-2 protein level is 102% of wildtype. (E) GFP::MAD-1 properly localizes to unattached kinetochores in *pch-2* mutants (F) Quantification of GFP::MAD-1 at unattached kinetochores in wildtype and *pch-2* mutants. Quantification was performed on 7 embryos for each genotype. Error bars in all graphs represent SEM. A ** indicates a p-value < 0.0001. Significance was assessed using a paired *t*-test. All scale bars represent 5μm.

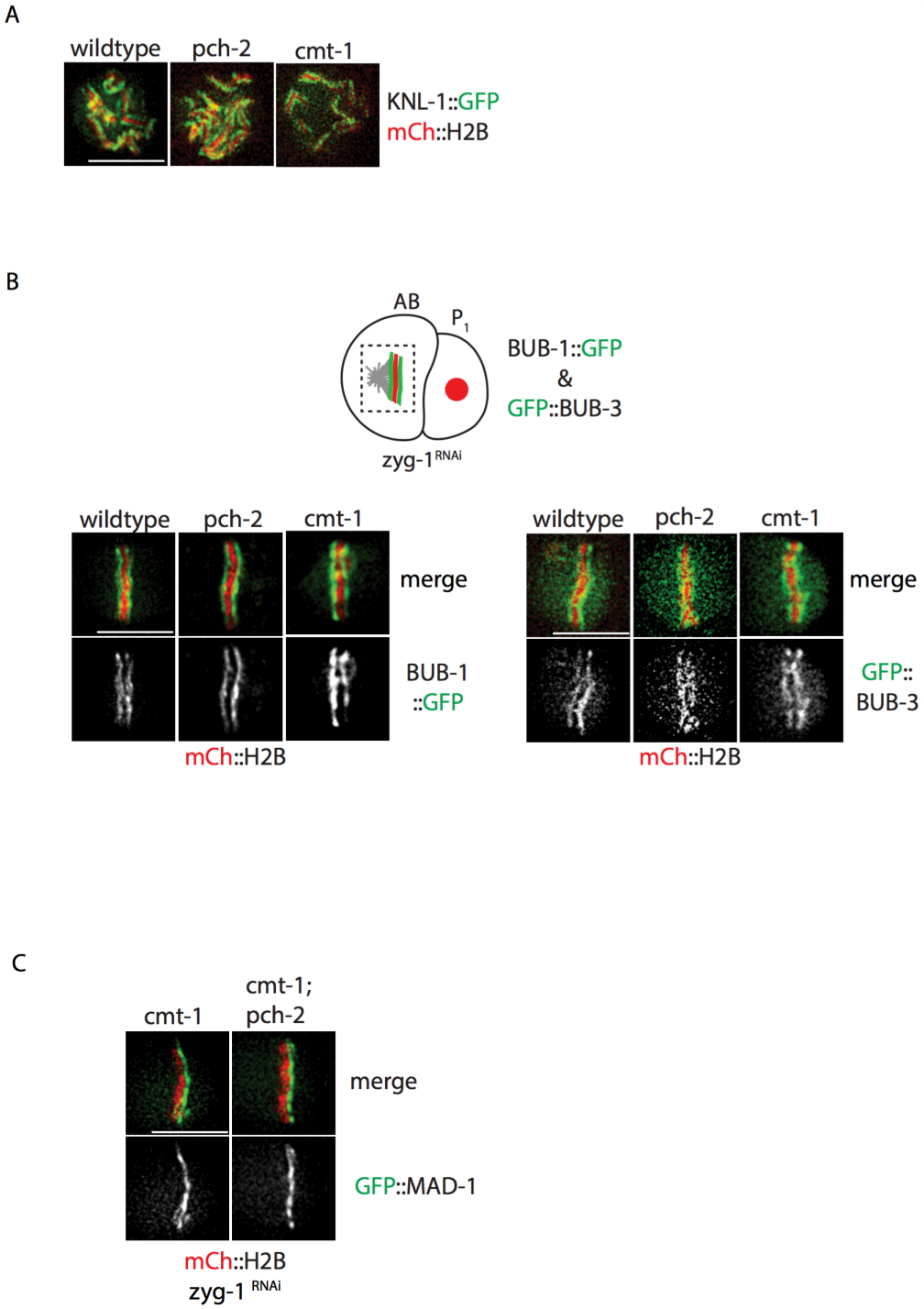

Figure 4- 4: Mutation of pch-2 or cmt-1 has no effect on the localization of KNL-1, BUB-1, BUB-3 and MAD-1 to kinetochores.

(A) No defects in KNL-1::GFP kinetochore signal intensity or loading were apparent in *pch-2* or *cmt-1* mutants. Images of pro-metaphase kinetochores are shown. (B, top) Schematic shows the localization of BUB-1::GFP and GFP::BUB-3 to kinetochores at metaphase after

zyg-1 RNAi. Note that both proteins localize to both sides of pseudo-metaphase plate, indicating their localization is not limited to unattached kinetochores. (B, bottom) BUB-1::GFP and GFP::BUB-3 properly localize to kinetochores in *pch-2* and *cmt-1* mutants. (C) GFP::MAD-1 properly localizes to unattached kinetochores after *zyg-1* RNAi in both *cmt-1* and *cmt-1;pch-2* mutants. All scale bars represent 5 μm.

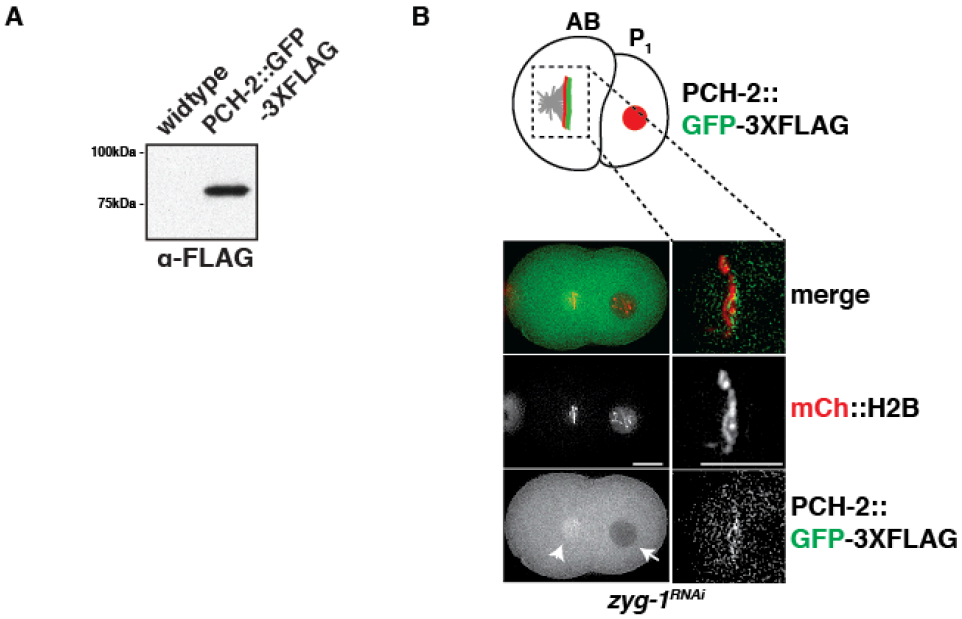

Figure 4- 5: PCH-2::GFP-3XFLAG localizes to unattached kinetochores during spindle checkpoint activation

(A) An immunoblot of PCH-2::GFP-3XFLAG worms shows that the full length tagged protein is expressed. (B, left panels) PCH-2:::GFP-3XFLAG is expressed in the mitotic embryo. The arrowhead (left) indicates enrichment of PCH-2::GFP-3XFLAG after NEBD in the AB cell, whereas the single arrow (right) indicates PCH-2::GFP-3XFLAG exclusion from the nucleoplasm prior to mitotic entry in the P_1 cell. Scale bar represents 10μm. (B, right panels) Checkpoint activation via RNAi of *zyg-1* localizes PCH-2::GFP-3XFLAG to unattached kinetochores. Scale bar represents 5μm.

A

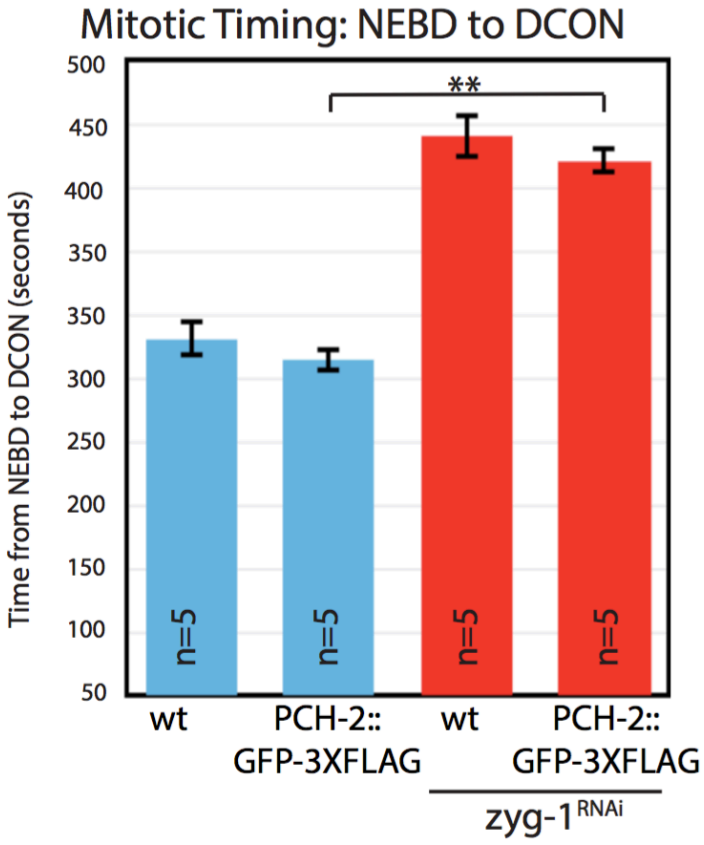

Figure 4- 6: PCH-2::GFP-3XFLAG embryos are competent for spindle checkpoint activation

(A). RNAi of zyg-1 in PCH-2::GFP-3XFLAG induces a statistically significant delay in mitotic timing as in wildtype embryos. Chromosome decondensation (DCON) was used as a marker of mitotic exit. Error bars represent SEM. A ** indicates a p-value < 0.0001. Significance was assessed using a paired t-test

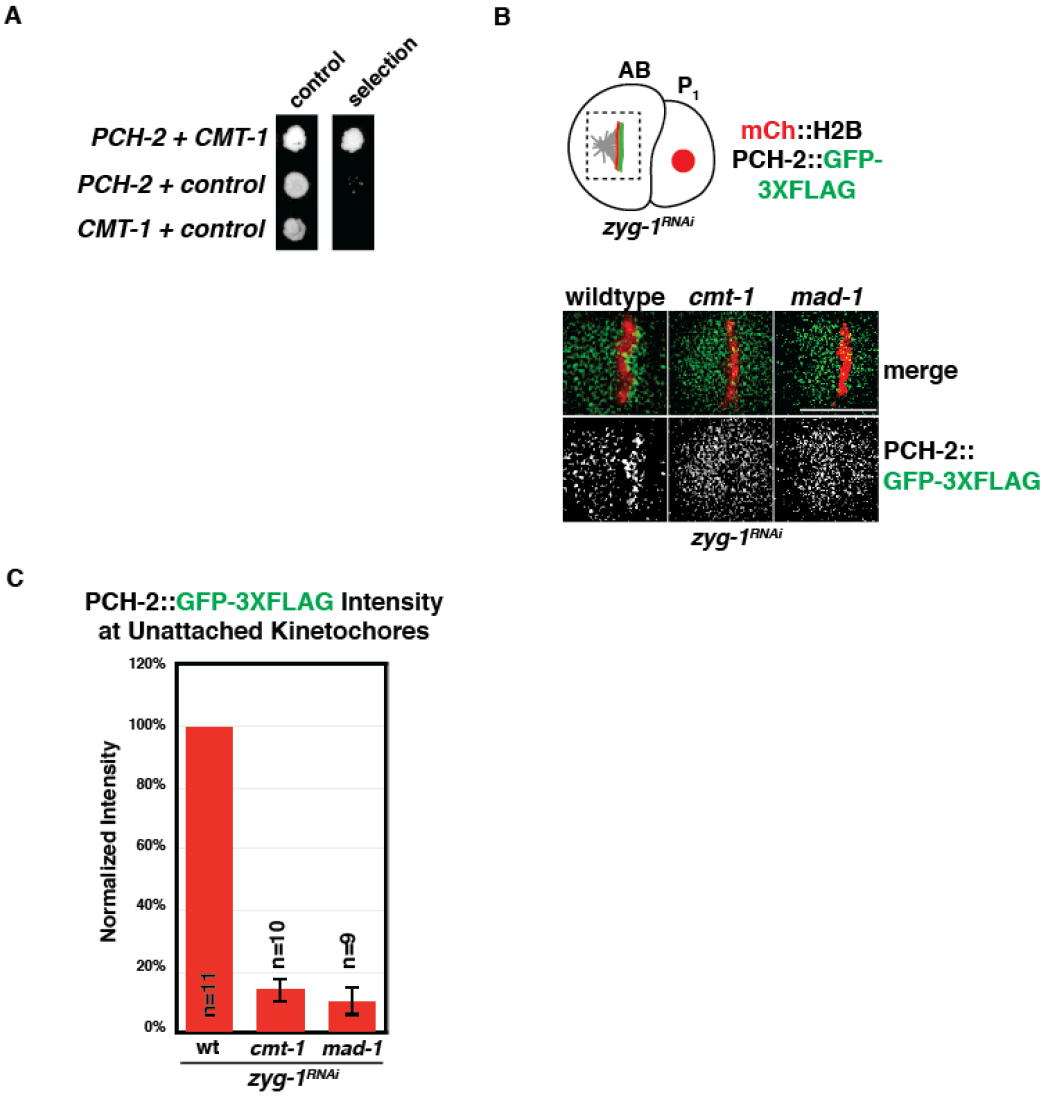

Figure 4- 7: CMT-1 and MAD-2 are required for PCH-2 localization to unattached kinetochores during checkpoint activation

(A) PCH-2 interacts with CMT-1 by yeast two-hybrid assay. PCH-2 is fused to GAL4 DNA binding domain (bait protein) and CMT-1 is fused to the GAL4 activation domain (prey protein). Control denotes growth on SC –leu –trp; Selection indicates growth on SC –leu –trp –his –ade. Histidine and adenine expression are driven by the GAL4 promoter. Empty prey or bait vectors were used as controls in lanes 2 and 3, respectively. (B) PCH-2::GFP-3XFLAG fails to localize to unattached kinetochores in cmt-1 and mad-1 mutant embryos when zyg-1 is knocked down by RNAi. Scale bar represents 5μm. (C) Quantification of PCH-2::GFP-3XFLAG at unattached kinetochores indicates that mutation of cmt-1 and mad-2 reduce signal to 14% and 10% of wildtype, respectively. Quantification was performed on 9 embryos for each genotype. Error bars in all graphs represent SEM.

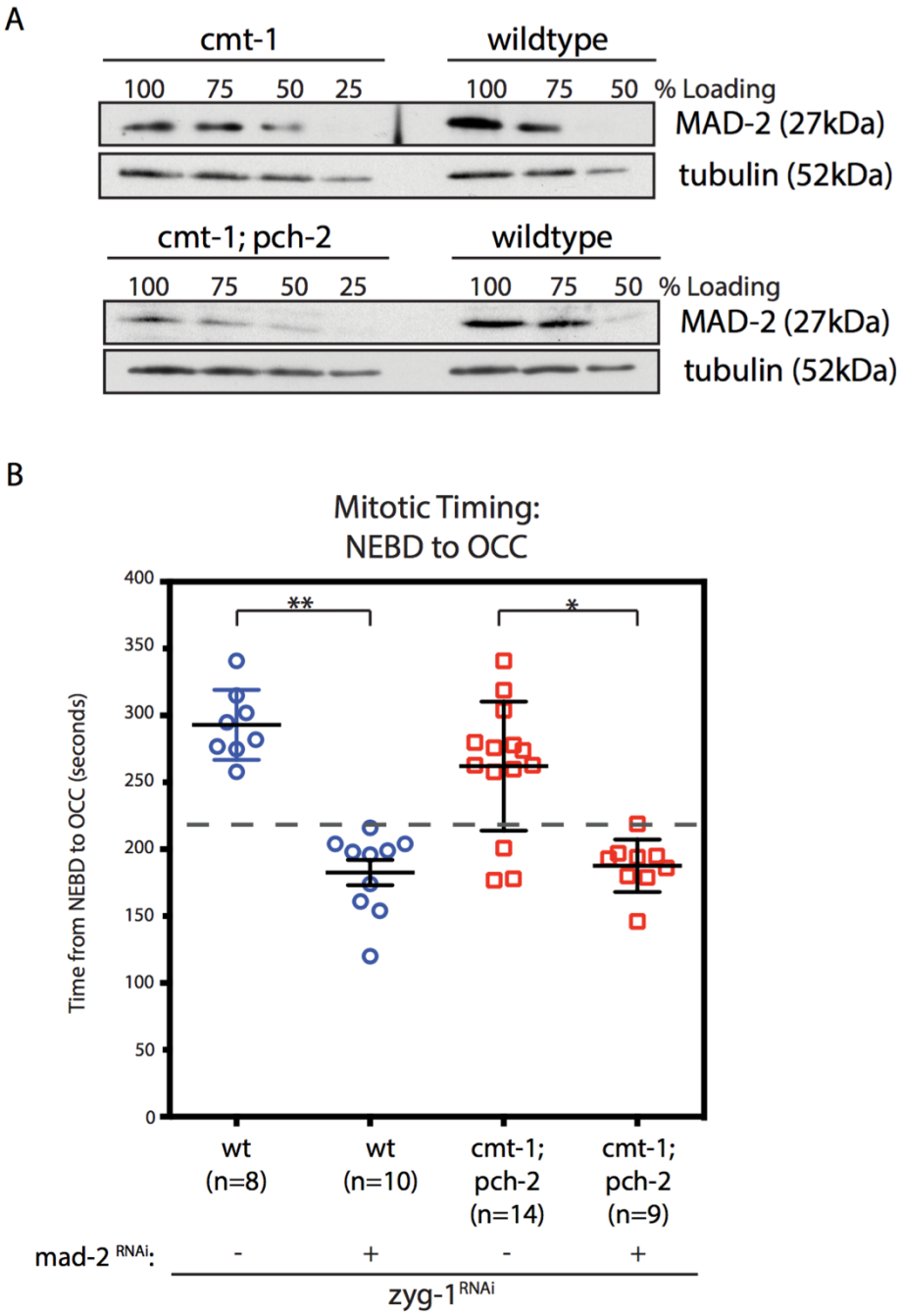

Figure 4- 8: The mitotic delay produced by zyg-1 RNAi in cmt-1;pch-2 mutants is spindle checkpoint dependent.

(A) MAD-2 protein levels are reduced in *cmt-1* and *cmt-1;pch-2* mutants. Whole worm lysates were first normalized for protein concentration and then serial dilutions were analyzed via immunoblot with an anti-MAD-2 antibody and an anti-alpha-tubulin antibody serving as a loading control. (B) RNAi of *mad-2* restores wildtype mitotic timing in both *zyg-1*^{RNAi} and *cmt-*

1;pch-2;zyg-1^{RNAi} embryos. Error bars represent SEM. A ** indicates a p-value < 0.0001. * indicates a p-value < 0.01. Significance was assessed using a paired *t*-test.

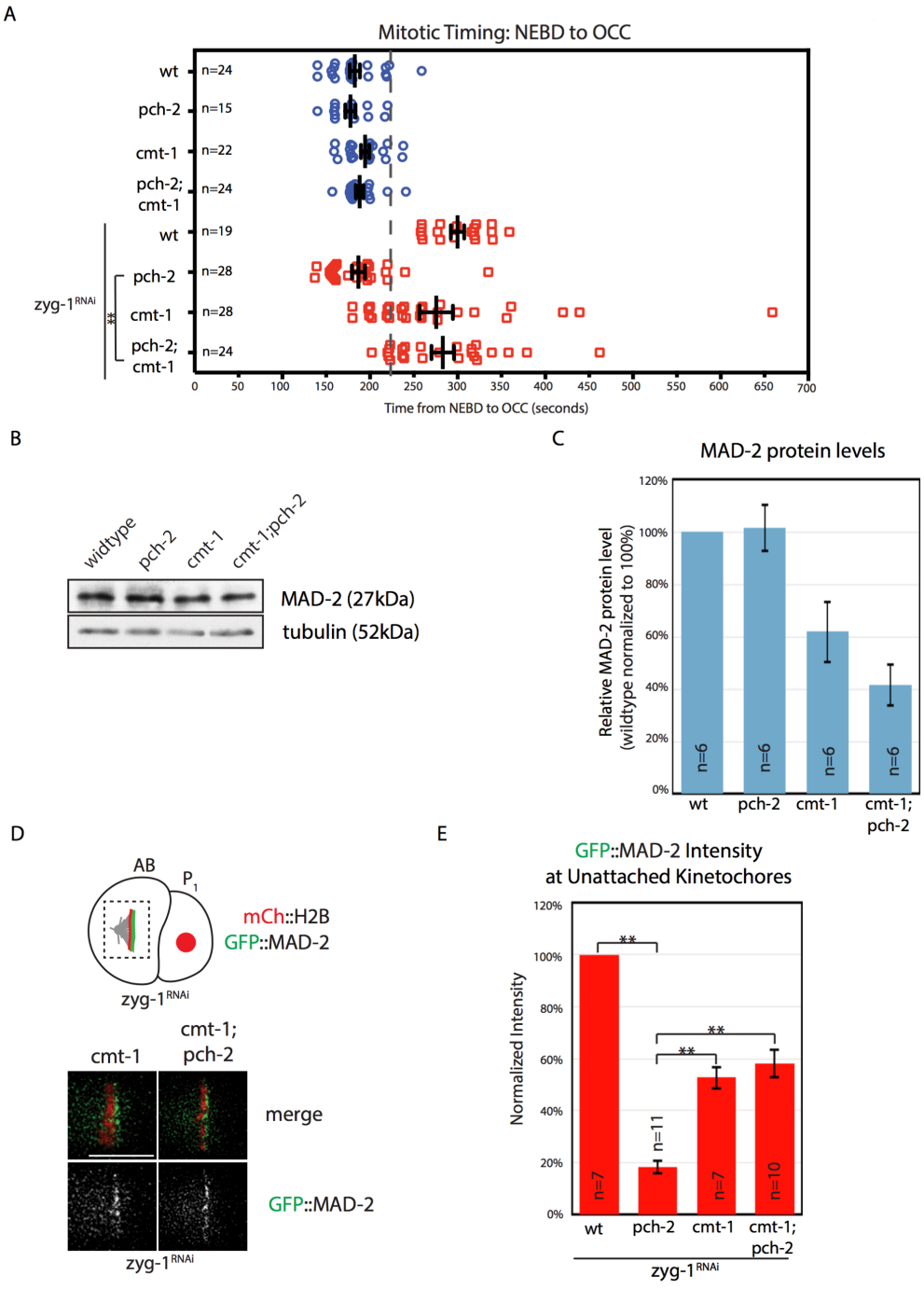

Figure 4- 9: Mutation of cmt-1 suppresses the checkpoint defect of pch-2 mutants.

(A) Mutation of *cmt-1* restores checkpoint function in *pch-2* mutants. A dashed gray line was drawn at 222 seconds representing the upper limit of wildtype mitotic timing. 95% of wildtype embryos and 0% of *zyg-1*^{RNAi} embryos displayed mitotic timing at or below this line. Black lines indicate the mean mitotic timing for each genotype, the whiskers indicate SEM. (B). MAD-2 protein levels are reduced in *cmt-1* and *cmt-1;pch-2* mutants. Whole worm lysates were first normalized for protein concentration and then serial dilutions were analyzed via immunoblot with an anti-MAD-2 antibody and an anti-alpha-tubulin antibody serving as a loading control. (C) *cmt-1* and *cmt-1;pch-2* double mutants show significant reductions in MAD-2 protein levels to 58% and 42%, respectively, after quantification. Quantification was performed on 3 unique lysates preparations each run in duplicate. (D) *cmt-1* and *cmt-1;pch-2* mutants show GFP::MAD-2 localization to unattached kinetochores. Scale bar represents 5μm. (E) Quantification of GFP::MAD-2 signal at unattached kinetochores shows that mutation of *cmt-1* partially restores GFP::MAD-2 localization in *pch-2* mutants. Quantification was performed on at least 7 embryos for each genotype. Error bars represent SEM. A ** indicates a p-value < 0.0001. Significance was assessed using a paired *t*-test.

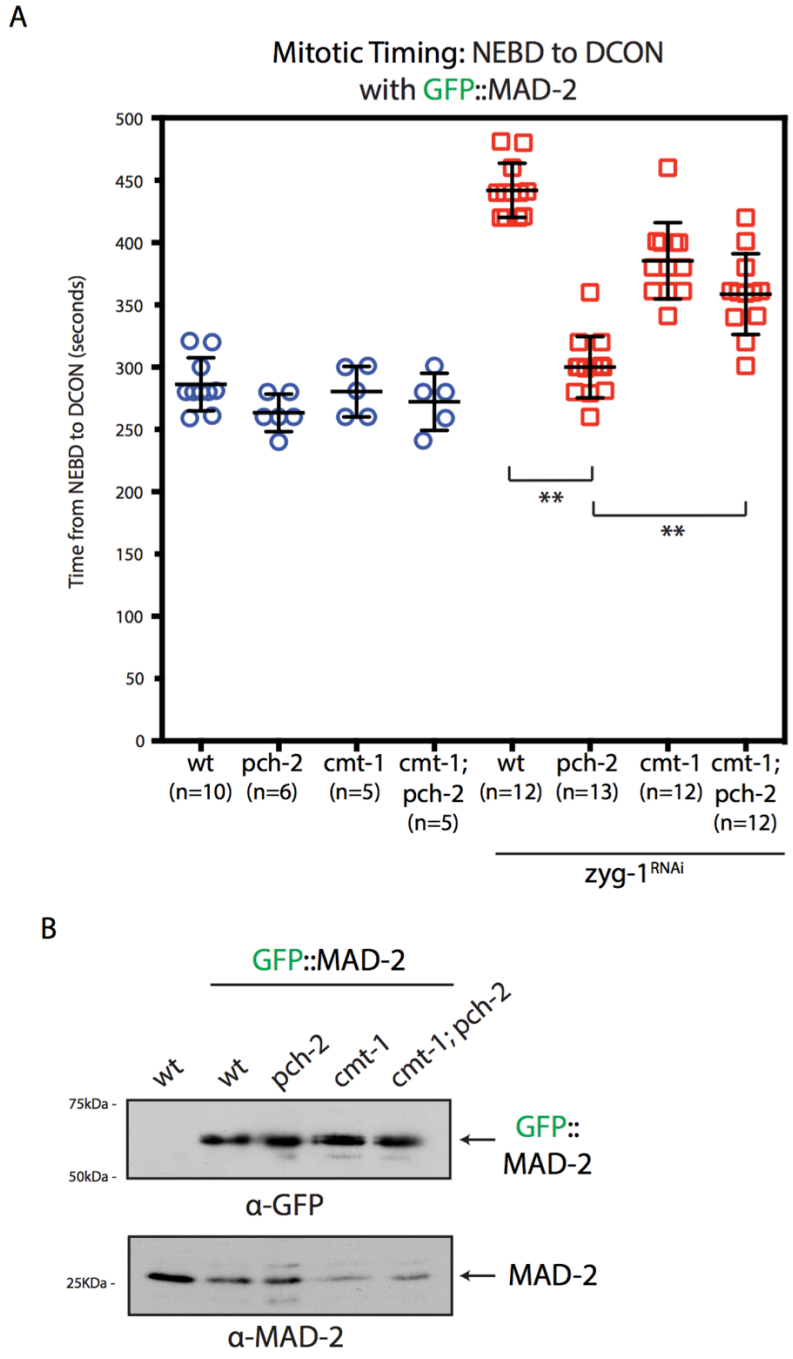

Figure 4- 10: Overexpression of GFP::MAD-2 does not rescue checkpoint function in pch-2 or cmt-1 mutants

(A) *pch-2;zyg-1*^{RNAi} mutants exhibit wildtype mitotic timing and *cmt-1; zyg-1*^{RNAi} and *cmt-1;pch-2; zyg-1*^{RNAi} mutants have a less robust checkpoint response despite overexpressing GFP::MAD-2. (B) Immunoblot showing GFP::MAD-2 levels are unperturbed in *pch-2* and *cmt-1* mutants. The strains expressing GFP::MAD-2 also

express endogenous MAD-2 protein (lower immunoblot). Error bars represent SEM. A ** indicates a p-value < 0.0001. Significance was assessed using a paired *t*-test.

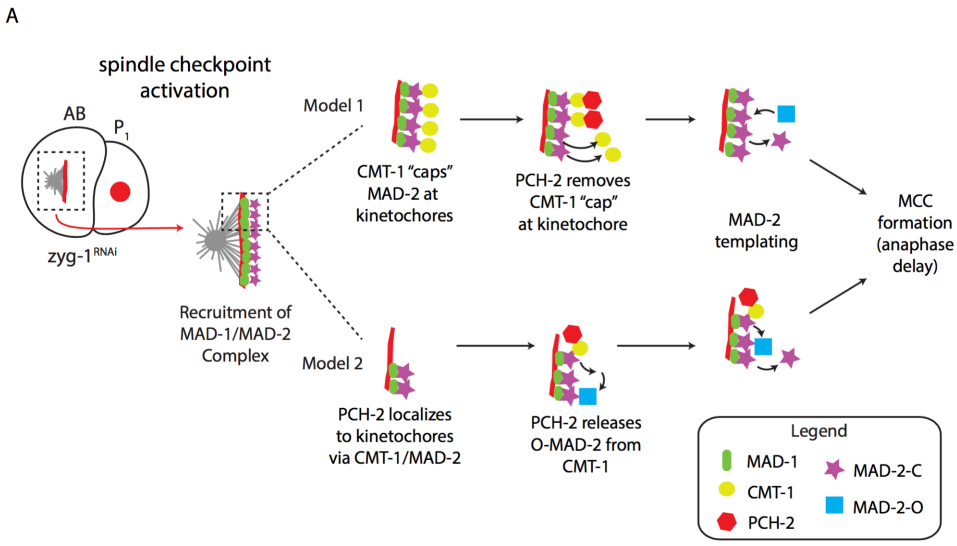

Figure 4- 11: Models for TRIP13^{PCH-2}'s role in spindle checkpoint activation.

(A) Two models for how TRIP13^{PCH-2} regulates spindle checkpoint activation discussed in the text are depicted. During checkpoint activation, the Mad1/C-Mad2 complex is recruited to unattached kinetochores. In model 1, TRIP13^{PCH-2} removes an inhibitory p31(comet)$^{CMT-1}$ "cap" from kinetochore bound Mad1/C-Mad2 in order to allow free O-Mad2 to dimerize with C-Mad2 at the kinetochore, converting it to C-Mad2, promoting MCC formation and preventing anaphase. In model 2, TRIP13^{PCH-2} localizes to kinetochores where it interacts with p31(comet)$^{CMT-1}$/C-Mad2, releasing O-Mad2 from p31(comet)$^{CMT-1}$. This allows for O-Mad2 to dimerize with Mad1/C-Mad2 at the kinetochore, promoting the generation of additional soluble C-Mad2, MCC production, and an anaphase delay.

Chapter 5: Analysis of the role of Trip13 in modulating spindle checkpoint robustness in human cells

Introduction

In mitosis, sister chromatids must bi-orient, such that they are attached to microtubules emanating from opposite spindle poles. The spindle checkpoint monitors chromosome attachment to the mitotic spindle and delays the onset of anaphase until all chromosomes are properly attached, allowing time for error correction. The spindle checkpoint prevents the production of daughter cells with incorrect chromosome number, termed aneuploidy, which are a hallmark of human solid tumors.

The spindle checkpoint functions through the recruitment of checkpoint components to kinetochores, the macromolecular machines that drive chromosome segregation (FOLEY AND KAPOOR 2013a). Mad2 is the most downstream component in the spindle checkpoint response at the kinetochore. The amount of Mad2 recruited to kinetochores correlates with the strength of the spindle checkpoint response (COLLIN *et al.* 2013) and modulating the amount of Mad2 alters the strength of the response. Furthermore, different MT poisons result in differing strengths of spindle checkpoint responses, again correlating with different amounts of Mad2 at kinetochores. Therefore, understanding the recruitment and regulation of Mad2 to kinetochores should determine the signals that regulate the strength or robustness of the spindle checkpoint.

Previously, we identified PCH-2^{TRIP13} as a novel component of the spindle checkpoint apparatus in *C. elegans*. Intriguingly, we found that PCH-2^{TRIP13}, in concert with its adaptor protein CMT-1^{p31comet} , was an important Mad2 recruitment factor at unattached kinetochores. While *pch-2* mutants showed a sever reduction (to 20% of WT) in Mad2 kinetochore recruitment, *cmt-1;pch-2* double mutants largely restored checkpoint function and Mad2 localization to unattached kinetochores. Thus, while *pch-2* mutants were checkpoint null in *C. elegans*, the CMT-1/PCH-2 module is not required *per se* for the spindle checkpoint. Thus, it

remains possible that the CMT-1/PCH-2 complex is merely an adaptation utilized by specific cell types to recruit additional Mad2 to kinetochores.

Here, we explore the function of TRIP13, the human ortholog of PCH-2, in the spindle checkpoint in two human cell types. Human RPE1 epithelial cells are the ideal cell line to study spindle checkpoint robustness, as they were previously utilized to demonstrate the dynamicity of the spindle checkpoint response. Utilizing this cell line, we can test whether TRIP13/p31(comet) complex is absolutely required for the spindle checkpoint in all cell types, or, instead, a complex that specific cell types utilize to promote checkpoint robustness.

Results

Trip13 knockdown in HeLa cells produces only mild spindle checkpoint defects

We first examined the function of TRIP13 in the spindle checkpoint in human cervical cancer, or HeLa cells. To knockdown Trip13 in HeLa cells, we utilized a shRNA (small hairpin RNA) targeting the 3'UTR (5'- CATTATACCAACTGAGAAA -3') previously showed robust knockdown, as well as a scrambled control shRNA (5' – GAAACACTACCTATAGAAT – 3'). In order to generate a stable cell line with robust Trip13 knockdown via shRNA, we used lentiviral infection with a copGFP reporter. Third generation lentiviral vectors and the shRNA plasmids were calcium chloride transfected into 293T cells. Lentivirus was harvested and used to infect HeLa cells. Both lentivirus infections were successful as HeLa cells successfully expressed the copGFP reporter (Figure 5-1A). However, the TRIP13 shRNA infection was lost with passaging of the cells, perhaps because HeLa cells rely upon TRIP13 to promote efficient mitotic exit. Therefore, we used FACs to sort the cells by GFP, enriching for Trip13 knockdown.

To assay for Trip13 knockdown, we performed an immunoblot on freshly sorted cells. Trip13 knockdown was robust, but not complete, perhaps due to its requirement in mitotic exit (Figure 5-1C). Importantly, Mad2 was not knocked down (Figure 5-1C) even though it's a common off-target hit for shRNA. Furthermore, Trip13 knockdown cells were

stained for Histone H3-S10 phosphorylation, which marks actively dividing cells. Trip13 knockdown induced a significant increase in mitotic index (H3-S10 positive; Figure 5-1D), consistent with previous characterization and further confirming Trip13 knockdown.

Next, we assayed the spindle checkpoint response in HeLa cells by localizing Mad1 and Mad2 to kinetochores after treatment with nocodazole, a spindle poison that depolymerizes microtubules. Mad1 showed robust co-localization with kinetochores, stained with CENP-A, in both control and *Trip13* knockdown cells as expected (Figure 5-1E). Mad2 kinetochore localization was disrupted in some *Trip13* shRNA cells, but not others (Figure 5-1F). We quantified the defect in Mad2 localization and determined that the majority of cells (>60%) showed robust Mad2 co-localization and only a very small percentage (~2%) showed loss of Mad2 from more than 20 kinetochores (Figure 5-1G). Therefore, knockdown of Trip13 in HeLa cells produces only minor defects in spindle checkpoint signaling in HeLa cells.

Trip13 is required for a robust spindle checkpoint response in human RPE1 cells

We previously showed that PCH-2, the TRIP13 ortholog in C. elegans, is essential for the spindle checkpoint in nematodes (NELSON *et al.* 2015). However, loss of Trip13 only resulted in a minor defect in Mad2 localization to unattached kinetochores in HeLa cells when the spindle checkpoint was activated. Therefore, we wondered if Trip13 might not be essential for the spindle checkpoint in human cells, but instead utilized as a checkpoint robustness factor by recruiting Mad2 to kinetochores. To test this hypothesis, we utilized the RPE1 human epithelial cell line, which has previously been utilized for checkpoint robustness assays (COLLIN *et al.* 2013).

First, we compared TRIP13 protein levels in HeLa and RPE1 cells via immunoblot (Figure 5-2A). We found TRIP13 to be dramatically overexpressed in the HeLa cell line compared to RPE1 cells. This is consistent with a 2016 analysis that found a human colon cancer cell line, HCT116, also dramatically overexpressed TRIP13 (MA AND POON 2016). Therefore, cancer cells may utilize TRIP13 as an oncogenic protein and further checkpoint analysis of TRIP13 should be performed in a non-transformed cell line.

We knocked down Trip13 and Mad2 in RPE1 cells using a lipofectamine based reagent and verified knockdown via immunoblot (Figure 5-2B). Next, we activated the spindle checkpoint using nocodazole in RPE1 cells expressing Venus-Mad2. Using live microscopy, we analyzed the localization of Venus-Mad2 to kinetochores in control, Trip13, and Mad2 siRNA treated cells. RPE1 cells are non-aneuploid and have 46 pairs of sister kinetochores. Whereas the majority of control cells localized Venus-Mad2 to >40 kinetochores, Trip13 knockdown dramatically reduced the number of kinetochores with Venus-Mad2 (Figure 5-3A). Knockdown of Mad2 produced an even stronger reduction in the number of Venus-Mad2 positive kinetochores than Trip13 siRNA (data not shown). Therefore, while loss of Trip13 results in reduced Mad2 kinetochore signal, the signal is not completely ablated. Using immunofluorescence and co-staining for CENP-A and YFP (Venus-Mad2), we confirmed that knockdown of Trip13 reduced Mad2 kinetochore signal (Figure 5-3B). Finally, we co-stained for Mad1 and CENP-A and found that Mad1 kinetochore signal was not reduced in Trip13 siRNA treated cells (Figure 5-3C). Quantification of Mad1/CENP-A co-localization confirmed this (Figure 5-3D). Together, these data indicate that Trip13 likely regulates Mad2 kinetochore localization directly, as is the case with PCH-2 in *C. elegans*. Thus, Trip13 is required for a robust, nocodazole-induced, checkpoint response in RPE1 cells.

Next, we treated cells with another spindle poison, taxol, which produces a weaker spindle checkpoint response, as assayed by Mad2/kinetochore co-localization (COLLIN *et al.* 2013). Confirming this result, we found that control siRNA treated RPE1 cells showed that only a small fraction of kinetochores localized Venus-Mad2 (Figure 5-4A). Treatment with Trip13 siRNA did not alter Venus-Mad2 kinetochore localization, with still only a small fraction of cells localizing Venus-Mad2 (Figure 5-4A). Quantification revealed no statistically significant difference in Venus-Mad2/kinetochore co-localization between control and Trip13 siRNA treated cells. Therefore, when the spindle checkpoint response is weakly activated with taxol, the requirement for Trip13 in Mad2 kinetochore localization is lost.

Discussion

Unlike *C. elegans* PCH-2, it appears Trip13 is not required for the spindle checkpoint in human cells. Instead, knockdown of Trip13 appears to reduce kinetochore accumulation of Mad2, indicating a weaker checkpoint response. Furthermore, in RPE1 cells, TRIP13 is only necessary for full Mad2 kinetochore localization when a robust checkpoint response is induced with nocodazole, but not when the checkpoint is induced weakly with taxol. These results indicate that Trip13 may function as a checkpoint robustness factor in human cells. To confirm this hypothesis, more checkpoint robustness assays should be completed. Previously, it was shown that Cyclin A is rapidly depleted when the checkpoint is activated robustly (COLLIN *et al.* 2013). Therefore, Cyclin A (Venus-CyclinA) degradation should be monitored in Trip13 siRNA cells treated with nocodazole. Furthermore, partial knockdown of Mad2 reduces checkpoint robustness. To determine if Trip13 is unnecessary for this weakened checkpoint response, Trip13 should be double depleted in Mad2 heterozygotes. If Mad2 kinetochore recruitment remains unchanged, this is consistent with Trip13 function as a checkpoint robustness factor. Recently, it was shown that during *C. elegans* embryogenesis, cell size determines checkpoint strength—larger cells produce weaker checkpoint responses than smaller cells (GALLI AND MORGAN 2016). While the authors determined that the "kinetochore-to-cytoplasmic" ratio determines the checkpoint strength in these cells, the molecular requirements for the checkpoint robustness factor remain enigmatic. PCH-2^{TRIP13} is an excellent candidate for this cell size robustness factor. Larger cells, early in embryogenesis, may require PCH-2^{TRIP13} to recruit Mad2 to kinetochores, as we have shown previously (NELSON *et al.* 2015). However, as cells progress through embryogenesis, cells become smaller, and the kinetochore-to-cytoplasm ratio increases. These later born cells may no longer require PCH-2^{TRIP13} to recruit Mad2 to kinetochores for checkpoint activation. This hypothesis is easily testable, utilizing drug sensitive genetic backgrounds (CARVALHO *et al.* 2011), and treating late-stage *pch-2* mutant embryos with nocodazole, assaying for

checkpoint function. It may turn out that PCH-2 is merely a robustness factor in *C. elegans* as well, indicating that its checkpoint function is fully conserved.

In *C. elegans*, PCH-2 utilizes the adaptor protein, CMT-1, to recruit MAD-2 to kinetochores. The human ortholog of CMT-1, called p31(comet), has also been shown to interact with Mad2 (YANG *et al.* 2007). In *C. elegans*, *pch-2;cmt-1* double mutants are checkpoint functional and localize significant MAD-2 to kinetochores, indicating the PCH-2/CMT-1 module is not absolutely required for checkpoint function in *C. elegans*. Future experiments should determine whether p31(comet) functions analogously during spindle checkpoint activation in human cells. For example, does double depletion of Trip13 and p31(comet) rescue the Mad2 localization defect compared to Trip13 single knockdown?

Human Trip13 was originally identified as a kinetochore component required for the disassembly of the MCC during mitotic exit (WANG *et al.* 2014b) (EYTAN *et al.* 2014a). However, more recent data, where TRIP13 was knocked out using CRISPR, argued that TRIP13 is not required for mitotic exit (MA AND POON 2016). Given that TRIP13 is overexpressed in HeLa cells, these malignant cells may have co-opted TRIP13 to help promote mitotic exit, perhaps through its binding to Mad2. Mad2 is a member of the mitotic checkpoint complex (MCC), which sequesters the anaphase promoting complex (APC) co-activator Cdc20 in order to block anaphase onset. Trip13 overexpression may titrate away Mad2 from the MCC, which would help to promote APC activation and mitotic exit. Thus, cancer cell lines may overexpress TRIP13 to drive cells through mitosis. Indeed, several reports have shown TRIP13 to be oncogenic and TRIP113 is frequently overexpressed in cancers (RHODES *et al.* 2004; BANERJEE *et al.* 2014). Thus, further analysis of TRIP13 checkpoint function should be carried out in non-transformed cell lines, like RPE1.

Materials & Methods

Cell Culture & RNA interference

HeLa cells were cultured in Dulbecco's Modified Eagle Medium (DMEM; Thermo Fisher) supplemented with 10% fetal bovine serum (FBS), 100U/mL penicillin, and 100ug/mL

of streptomycin. RPE1 cells were cultured F12/DMEM (Thermo Fisher) supplemented with Glutamax (Invitrogen), 10% FBS, 100U/mL penicillin, 100ug/mL of streptomycin, and 0.5ug/mL fungizone. Both cell lines were cultured n a 37°C incubator with 5% CO_2. For spindle checkpoint analysis, cells were treated with either 0.5uM nocodazole or 0.2uM taxol for 4 hours prior to analysis.

For lentiviral shRNA treatment of HeLa cells, a third generation lentiviral vector system was used to infect 293T cells. The vector was then harvested and titrated for robust infection of Hela cells, as verified by >90% expression of the co-GFP reporter. For the shRNA sequences utilized, see the Results section. After lentivirus infection, HeLa cells were sorted via FACS (UCSC Flow Cytometry Facility) for maximum GFP fluorescence. For siRNA treatment of RPE1 cells, transfection was performed using Lipofectamine RNAiMAX reagent (Invitrogen) of the following siRNAs: Trip13 (CAUUAUACCAACUGAGAAAUU), Mad2 (GAAGAGUCGGGACCACAGUU), and control (GAAACACUACCUAUAGAAUUU). siRNAs were transfected at 50nM for 48 hours prior to analysis.

Lysate Preparation & Immunoblot Analysis

For immunoblot analysis of siRNA knockdown efficiency, a 50mM plate of cells was cultured until cells were >90% confluent. To prepare lysates, plates were put on ice, and then washed 5X with PBS to remove all FBS. 250uL of RIPA buffer (20mM sodium phosphate pH7.5, 0.15M NaCl, 1% TritonX-100, 0.5% sodium deoxycholate, 0.1% SDS) supplemented with 1mM PMSF and Roche Protease Inhibitor Tablets was added to the cells and they were left on ice for 20 minutes. The cells were scraped from the plate using a rubber-policeman and then spun for 15 minutes at 40k. The supernatant was removed, an equal volume of 2X SB was added, and the sample was boiled for 5 minutes prior to loading on an SDS-PAGE gel.

For immunoblotting, samples were run on 12% SDS-PAGE gels, transferred to nitrocellulose using a Trans-Blot SD Semi-Dry system (Bio-Rad), blocked in a PBST + 5%

(w/v) non-fat milk solution, and then probed with either rabbit anti-TRIP13 (1:1000; gift from Liu lab), mouse anti-GAPDH (1:2500; Sigma), or rabbit anti-MAD-2 (1:1000, Bethyl) overnight at 4°C. Blots were washed 3x for 10 minutes in PBST, probed for 1 hour using an HRP-conjugated secondary antibody (rabbit or mouse; GE Healthcare), washed 3x for 10 minutes in PBST, and then analyzed using a chemiluminescent substrate (Thermo Scientific).

Immunofluorescence & Microscopy

All immunofluorescence and live microscopy was performed on a DeltaVision Personal DV deconvolution microscope (Applied Precision) equipped with a 100X N.A. 1.40 oil-immersion objective (Olympus) coupled with a CoolSNAP charge-coupled camera (Roper Scientific). Three-dimensional image stacks were collected at 0.2-μm Z-spacing and processed by constrained, iterative deconvolution. Image scaling and analysis were performed using functions in the softWoRx software package. Projections were calculated by a maximum intensity algorithm. Composite images were assembled and some false coloring was performed with Adobe Photoshop. For live microscopy analysis of Venus-Mad2, a YFP filter was utilized for image acquisition.

For immunofluorescence, media was removed, cells were incubated for 1 minute in pre-extraction buffer ((0.2% Triton X-100, 100mM Pipes pH 6.8, 1mM MgCl2, 5mM EGTA), fixed for 10 minutes (3.2% Paraformaldehyde in PBS), washed in 1X PBS, and then blocked for 1 hour (3% BSA in 1X PBS). After blocking, cells were incubated with primary antibody (in 1X PBS, .08mg/mL RNase A) overnight at 4C. Cells were washed 3X in PBS+0.01% TX-100, secondary antibodies were applied for 1 hour in the dark, cells were washed 3 more times in PBS+0.01% TX-100 and then mounted in 1X PBS, 70% glycerol). in PBS The following primary antibodies were used (dilutions in parentheses): rabbit anti-Mad2 (1:1000, Bethyl), mouse anti-CENPA (1:500, Abcam), rabbit anti-Mad1 (Rabbit, Abcam), and mouse anti-Histone H3 phospho-serine 10 (1:500) [Sigma]. Secondary antibodies were Cy3 anti-mouse (Jackson Immunochemicals) and Alexa-Fluor 488 anti-rabbit (Invitrogen).

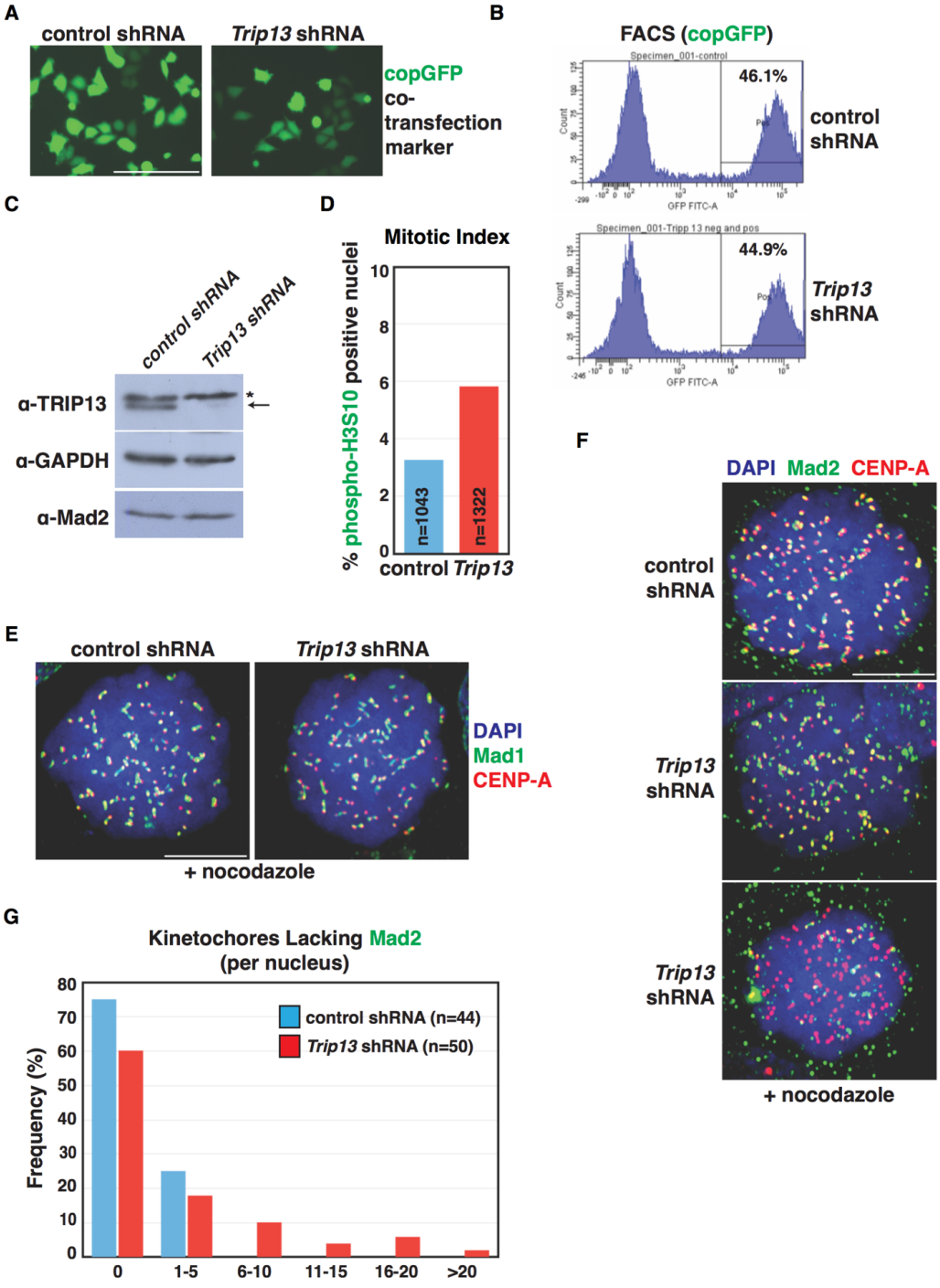

Figure 5- 1: Analysis of the role of TRIP13 in the HeLa cell spindle checkpoint.

(A) Expression of co-transfection copGFP marker indicates lentiviral delivery of *Trip13* and a scrambled control shRNAs into HeLa cells was successful. Scale bar represents 200 μm. (B) FACS using copGFP marker was used to enrich for shRNA knockdown. (C) Immunoblot of sorted cells indicates TRIP13 protein level is reduced with *Trip13* shRNA, but not the

scrambled control. GAPDH is used as a loading control. Mad2 levels are not reduced in *Trip13* shRNA strain. (D) Knockdown of *Trip13* via shRNA increases mitotic index, consistent with previous reports that TRIP13 is important for mitotic exit. (E) Control and *Trip13* shRNA cells properly localize Mad1 to kinetochores after nocodazole treatment. Scale bar represents 5 μm. (F) A subset of Trip13 shRNA cells fail to properly localize Mad2 (bottom panel) to all kinetochores (CENP-A). Scale bar represents 5 μm. (G) Trip13 shRNA increases the frequency of nuclei with kinetochores (CENP-A) lacking Mad2 localization. Quantification of nuclei from (F).

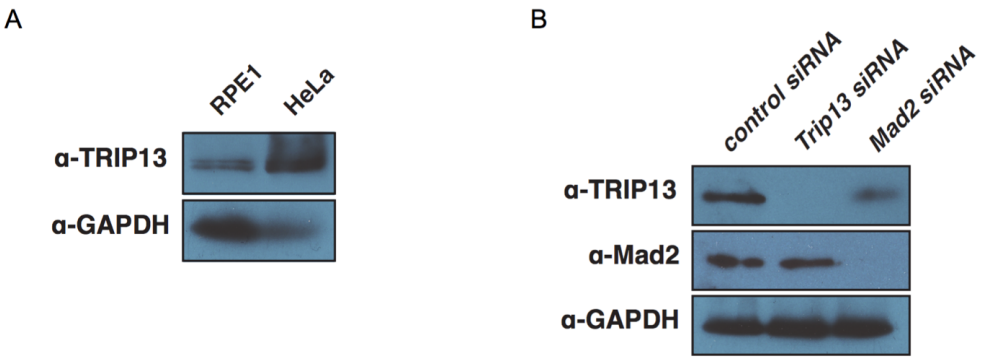

Figure 5- 2: TRIP13 is overexpressed in HeLa cells.

(A) TRIP13 is dramatically overexpressed in human cancer cells (HeLa) compared to non-cancerous human epithelial cells (RPE1). (B) Trip13 and Mad2 are successfully knocked down via direct siRNA of RPE1 cells.

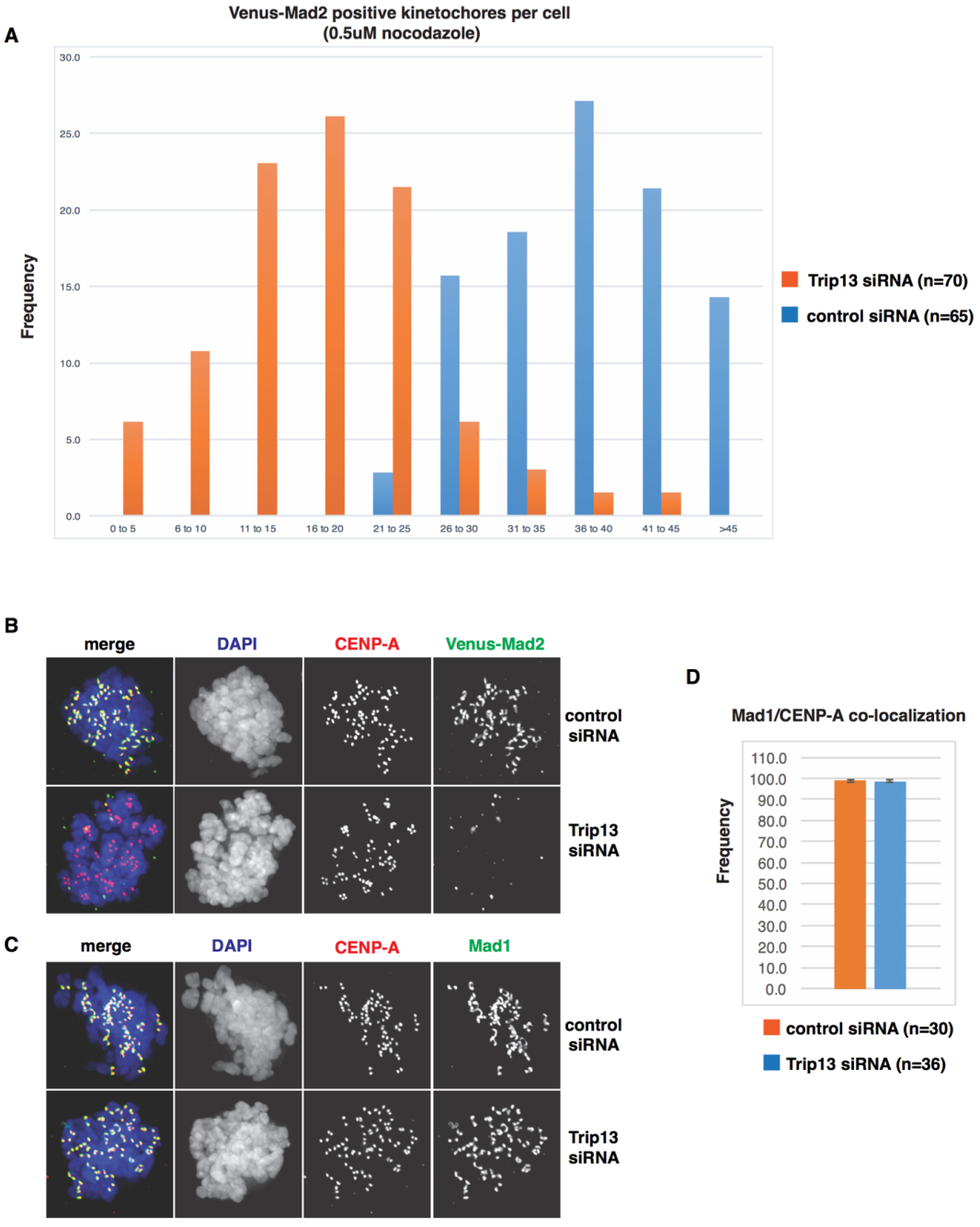

Figure 5- 3: TRIP13 is required for robust MAD-2 localization to kinetochores during spindle checkpoint activation in RPE1 cells.

(A) Quantification of Venus-Mad-2 positive kinetochores via live microscopy after nocodazole treatment of control or Trip13 siRNA RPE1 cells. (B) Immunofluorescence of nocodazole treated RPE1 cells with CENP-A and Mad2 antibodies shows that Trip13 is required for complete Mad2 kinetochore recruitment (C) Immunofluorescence of nocodazole treated RPE1 cells with CENP-A and Mad1 antibodies shows that Trip13 is NOT required for Mad1 kinetochore recruitment (D) Quantification of Mad1/CENP-A co-localization in C.

A

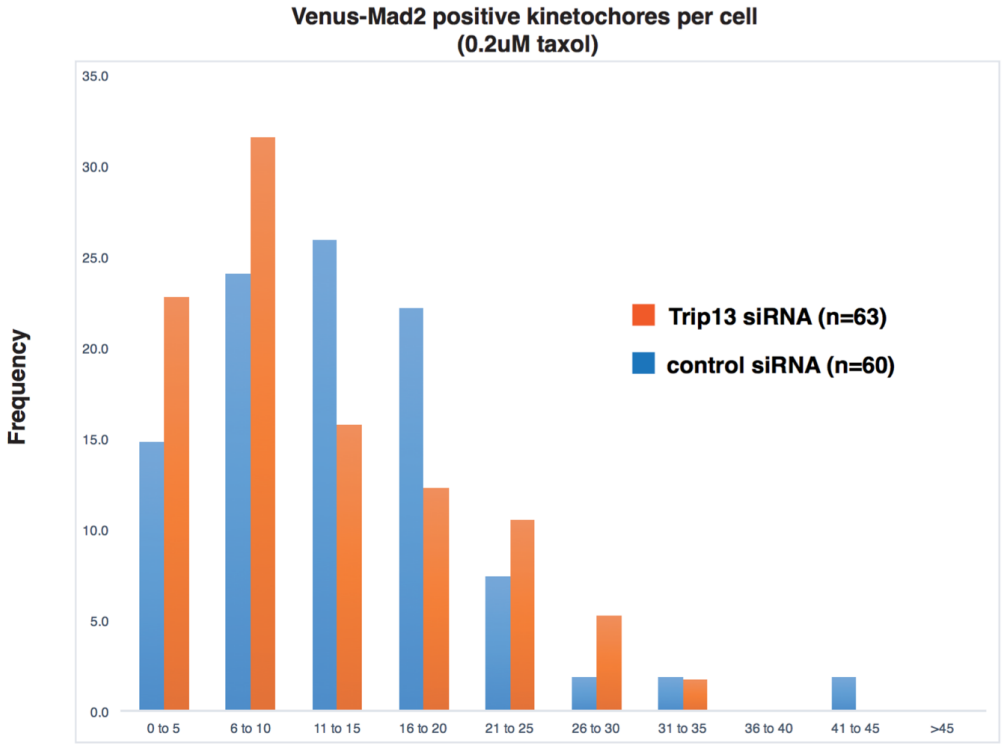

Figure 5- 4: TRIP13 is not required for a weak taxol induced checkpoint response in RPE1 cells.

(A) Quantification of Venus-Mad-2 positive kinetochores after taxol treatment of control or Trip13 siRNA RPE1 cells.

References

Agarwal, S., and G. S. Roeder, 2000 Zip3 provides a link between recombination enzymes and synaptonemal complex proteins. Cell 102**:** 245-255.

Akiyoshi, B., C. R. Nelson, J. A. Ranish and S. Biggins, 2009a Quantitative proteomic analysis of purified yeast kinetochores identifies a PP1 regulatory subunit. Genes & development 23**:** 2887-2899.

Akiyoshi, B., C. R. Nelson, J. A. Ranish and S. Biggins, 2009b Quantitative proteomic analysis of purified yeast kinetochores identifies a PP1 regulatory subunit. Genes Dev 23**:** 2887-2899.

Aravind, L., and E. V. Koonin, 1998 The HORMA domain: a common structural denominator in mitotic checkpoints, chromosome synapsis and DNA repair. Trends in biochemical sciences 23**:** 284-286.

Arur, S., M. Ohmachi, S. Nayak, M. Hayes, A. Miranda *et al.*, 2009 Multiple ERK substrates execute single biological processes in Caenorhabditis elegans germ-line development. Proc Natl Acad Sci U S A 106**:** 4776-4781.

Ballister, E. R., M. Riegman and M. A. Lampson, 2014 Recruitment of Mad1 to metaphase kinetochores is sufficient to reactivate the mitotic checkpoint. J Cell Biol 204**:** 901-908.

Banerjee, R., N. Russo, M. Liu, V. Basrur, E. Bellile *et al.*, 2014 TRIP13 promotes error-prone nonhomologous end joining and induces chemoresistance in head and neck cancer. Nat Commun 5**:** 4527.

Bao, Z., Z. Zhao, T. J. Boyle, J. I. Murray and R. H. Waterston, 2008 Control of cell cycle timing during C. elegans embryogenesis. Developmental biology 318**:** 65-72.

Bhalla, N., and A. F. Dernburg, 2005 A conserved checkpoint monitors meiotic chromosome synapsis in Caenorhabditis elegans. Science 310**:** 1683-1686.

Bhalla, N., and A. F. Dernburg, 2008 Prelude to a division. Annu Rev Cell Dev Biol 24: 397-424.

Bhalla, N., D. J. Wynne, V. Jantsch and A. F. Dernburg, 2008 ZHP-3 acts at crossovers to couple meiotic recombination with synaptonemal complex disassembly and bivalent formation in C. elegans. PLoS Genet 4: e1000235.

Borner, G. V., A. Barot and N. Kleckner, 2008 Yeast Pch2 promotes domainal axis organization, timely recombination progression, and arrest of defective recombinosomes during meiosis. Proc Natl Acad Sci U S A 105: 3327-3332.

Brenner, S., 1974 The genetics of Caenorhabditis elegans. Genetics 77: 71-94.

Burger, J., J. Merlet, N. Tavernier, B. Richaudeau, A. Arnold *et al.*, 2013 CRL(2LRR-1) E3-ligase regulates proliferation and progression through meiosis in the *Caenorhabditis elegans* germline. PLoS genetics 9: e1003375.

Canman, J. C., D. B. Hoffman and E. D. Salmon, 2000 The role of pre- and post-anaphase microtubules in the cytokinesis phase of the cell cycle. Curr Biol 10: 611-614.

Carvalho, A., S. K. Olson, E. Gutierrez, K. Zhang, L. B. Noble *et al.*, 2011 Acute drug treatment in the early C. elegans embryo. PLoS One 6: e24656.

Cheeseman, I. M., J. S. Chappie, E. M. Wilson-Kubalek and A. Desai, 2006 The conserved KMN network constitutes the core microtubule-binding site of the kinetochore. Cell 127: 983-997.

Cheeseman, I. M., and A. Desai, 2008a Molecular architecture of the kinetochore-microtubule interface. Nat Rev Mol Cell Biol 9: 33-46.

Cheeseman, I. M., and A. Desai, 2008b Molecular architecture of the kinetochore-microtubule interface. Nature reviews. Molecular cell biology 9: 33-46.

Chelysheva, L., D. Vezon, A. Chambon, G. Gendrot, L. Pereira *et al.*, 2012 The Arabidopsis HEI10 is a new ZMM protein related to Zip3. PLoS Genet 8: e1002799.

Chen, B., J. Mariano, Y. C. Tsai, A. H. Chan, M. Cohen *et al.*, 2006 The activity of a human endoplasmic reticulum-associated degradation E3, gp78, requires its Cue domain, RING finger, and an E2-binding site. Proc Natl Acad Sci U S A 103**:** 341-346.

Chen, C., A. Jomaa, J. Ortega and E. E. Alani, 2014 Pch2 is a hexameric ring ATPase that remodels the chromosome axis protein Hop1. Proceedings of the National Academy of Sciences of the United States of America 111**:** E44-53.

Chen, R. H., A. Shevchenko, M. Mann and A. W. Murray, 1998 Spindle checkpoint protein Xmad1 recruits Xmad2 to unattached kinetochores. J Cell Biol 143**:** 283-295.

Chen, R. H., J. C. Waters, E. D. Salmon and A. W. Murray, 1996 Association of spindle assembly checkpoint component XMAD2 with unattached kinetochores. Science 274**:** 242-246.

Chen, Z., T. B. Gibson, F. Robinson, L. Silvestro, G. Pearson *et al.*, 2001 MAP kinases. Chem Rev 101**:** 2449-2476.

Cheng, C. H., Y. H. Lo, S. S. Liang, S. C. Ti, F. M. Lin *et al.*, 2006 SUMO modifications control assembly of synaptonemal complex and polycomplex in meiosis of Saccharomyces cerevisiae. Genes Dev 20**:** 2067-2081.

Cleveland, D. W., Y. Mao and K. F. Sullivan, 2003 Centromeres and kinetochores: from epigenetics to mitotic checkpoint signaling. Cell 112**:** 407-421.

Collin, P., O. Nashchekina, R. Walker and J. Pines, 2013 The spindle assembly checkpoint works like a rheostat rather than a toggle switch. Nat Cell Biol 15**:** 1378-1385.

Couteau, F., K. Nabeshima, A. Villeneuve and M. Zetka, 2004 A component of C. elegans meiotic chromosome axes at the interface of homolog alignment, synapsis, nuclear reorganization, and recombination. Curr Biol 14**:** 585-592.

Couteau, F., and M. Zetka, 2005 HTP-1 coordinates synaptonemal complex assembly with homolog alignment during meiosis in C. elegans. Genes Dev 19**:** 2744-2756.

Couteau, F., and M. Zetka, 2011 DNA damage during meiosis induces chromatin remodeling and synaptonemal complex disassembly. Dev Cell 20**:** 353-363.

Date, D. A., A. C. Burrows and M. K. Summers, 2014 Phosphorylation regulates the p31Comet-mitotic arrest-deficient 2 (Mad2) interaction to promote spindle assembly checkpoint (SAC) activity. J Biol Chem 289**:** 11367-11373.

De Antoni, A., C. G. Pearson, D. Cimini, J. C. Canman, V. Sala *et al.*, 2005 The Mad1/Mad2 complex as a template for Mad2 activation in the spindle assembly checkpoint. Curr Biol 15**:** 214-225.

Dernburg, A. F., 2001 Here, there, and everywhere: kinetochore function on holocentric chromosomes. J Cell Biol 153**:** F33-38.

Desai, A., S. Rybina, T. Muller-Reichert, A. Shevchenko, A. Hyman *et al.*, 2003 KNL-1 directs assembly of the microtubule-binding interface of the kinetochore in C. elegans. Genes & development 17**:** 2421-2435.

Deshaies, R. J., and C. A. Joazeiro, 2009 RING domain E3 ubiquitin ligases. Annu Rev Biochem 78**:** 399-434.

Deshong, A. J., A. L. Ye, P. Lamelza and N. Bhalla, 2014 A quality control mechanism coordinates meiotic prophase events to promote crossover assurance. PLoS genetics 10**:** e1004291.

Dickinson, D. J., J. D. Ward, D. J. Reiner and B. Goldstein, 2013 Engineering the Caenorhabditis elegans genome using Cas9-triggered homologous recombination. Nat Methods 10**:** 1028-1034.

Dougan, D. A., A. Mogk, K. Zeth, K. Turgay and B. Bukau, 2002 AAA+ proteins and substrate recognition, it all depends on their partner in crime. FEBS Lett 529**:** 6-10.

Encalada, S. E., J. Willis, R. Lyczak and B. Bowerman, 2005 A spindle checkpoint functions during mitosis in the early Caenorhabditis elegans embryo. Mol Biol Cell 16**:** 1056-1070.

Essex, A., A. Dammermann, L. Lewellyn, K. Oegema and A. Desai, 2009 Systematic analysis in Caenorhabditis elegans reveals that the spindle checkpoint is composed of two largely independent branches. Molecular biology of the cell 20**:** 1252-1267.

Eytan, E., K. Wang, S. Miniowitz-Shemtov, D. Sitry-Shevah, S. Kaisari *et al.*, 2014a Disassembly of mitotic checkpoint complexes by the joint action of the AAA-ATPase TRIP13 and p31(comet). Proc Natl Acad Sci U S A 111**:** 12019-12024.

Eytan, E., K. Wang, S. Miniowitz-Shemtov, D. Sitry-Shevah, S. Kaisari *et al.*, 2014b Disassembly of mitotic checkpoint complexes by the joint action of the AAA-ATPase TRIP13 and p31(comet). Proceedings of the National Academy of Sciences of the United States of America 111**:** 12019-12024.

Flaggs, G., A. W. Plug, K. M. Dunks, K. E. Mundt, J. C. Ford *et al.*, 1997 Atm-dependent interactions of a mammalian chk1 homolog with meiotic chromosomes. Curr Biol 7**:** 977-986.

Foley, E. A., and T. M. Kapoor, 2013a Microtubule attachment and spindle assembly checkpoint signalling at the kinetochore. Nat Rev Mol Cell Biol 14**:** 25-37.

Foley, E. A., and T. M. Kapoor, 2013b Microtubule attachment and spindle assembly checkpoint signalling at the kinetochore. Nature reviews. Molecular cell biology 14**:** 25-37.

Fraser, A. G., R. S. Kamath, P. Zipperlen, M. Martinez-Campos, M. Sohrmann *et al.*, 2000 Functional genomic analysis of C. elegans chromosome I by systematic RNA interference. Nature 408**:** 325-330.

Frokjaer-Jensen, C., M. W. Davis, C. E. Hopkins, B. J. Newman, J. M. Thummel *et al.*, 2008 Single-copy insertion of transgenes in Caenorhabditis elegans. Nat Genet 40**:** 1375-1383.

Galli, M., and D. O. Morgan, 2016 Cell Size Determines the Strength of the Spindle Assembly Checkpoint during Embryonic Development. Dev Cell 36**:** 344-352.

Gibson, D. G., L. Young, R. Y. Chuang, J. C. Venter, C. A. Hutchison, 3rd *et al.*, 2009 Enzymatic assembly of DNA molecules up to several hundred kilobases. Nat Methods 6**:** 343-345.

Gill, G., 2004 SUMO and ubiquitin in the nucleus: different functions, similar mechanisms? Genes Dev 18**:** 2046-2059.

Goodyer, W., S. Kaitna, F. Couteau, J. D. Ward, S. J. Boulton *et al.*, 2008 HTP-3 links DSB formation with homolog pairing and crossing over during C. elegans meiosis. Dev Cell 14**:** 263-274.

Hagan, R. S., M. S. Manak, H. K. Buch, M. G. Meier, P. Meraldi *et al.*, 2011 p31(comet) acts to ensure timely spindle checkpoint silencing subsequent to kinetochore attachment. Molecular biology of the cell 22**:** 4236-4246.

Hassold, T., and P. Hunt, 2001 To err (meiotically) is human: the genesis of human aneuploidy. Nat Rev Genet 2**:** 280-291.

Heinrich, S., E. M. Geissen, J. Kamenz, S. Trautmann, C. Widmer *et al.*, 2013 Determinants of robustness in spindle assembly checkpoint signalling. Nature cell biology 15**:** 1328-1339.

Heinrich, S., K. Sewart, H. Windecker, M. Langegger, N. Schmidt *et al.*, 2014 Mad1 contribution to spindle assembly checkpoint signalling goes beyond presenting Mad2 at kinetochores. EMBO Rep 15**:** 291-298.

Holland, A. J., and D. W. Cleveland, 2009 Boveri revisited: chromosomal instability, aneuploidy and tumorigenesis. Nat Rev Mol Cell Biol 10**:** 478-487.

Holland, A. J., and D. W. Cleveland, 2012 Losing balance: the origin and impact of aneuploidy in cancer. EMBO Rep 13**:** 501-514.

Howell, B. J., B. Moree, E. M. Farrar, S. Stewart, G. Fang *et al.*, 2004 Spindle checkpoint protein dynamics at kinetochores in living cells. Curr Biol 14**:** 953-964.

Jantsch, V., P. Pasierbek, M. M. Mueller, D. Schweizer, M. Jantsch *et al.*, 2004 Targeted gene knockout reveals a role in meiotic recombination for ZHP-3, a Zip3-related protein in Caenorhabditis elegans. Mol Cell Biol 24**:** 7998-8006.

Joshi, N., A. Barot, C. Jamison and G. V. Borner, 2009 Pch2 links chromosome axis remodeling at future crossover sites and crossover distribution during yeast meiosis. PLoS Genet 5: e1000557.

Joshi, N., M. S. Brown, D. K. Bishop and G. V. Borner, 2015 Gradual implementation of the meiotic recombination program via checkpoint pathways controlled by global DSB levels. Mol Cell 57: 797-811.

Kalogeropoulos, N., C. Christoforou, A. J. Green, S. Gill and N. R. Ashcroft, 2004 chk-1 is an essential gene and is required for an S-M checkpoint during early embryogenesis. Cell Cycle 3: 1196-1200.

Kamath, R. S., and J. Ahringer, 2003 Genome-wide RNAi screening in Caenorhabditis elegans. Methods 30: 313-321.

Kim, Y., S. C. Rosenberg, C. L. Kugel, N. Kostow, O. Rog *et al.*, 2014 The chromosome axis controls meiotic events through a hierarchical assembly of HORMA domain proteins. Dev Cell 31: 487-502.

Kirschner, M. W., and T. Mitchison, 1986 Microtubule dynamics. Nature 324: 621.

Kleckner, N., 2006 Chiasma formation: chromatin/axis interplay and the role(s) of the synaptonemal complex. Chromosoma 115: 175-194.

Kong, A., G. Thorleifsson, H. Stefansson, G. Masson, A. Helgason *et al.*, 2008 Sequence variants in the RNF212 gene associate with genome-wide recombination rate. Science 319: 1398-1401.

Kruse, T., M. S. Larsen, G. G. Sedgwick, J. O. Sigurdsson, W. Streicher *et al.*, 2014 A direct role of Mad1 in the spindle assembly checkpoint beyond Mad2 kinetochore recruitment. EMBO Rep 15: 282-290.

Kuijt, T. E., M. Omerzu, A. T. Saurin and G. J. Kops, 2014 Conditional targeting of MAD1 to kinetochores is sufficient to reactivate the spindle assembly checkpoint in metaphase. Chromosoma 123: 471-480.

Lackner, M. R., and S. K. Kim, 1998 Genetic analysis of the Caenorhabditis elegans MAP kinase gene mpk-1. Genetics 150**:** 103-117.

Lamesch, P., S. Milstein, T. Hao, J. Rosenberg, N. Li *et al.*, 2004 C. elegans ORFeome version 3.1: increasing the coverage of ORFeome resources with improved gene predictions. Genome Res 14**:** 2064-2069.

Lara-Gonzalez, P., F. G. Westhorpe and S. S. Taylor, 2012 The spindle assembly checkpoint. Current biology : CB 22**:** R966-980.

London, N., and S. Biggins, 2014 Signalling dynamics in the spindle checkpoint response. Nat Rev Mol Cell Biol 15**:** 736-747.

London, N., S. Ceto, J. A. Ranish and S. Biggins, 2012 Phosphoregulation of Spc105 by Mps1 and PP1 regulates Bub1 localization to kinetochores. Curr Biol 22**:** 900-906.

Luo, X., Z. Tang, J. Rizo and H. Yu, 2002 The Mad2 spindle checkpoint protein undergoes similar major conformational changes upon binding to either Mad1 or Cdc20. Mol Cell 9**:** 59-71.

Luo, X., Z. Tang, G. Xia, K. Wassmann, T. Matsumoto *et al.*, 2004 The Mad2 spindle checkpoint protein has two distinct natively folded states. Nat Struct Mol Biol 11**:** 338-345.

Ma, H. T., and R. Y. Poon, 2016 TRIP13 Regulates Both the Activation and Inactivation of the Spindle-Assembly Checkpoint. Cell Rep 14**:** 1086-1099.

MacQueen, A. J., M. P. Colaiacovo, K. McDonald and A. M. Villeneuve, 2002 Synapsis-dependent and -independent mechanisms stabilize homolog pairing during meiotic prophase in C. elegans. Genes Dev 16**:** 2428-2442.

Maldonado, M., and T. M. Kapoor, 2011 Constitutive Mad1 targeting to kinetochores uncouples checkpoint signalling from chromosome biorientation. Nature cell biology 13**:** 475-482.

Martinez-Perez, E., M. Schvarzstein, C. Barroso, J. Lightfoot, A. F. Dernburg *et al.*, 2008 Crossovers trigger a remodeling of meiotic chromosome axis composition that is linked to two-step loss of sister chromatid cohesion. Genes Dev 22**:** 2886-2901.

Martinez-Perez, E., and A. M. Villeneuve, 2005 HTP-1-dependent constraints coordinate homolog pairing and synapsis and promote chiasma formation during C. elegans meiosis. Genes Dev 19**:** 2727-2743.

Minshull, J., H. Sun, N. K. Tonks and A. W. Murray, 1994 A MAP kinase-dependent spindle assembly checkpoint in Xenopus egg extracts. Cell 79**:** 475-486.

Moghal, N., and P. W. Sternberg, 2003 The epidermal growth factor system in Caenorhabditis elegans. Exp Cell Res 284**:** 150-159.

Moyle, M. W., T. Kim, N. Hattersley, J. Espeut, D. K. Cheerambathur *et al.*, 2014 A Bub1-Mad1 interaction targets the Mad1-Mad2 complex to unattached kinetochores to initiate the spindle checkpoint. The Journal of cell biology 204**:** 647-657.

Musacchio, A., and E. D. Salmon, 2007 The spindle-assembly checkpoint in space and time. Nat Rev Mol Cell Biol 8**:** 379-393.

Nabeshima, K., A. M. Villeneuve and M. P. Colaiacovo, 2005 Crossing over is coupled to late meiotic prophase bivalent differentiation through asymmetric disassembly of the SC. J Cell Biol 168**:** 683-689.

Nabeshima, K., A. M. Villeneuve and K. J. Hillers, 2004 Chromosome-wide regulation of meiotic crossover formation in Caenorhabditis elegans requires properly assembled chromosome axes. Genetics 168**:** 1275-1292.

Neale, M. J., and S. Keeney, 2006 Clarifying the mechanics of DNA strand exchange in meiotic recombination. Nature 442**:** 153-158.

Nelson, C. R., T. Hwang, P. H. Chen and N. Bhalla, 2015 TRIP13PCH-2 promotes Mad2 localization to unattached kinetochores in the spindle checkpoint response. J Cell Biol 211**:** 503-516.

Nezi, L., and A. Musacchio, 2009 Sister chromatid tension and the spindle assembly checkpoint. Current opinion in cell biology 21**:** 785-795.

O'Connell, K. F., C. Caron, K. R. Kopish, D. D. Hurd, K. J. Kemphues *et al.*, 2001 The C. elegans zyg-1 gene encodes a regulator of centrosome duplication with distinct maternal and paternal roles in the embryo. Cell 105**:** 547-558.

Oegema, K., A. Desai, S. Rybina, M. Kirkham and A. A. Hyman, 2001 Functional analysis of kinetochore assembly in Caenorhabditis elegans. The Journal of cell biology 153**:** 1209-1226.

Page, S. L., and R. S. Hawley, 2003 Chromosome choreography: the meiotic ballet. Science 301**:** 785-789.

Paix, A., Y. Wang, H. E. Smith, C. Y. Lee, D. Calidas *et al.*, 2014 Scalable and Versatile Genome Editing Using Linear DNAs with Micro-Homology to Cas9 Sites in Caenorhabditis elegans. Genetics.

Penkner, A., L. Tang, M. Novatchkova, M. Ladurner, A. Fridkin *et al.*, 2007 The nuclear envelope protein Matefin/SUN-1 is required for homologous pairing in C. elegans meiosis. Dev Cell 12**:** 873-885.

Penkner, A. M., A. Fridkin, J. Gloggnitzer, A. Baudrimont, T. Machacek *et al.*, 2009 Meiotic chromosome homology search involves modifications of the nuclear envelope protein Matefin/SUN-1. Cell 139**:** 920-933.

Perry, J., N. Kleckner and G. V. Borner, 2005 Bioinformatic analyses implicate the collaborating meiotic crossover/chiasma proteins Zip2, Zip3, and Spo22/Zip4 in ubiquitin labeling. Proc Natl Acad Sci U S A 102**:** 17594-17599.

Praitis, V., E. Casey, D. Collar and J. Austin, 2001 Creation of low-copy integrated transgenic lines in Caenorhabditis elegans. Genetics 157**:** 1217-1226.

Qiao, H., H. B. Prasada Rao, Y. Yang, J. H. Fong, J. M. Cloutier *et al.*, 2014 Antagonistic roles of ubiquitin ligase HEI10 and SUMO ligase RNF212 regulate meiotic recombination. Nat Genet 46**:** 194-199.

Ranjitkar, P., M. O. Press, X. Yi, R. Baker, M. J. MacCoss *et al.*, 2010 An E3 ubiquitin ligase prevents ectopic localization of the centromeric histone H3 variant via the centromere targeting domain. Mol Cell 40**:** 455-464.

Reynolds, A., H. Qiao, Y. Yang, J. K. Chen, N. Jackson *et al.*, 2013 RNF212 is a dosage-sensitive regulator of crossing-over during mammalian meiosis. Nat Genet 45**:** 269-278.

Rhodes, D. R., J. Yu, K. Shanker, N. Deshpande, R. Varambally *et al.*, 2004 Large-scale meta-analysis of cancer microarray data identifies common transcriptional profiles of neoplastic transformation and progression. Proc Natl Acad Sci U S A 101**:** 9309-9314.

Roig, I., J. A. Dowdle, A. Toth, D. G. de Rooij, M. Jasin *et al.*, 2010 Mouse TRIP13/PCH2 is required for recombination and normal higher-order chromosome structure during meiosis. PLoS Genet 6.

San-Segundo, P. A., and G. S. Roeder, 1999 Pch2 links chromatin silencing to meiotic checkpoint control. Cell 97**:** 313-324.

Sanchez, Y., C. Wong, R. S. Thoma, R. Richman, Z. Wu *et al.*, 1997 Conservation of the Chk1 checkpoint pathway in mammals: linkage of DNA damage to Cdk regulation through Cdc25. Science 277**:** 1497-1501.

Sato, A., B. Isaac, C. M. Phillips, R. Rillo, P. M. Carlton *et al.*, 2009 Cytoskeletal forces span the nuclear envelope to coordinate meiotic chromosome pairing and synapsis. Cell 139**:** 907-919.

Shah, J. V., E. Botvinick, Z. Bonday, F. Furnari, M. Berns *et al.*, 2004 Dynamics of centromere and kinetochore proteins; implications for checkpoint signaling and silencing. Curr Biol 14**:** 942-952.

Sharrocks, A. D., S. H. Yang and A. Galanis, 2000 Docking domains and substrate-specificity determination for MAP kinases. Trends Biochem Sci 25**:** 448-453.

Shepperd, L. A., J. C. Meadows, A. M. Sochaj, T. C. Lancaster, J. Zou *et al.*, 2012 Phosphodependent recruitment of Bub1 and Bub3 to Spc7/KNL1 by Mph1 kinase maintains the spindle checkpoint. Curr Biol 22**:** 891-899.

Sheridan, S. D., X. Yu, R. Roth, J. E. Heuser, M. G. Sehorn *et al.*, 2008 A comparative analysis of Dmc1 and Rad51 nucleoprotein filaments. Nucleic Acids Res 36**:** 4057-4066.

Silva, N., N. Ferrandiz, C. Barroso, S. Tognetti, J. Lightfoot *et al.*, 2014 The fidelity of synaptonemal complex assembly is regulated by a signaling mechanism that controls early meiotic progression. Dev Cell 31**:** 503-511.

Sironi, L., M. Mapelli, S. Knapp, A. De Antoni, K. T. Jeang *et al.*, 2002 Crystal structure of the tetrameric Mad1-Mad2 core complex: implications of a 'safety belt' binding mechanism for the spindle checkpoint. The EMBO journal 21**:** 2496-2506.

Stein, K. K., E. S. Davis, T. Hays and A. Golden, 2007 Components of the spindle assembly checkpoint regulate the anaphase-promoting complex during meiosis in Caenorhabditis elegans. Genetics 175**:** 107-123.

Stevens, D., K. Oegema and A. Desai, 2013 Meiotic double-strand breaks uncover and protect against mitotic errors in the C. elegans germline. Current biology : CB 23**:** 2400-2406.

Sudakin, V., G. K. Chan and T. J. Yen, 2001 Checkpoint inhibition of the APC/C in HeLa cells is mediated by a complex of BUBR1, BUB3, CDC20, and MAD2. J Cell Biol 154**:** 925-936.

Symington, L. S., and J. Gautier, 2011 Double-strand break end resection and repair pathway choice. Annu Rev Genet 45**:** 247-271.

Teichner, A., E. Eytan, D. Sitry-Shevah, S. Miniowitz-Shemtov, E. Dumin *et al.*, 2011 p31comet Promotes disassembly of the mitotic checkpoint complex in an ATP-dependent process. Proc Natl Acad Sci U S A 108**:** 3187-3192.

Tipton, A. R., K. Wang, P. Oladimeji, S. Sufi, Z. Gu *et al.*, 2012 Identification of novel mitosis regulators through data mining with human centromere/kinetochore proteins as group queries. BMC cell biology 13**:** 15.

Vader, G., 2015 Pch2: controlling cell division through regulation of HORMA domains. Chromosoma.

Vink, M., M. Simonetta, P. Transidico, K. Ferrari, M. Mapelli *et al.*, 2006 In vitro FRAP identifies the minimal requirements for Mad2 kinetochore dynamics. Curr Biol 16**:** 755-766.

Vleugel, M., E. Hoogendoorn, B. Snel and G. J. Kops, 2012 Evolution and function of the mitotic checkpoint. Developmental cell 23**:** 239-250.

Voelkel-Meiman, K., L. F. Taylor, P. Mukherjee, N. Humphryes, H. Tsubouchi *et al.*, 2013 SUMO localizes to the central element of synaptonemal complex and is required for the full synapsis of meiotic chromosomes in budding yeast. PLoS Genet 9**:** e1003837.

Wang, F. Z., H. R. Fei, Y. J. Cui, Y. K. Sun, Z. M. Li *et al.*, 2014a The checkpoint 1 kinase inhibitor LY2603618 induces cell cycle arrest, DNA damage response and autophagy in cancer cells. Apoptosis 19**:** 1389-1398.

Wang, K., B. Sturt-Gillespie, J. C. Hittle, D. Macdonald, G. K. Chan *et al.*, 2014b Thyroid hormone receptor interacting protein 13 (TRIP13) AAA-ATPase is a novel mitotic checkpoint-silencing protein. J Biol Chem 289**:** 23928-23937.

Woglar, A., A. Daryabeigi, A. Adamo, C. Habacher, T. Machacek *et al.*, 2013a Matefin/SUN-1 phosphorylation is part of a surveillance mechanism to coordinate chromosome synapsis and recombination with meiotic progression and chromosome movement. PLoS genetics 9**:** e1003335.

Woglar, A., A. Daryabeigi, A. Adamo, C. Habacher, T. Machacek *et al.*, 2013b Matefin/SUN-1 phosphorylation is part of a surveillance mechanism to coordinate chromosome

synapsis and recombination with meiotic progression and chromosome movement. PLoS Genet 9: e1003335.

Wojtasz, L., K. Daniel, I. Roig, E. Bolcun-Filas, H. Xu *et al.*, 2009 Mouse HORMAD1 and HORMAD2, two conserved meiotic chromosomal proteins, are depleted from synapsed chromosome axes with the help of TRIP13 AAA-ATPase. PLoS Genet 5: e1000702.

Wu, H. Y., and S. M. Burgess, 2006 Two distinct surveillance mechanisms monitor meiotic chromosome metabolism in budding yeast. Curr Biol 16: 2473-2479.

Xia, G., X. Luo, T. Habu, J. Rizo, T. Matsumoto *et al.*, 2004 Conformation-specific binding of p31(comet) antagonizes the function of Mad2 in the spindle checkpoint. The EMBO journal 23: 3133-3143.

Xie, Y., and A. Varshavsky, 1999 The E2-E3 interaction in the N-end rule pathway: the RING-H2 finger of E3 is required for the synthesis of multiubiquitin chain. EMBO J 18: 6832-6844.

Yamagishi, Y., C. H. Yang, Y. Tanno and Y. Watanabe, 2012 MPS1/Mph1 phosphorylates the kinetochore protein KNL1/Spc7 to recruit SAC components. Nat Cell Biol 14: 746-752.

Yang, M., B. Li, D. R. Tomchick, M. Machius, J. Rizo *et al.*, 2007 p31comet blocks Mad2 activation through structural mimicry. Cell 131: 744-755.

Ye, Q., S. C. Rosenberg, A. Moeller, J. A. Speir, T. Y. Su *et al.*, 2015 TRIP13 is a protein-remodeling AAA+ ATPase that catalyzes MAD2 conformation switching. Elife 4.

Zanders, S., and E. Alani, 2009 The pch2Delta mutation in baker's yeast alters meiotic crossover levels and confers a defect in crossover interference. PLoS Genet 5: e1000571.

Zanders, S., M. Sonntag Brown, C. Chen and E. Alani, 2011 Pch2 modulates chromatid partner choice during meiotic double-strand break repair in Saccharomyces cerevisiae. Genetics 188: 511-521.

Zetka, M. C., I. Kawasaki, S. Strome and F. Muller, 1999 Synapsis and chiasma formation in Caenorhabditis elegans require HIM-3, a meiotic chromosome core component that functions in chromosome segregation. Genes Dev 13**:** 2258-2270.

Zhang, L., J. D. Ward, Z. Cheng and A. F. Dernburg, 2015 The auxin-inducible degradation (AID) system enables versatile conditional protein depletion in C. elegans. Development 142**:** 4374-4384.

Zickler, D., and N. Kleckner, 1999 Meiotic chromosomes: integrating structure and function. Annu Rev Genet 33**:** 603-754.